UNIVERSITY OF CALIFORNIA SAN DIEGO

Seismic Behavior of Deep, Slender Wide-flange Structural Steel Beam-columns

A Thesis submitted in partial satisfaction of the requirements
for the degree Master of Science

in

Structural Engineering

by

Piyachai Chansuk

Committee in charge:

Professor Chia-Ming Uang, Chair
Professor Joel P. Conte
Professor Benson Shing

2018

The Thesis of Piyachai Chansuk is approved, and it is acceptable in quality and form for publication on microfilm and electronically:

Chair

University of California San Diego

2018

TABLE OF CONTENTS

LIST OF FIGURES

LIST OF TABLES

ACKNOWLEDGEMENTS

Funding for this research was provided by the NEHRP Consultants Joint Venture Earthquake, Structural, and Engineering Research for the National Institute of Standards and Technology. Mr. J. O. Malley from Degenkolb Engineers chaired the Project Technical Committee, and Ms. A. Hortacsu from Applied Technology Council served as the project manager. Professor G. Mosqueda and Dr. A. Sarebanha assisted in developing a close-loop control algorithm for the SRMD test facility. Ms. V. Mazzotta assisted in nonlinear time-history analysis of a moment frame building. The author also would like to acknowledge the American Institute of Steel Construction for donating steel materials.

Chapter 2, 3, 4, and 5 in part are currently being prepared for submission for publication of the material. Chansuk, P., Ozkula, G., and Uang, C.-M. (2018). "ATC-106 Phase 2: Seismic behavior and design of deep, slender wide-flange structural steel beam-columns." *Report No. SSRP-18/02*, University of California, San Diego, La Jolla, CA. The thesis author was the primary investigator and author of this material.

ABSTRACT OF THE THESIS

Seismic Behavior of Deep, Slender Wide-Flange Structural Steel Beam-columns

by

Piyachai Chansuk

Master of Science in Structural Engineering

University of California San Diego, 2018

Professor Chia-Ming Uang, Chair

This thesis investigates nonlinear cyclic responses of deep wide-flange steel beam-columns, which are primarily used in Special Moment Frame (SMF) for their high in-plane, strong-axis moment of inertia to satisfy story drift limits specified in building codes. SMF design principles aim to achieve energy dissipation through plastic hinging of the beams, while flexural yielding of the columns at the base is also permitted. Although behavior of the beams has been extensively researched, that of the columns is lacking especially for deep columns (e.g., W18 to W36). Therefore, cyclic testing of deep columns was conducted to generate experimental database. Due to large width-to-thickness ratios of

these sections, test results showed significant web and flange local buckling; some specimens also exhibited lateral-torsional buckling. These local and global instabilities resulted in significant axial shortening and flexural strength degradation. These behaviors differ significantly from those observed in prior testing of shallow W14 columns, featuring excellent ductility capacity at high axial loads.

Additionally, the test matrix was designed to investigate the effects of section depths, varying axial loads, lateral-drift loading sequences, and boundary conditions on the column responses. Inevitably in this testing, the responses were also influenced by flexibility of column-end connections. To eliminate this undesired variable from the responses, a procedure was developed to correct the lateral drift response based on the second-order Timoshenko elastic theory. The effects of boundary conditions were further investigated using high-fidelity finite element software ABAQUS. Results show that fixed-fixed and fixed-rotating column responses can be converted to one another.

1. INTRODUCTION

1.1 General

Moment-resisting frames are one of the most common lateral force-resisting systems that are used in high seismic regions due to their high energy dissipation capacity and architectural versatility. Unexpected non-ductile failure of seismically designed steel moment connections that was observed after the Northridge, California Earthquake in 1994 had triggered extensive studies on the behavior of Special Moment Frames (SMF). Extensive studies, including those completed by the SAC Joint Venture (FEMA 2000), have been conducted to evaluate the cyclic behavior and design of beam-to-column connections. Since plastic hinging in the beams is expected in an SMF, cyclic behavior of beams, but not columns has also been researched.

Before the Northridge Earthquake, shallow wide-flange columns (e.g., W14 or W12 sections) were commonly used in moment-resisting frames because of their comparable strong- and weak-axis radii of gyration. However, it was challenging to continue using shallow sections in frame designs since they were required to have large lateral stiffness to satisfy the code-enforced story drift limit (ASCE 2016). To overcome this challenge, engineers turned to deeper steel columns, which were more economical in providing adequate lateral stiffness, i.e., the in-plane strong-axis moment of inertia. For instance, Table 1.1 compares the properties of shallow and deep sections with the same strong-axis moment of inertia (see Figure 1.1). The benefit of using the deep W30×148 section is obvious; the weight of the column is reduced from 426 to 148 lb/ft. However, the width-to-thickness ratios for flange local buckling (FLB) and, particularly, web local buckling (WLB) controls (i.e., $b_f/2t_f$ and h/t_w, respectively) are much larger for the deep

section, making it more susceptible to local instability. In addition, the deep column is also prone to out-of-plane, global-type member buckling like flexural buckling (FB) or lateral-torsional buckling (LTB) since its radius of gyration about the weak-axis (r_y) is much smaller than that (r_x) about the strong-axis.

Because columns in moment frames are subjected to both bending and axial loads during a seismic event, they are also referred to as beam-columns in design. Unfortunately, little experimental research on cyclic behavior of beam-columns is available to expansively support the seismic design or assessment provisions in AISC 341 (AISC 2016a) and ASCE 41 (ASCE 2013).

1.2 Literature Review

MacRae et al. (1990) tested 250UC73 (W10×49) columns under constant axial compression and cyclic lateral displacements with two cycles at each member displacement ductility of 2, 4, 6, 8, and 10, respectively. The constant axial force ratios, P/P_y, ranged from 0.0 to 0.8. Significant web and flange local buckling, axial shortening, and strength degradation were reported for beam-column specimens with high axial load.

Newell and Uang (2008) cyclically tested shallow W14 columns with varying axial load and reported high ductility capacities; web local buckling was limited or not observed in some specimens. In contrast, an analytical study by Newell and Uang (2006) demonstrated that cyclic hystereses of deeper columns (W27) subjected to high axial load were characterized by rapid strength degradation due to severe simultaneous web and flange local buckling.

To generate an experimental database as the basis for future analytical modeling of deep columns and evaluate the adequacy of design requirements for deep columns in AISC

341 and ASCE 41, NIST developed a comprehensive research plan to study the seismic behavior and design of deep, slender wide-flange structural steel beam-columns (NIST 2011). The plan included studies at the member, subassemblage, and system levels.

With the focus on the column behavior at the member level, Ozkula and Uang (2015) initiated the NIST study with full-scale testing of twenty-five wide-flange specimens, including five different W24 sections; each varied in section slenderness ratios ($b_f/2t_f$ and h/t_w) and member slenderness ratio (L/r_y). As shown in Table 1.2, the test matrix intended to investigate the effects of section slenderness parameters, constant axial load levels, lateral-drift sequences (including both cyclic and monotonic types), bending directions, and biaxial loading on the column responses. The test results confirmed the findings from the analytical study of deep-column cyclic responses conducted by Newell and Uang (2006). While in-plane plastic hinging in the form of simultaneous flange and web local buckling was observed at the member ends of W24×131 and W24×104 columns as expected, unexpected out-of-plane LTB was observed in W24×176 and W24×84 columns. This variation in instability behaviors of deep columns motivated additional testing in the NIST research program. Following this so-called Phase 1 study, Phase 2 study encompassed testing of additional twenty-three specimens with further diversified wide-flange sections ranging from W14 to W30 to further investigate Phase 1 objectives and examine the effects of section depths, varying axial loads, and boundary conditions on the column responses. A similar experimental investigation with fewer specimens that examined the beam-column cyclic behavior was conducted by Elkady and Lignos (2016), which investigated the same variables as the NIST studies.

Most of the specimens tested in the NIST studies sustained fixed-fixed boundary conditions; however, the top end of first-story columns in an SMF rotates during a seismic event due to flexibility of the connected beams, i.e., the columns experience fixed-rotating boundary conditions. To simulate and study this effect, four specimens in Phase 2 testing were subjected to cyclic rotation at the moving end with the magnitude proportional to the cyclic lateral drifts.

Testing of shallow, stocky W14 sections by Newell and Uang (2008) and deep, slender W24 sections by Ozkula and Uang (2015) has shown that beam-column *buckling mode* characterizes the column responses. Within a certain limit of L/r_y, a parameter based on section slenderness was proposed to predict the governing buckling mode (or failure mode), which are categorized into: (1) Symmetric Flange Local Buckling (SFB) mode, (2) Anti-symmetric Local Buckling (ALB) mode, and (3) Coupled Buckling (CB) mode (Ozkula et al. 2017). Buckled configurations and hysteretic features associated with each failure mode are briefly summarized in Section 2.8.

1.3 Scope of the Thesis

Phase 2 testing of the NIST research program is introduced in Chapter 2. Flexibility of column-end connections was observed in this testing, which affected the test responses. To allow a meaningful comparison between the test responses, the effect of connection flexibility needs to be removed from the global hystereses, i.e., the column shear and end moment versus lateral displacements. Chapter 3 presents the procedure developed to correct the lateral drift responses utilizing the second-order Timoshenko elastic theory.

This thesis presents the corrected test results in Chapter 4 and examines the effects of section depths, varying axial loads, lateral-drift sequences, and boundary conditions on the column responses.

Utilizing a high-fidelity finite element software ABAQUS, this thesis further investigates the boundary condition effect on the column responses in Chapter 5. Since most specimens in the NIST research program sustained fixed-fixed ends, developing a procedure that enable conversion of the fixed-fixed column responses to fixed-rotating column responses, which are more representative of the behavior of first-story columns in an SMF, becomes the objective of this study. Although some fixed-rotating column responses were obtained from Phase 2 testing (four boundary condition tests), calibrated finite element models were used to generate additional data to support and generalize the experimental findings.

Table 1.1 Section Property Comparison of Shallow and Deep Wide-flange Columns

Section	Weight (lb/ft)	r_x (in.)	r_y (in.)	I_x (in.^{4})	I_y (in.^{4})	$\frac{b_f}{2t_f}$	$\frac{h}{t_w}$
W14×426	426	7.26	4.34	6600	2360	2.75	6.08
W30×148	148	12.4	2.28	6680	227	4.44	41.6

Table 1.2 Test Matrix (Phase 1)

Group No.	Section	Specimen Designation	L (ft)	Slenderness			Column Axial Load		Bending Direction
				$\frac{b_f}{2t_f}$	$\frac{h}{t_w}$	$\frac{L}{r_y}$	C_a	P (kips)	
1	W24×176	1L 1M 1H	18	4.81	28.7	71.1	0.2 0.4 0.6	465 931 1396	Strong-axis
2	W24×131	2Z 2L 2L-P 2M 2M-NF 2H	18	6.70	35.6	72..7	0.0 0.2 0.2 0.4 0.4 0.6	0 347 347 693 693 1040	
3	W24×104	3L 3M 3H	18	8.50	43.1	74.2	0.2 0.4 0.6	276 551 826	
4	W24×84	4L 4M	18	5.86	45.9	110.8	0.2 0.4	222 445	
5	W24×55	5L 5LM 5M	18	6.94	54.6	161.2	0.2 0.3 0.4	146 219 292	
6	W24×131	6L 6L-P 6H	18	6.70	35.6	72..7	0.2 0.2 0.6	347 1040 1040	Weak-axis
7	W24×131	7M	18	6.70	35.6	72..7	0.4	693	Biaxial

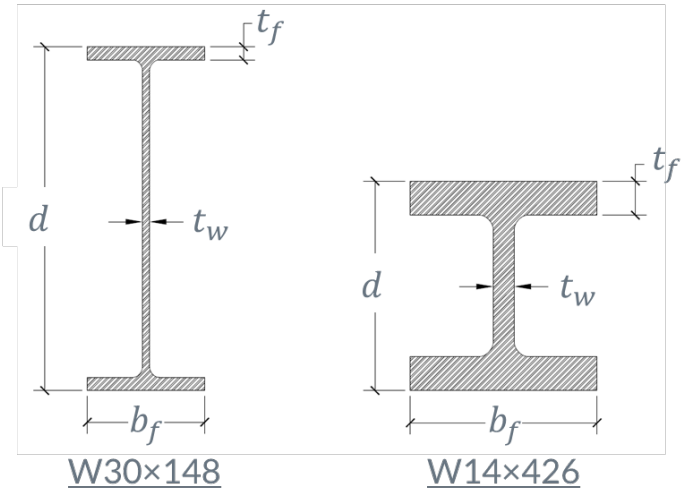

Figure 1.1 Comparison of Shallow and Deep Wide-flange Columns

2. TEST PROGRAM

2.1 Introduction

This chapter explains details of Phase 2 testing of the NIST research program that are relevant to the scope of this thesis; Chansuk et al. (2018) provide the complete information regarding the research. Although the original report divides Phase 2 testing into two sub-phases, i.e., Phase 2A and 2B, this thesis presents both testing details and results as one combined study but still keeps the same specimen-labeling scheme for consistency purpose.

2.2 Test Setup

Twenty-three wide-flange columns with sections ranging from W14 to W30 were subjected to inelastic strong-axis drifts utilizing various loading sequences and axial loads that could be constant or varying. The overall geometry of the test setup is shown in Figure 2.1. Testing was conducted in the Seismic Response Modification Device (SRMD) Test Facility at the University of California, San Diego. Specimens were tested in a horizontal position with one end (west end) connected to a reaction fixture fixed to a strong wall and the other end (east or moving end) connected to a reaction fixture tied down to the SRMD shake table platen. The platen had six degrees of freedom. Longitudinal movement of the platen imposed an axial force to the specimens. A force-control algorithm was employed to either maintain a constant axial load or apply varying axial load. Displacing the platen laterally in the horizontal plane imposed strong-axis bending to the specimens. To simulate fixed-rotating boundary conditions, the platen was prescribed a cyclic rotation in the

column strong-axis direction. The platen was in a displacement-control mode for lateral movements and strong-axis rotation.

2.3 Interior vs. Exterior Columns

During a seismic event, exterior first-story columns in an SMF sustain lateral drifts and significant fluctuation in axial load demands that could range from compressive to tensile forces due to dynamic overturning effects. On the contrary, interior columns experience limited axial load fluctuation and are assumed to sustain constant compressive axial loads in this research. A normalized parameter C_a is used to indicate the levels of axial load being applied to the specimens (AISC 2016a):

$$C_a = \frac{P_u}{\phi_c P_n} \tag{2.1}$$

where $P_u =$ applied axial load (positive for compression), $P_n = A_g F_{yn}$, $A_g =$ gross area, $F_{yn} =$ nominal yield stress, and $\phi_c =$ resistance factor (0.9). For most constant axial load tests simulating the interior-column condition, either of the three levels of axial compression, i.e., $C_a = 0.2$, 0.4, or 0.6, was applied to the specimens; letters "L", "M", and "H" represent these low, medium, and high levels, respectively, in the specimen designation. To accommodate the maximum capacity of the SRMD platen, some specimens were tested with C_a equal to 0.3 and named accordingly; "LM" indicates the average between the low- and medium-level axial compression. For varying axial load tests simulating the exterior-column condition, certain ranges of C_a were specified; specific details regarding varying axial load sequences are discussed in Section 2.6.2.

2.4 Design of Test Specimens

Figure 2.2 shows geometries and bolted end-connection details of typical specimens; additional information is documented by Chansuk et al. (2018). The weld access hole profile specified in AISC 360 (AISC 2016c) was used for welding detail. High-strength bolts with 1½-in. diameter were used to fasten the end plates to reaction fixtures.

Table 2.1 summarizes slenderness parameters of each specimen, including the member slenderness ratios, L/r_y, where L is the clear member length, and r_y is the radius of gyration about the weak axis. Wide-flange sections were selected such that the L/r_y ratios fall within a targeted and practical range.

Three "shallow" (W14) and ten "deep" (W18 to W30) wide-flange sections for a total of twenty-three specimens were included in Phase 2 testing. In Phase 1 testing, an "unusual" coupled buckling involving out-of-plane LTB was observed in Group 1 specimens (W24×176). Therefore, Group 11 was assigned with the same section as Group 1, and Specimen 11M was tested to confirm if the same failure mode could be reproduced. In addition, W14, W18, and W30 sections were included in Phase 2 test matrix to achieve two goals: (1) to investigate whether findings from Phase 1 (testing of W24 sections) can be applied to deeper (e.g., W30) and shallower (e.g., W14 and W18) columns, and (2) to expand the section slenderness database. Figure 2.3 illustrates distribution of the flange and web width-to-thickness ratios of test specimens with respect to the compactness limits specified in AISC 341 (AISC 2016a).

In Phase 1 testing, Group 5 specimens failed due to elastic LTB without plastic hinging at the member ends because their L/r_y ratio (= 161.2) was much larger than that of the other specimens. Consequently, inelastic cyclic responses associated with their

slenderness characteristics were not obtained. Group 14 specimen had a similar web slenderness to that of Group 5 specimens and a larger flange slenderness. But its L/r_y ratio (= 101.4) was much lower than that of Group 5 specimens, making it less prone to elastic LTB. Testing of Group 14 member was designed to fill this data gap.

All specimens were subjected to inelastic cyclic drifts except for Specimen 12LM-P ("P" for "Pushover"), which was tested monotonically to obtain a monotonic backbone curve for comparison with the cyclic backbone curve of its counterpart, Specimen 12LM. Furthermore, Specimen 21M-NF underwent the near-fault loading protocol (see Section 2.6.1); the results were used to study how different lateral-drift sequences affected column responses.

To study cyclic responses of exterior columns under different axial load variations caused by the overturning moment effect, Specimen 11H-VA, 21M-VAU, 21M-VAM, and 21M-VAU-BC were subjected to varying axial load sequences in conjunction with the AISC loading protocol ("VA" for "Varying Axial Load").

In Phase 1 testing, fixed-fixed boundary conditions were used. Therefore, they were mainly used in Phase 2 as well to allow a direct comparison between the test results from both phases. To evaluate the effects of rotation at the top end of first-story columns in an SMF caused by flexibility of the connected beams, four specimens with "BC" designation were tested with fixed-rotating boundary conditions.

2.5 Steel Material Properties

ASTM A992 was specified for all beam-column specimens, and A572 Gr. 50 steel was specified for the end plates. Table 2.2 summarizes mechanical properties of the specimens; coupons were taken from both webs and flanges. A sample of engineering

stress versus engineering strain relationships are shown in Figure 2.4 (refer to Chansuk et al. 2018 for more information).

2.6 Testing Procedure and Loading Protocols

Firstly, axial loads were applied to the specimens and either maintained at a constant level or varied with respect to a prescribed range as the specimens underwent inelastic lateral drifts imposed at the moving end of the columns (see Figure 2.1). For fixed-rotating boundary condition tests, cyclic rotation about the column strong axis was also prescribed to the platen. Several employed loading protocols are discussed below.

2.6.1 Lateral Drift Sequences

Since the objective of this research was to evaluate the cyclic responses of steel columns in moment frames, the standard loading protocol for qualifying cyclic tests of beam-to-column moment connections in Special and Intermediate Moment Frames specified in Section K2.4b of AISC 341-16 was utilized for most specimens. Figure 2.5(a) shows the typical story drift angle (*SDA*) history of the AISC loading protocol.

In addition to the AISC loading protocol, one specimen (Specimen 21M-NF) was tested with the near-fault loading protocol shown in Figure 2.5(d). This loading protocol was characterized by its large initial pulse that was followed by smaller-amplitude drift cycles oscillating about a level of residual drift. Beside these two cyclic loading protocols, the third lateral-drift sequence employed in this testing was a monotonic pushover, which was applied to Specimen 12LM-P.

Ultimately, the column responses corresponding to the AISC loading protocol, which resembled a far-field drift characteristic, the near-fault loading protocol, and the monotonic loading, were compared to study the effects of lateral-drift sequences.

2.6.2 Varying Axial Load Sequences

To examine exterior-column behavior, Specimen 11H-VA was tested with the AISC loading protocol in conjunction with the varying axial load sequence illustrated in Figure 2.5(b). The compressive axial load applied to this specimen fluctuated about a gravity load of $C_a = 0.45$. The cyclic axial load variation grew proportionally to lateral-drift amplitudes; this simulated the dynamic overturning-moment effect that amplified as a structure displaced to higher amplitudes. At a certain drift level, plastic hinging was expected at beam ends, and the overturning moment stabilized. Accordingly, the axial load range was capped between $C_a = 0.3$ and $C_a = 0.6$ at *SDA* of 0.01 rad and beyond.

The varying axial load sequences used with Specimens 21M-VAU, 21M-VAM, and 26LM-VAM are shown in Figure 2.6 with respect to the applied lateral drifts (i.e., the AISC loading protocol). The only differences between the sequences applied to Group 21 specimens and the ones used with Specimens 11H-VA and 26LM-VAM were the amplitude ranges and the time step at which the axial load reversed its direction. For Group 21 specimens, the axial load was set to reverse in direction at the same time step at which the lateral drift changed its direction (dash lines at some peak drifts were provided in Figure 2.6 to illustrate this behavior); this reflected a more accurate loading condition that exterior columns experienced in a seismic event. The axial load ranges were kept steady at *SDA* of 0.01 rad and beyond due to plastic hinging in beams.

In this testing, two types of axial load variation were considered with the following features: (1) the gravity load was set at a target C_a about which the axial load oscillated, and (2) the gravity load was set lower than a target C_a but the upper bound of the oscillating axial load was set at the target C_a. Specimens with the designation “VAM” were tested

with the first loading type, which had its "Mean" axial load (i.e., the gravity load) equal to a target C_a. On the contrary, specimens tested with the second loading type were labeled "VAU", indicating that the "Upper bound" of the axial load variation equaled to a target C_a. To investigate the varying axial load effect, column responses obtained from the "VAM" and/or "VAU" tests were compared with their counterpart specimen that was subjected to constant axial compression; the same target C_a were used in all comparable tests.

2.6.3 End Rotation Sequence

Due to flexibility of connected beams, first-story columns in an SMF sustain fixed-rotating boundary conditions during a seismic event. These boundary conditions were simulated in testing of four specimens (Specimens 11H-BC, 13M-BC, 16M-BC, and 21M-VAU-BC). Expressing top end rotation as a function of the story drift angle,

$$\theta = \xi \left(\frac{\Delta}{L}\right) \tag{2.2}$$

a three-bay, four-story SMF designed by Harris and Speicher (2015) was analyzed to determine an approximate ξ value for this test program. Based on a nonlinear, time-history analysis of this structure with 14 ground motions, scaled to match the Design Earthquake per ASCE 7, the top end rotation and the first-story drift angle were similar in magnitude, i.e., ξ = 1.0. Thus, for most boundary condition tests, strong-axis end rotation was prescribed at the platen end with the same magnitude as the applied story drift angle. Figure 2.5(c) shows the typical end rotation sequence that was applied in conjunction with the AISC loading protocol.

2.7 Instrumentation

Displacement transducers, inclinometers, strain gauge rosettes, and uniaxial strain gauges were used to measure global and local responses. Figure 2.7 shows displacement transducer and inclinometer layout. Figure 2.8 shows rosette and uniaxial strain gauge locations. Movements of the platen and their associated forces in six degrees of freedom were also recorded.

2.8 Characterization of Failure Modes

Testing of deep, slender columns in this study and shallow, stocky (W14) columns by Newell and Uang (2008) has shown that beam-column buckling mode characterizes the column hysteretic response. Within a certain limit of L/r_y, a parameter based on local slenderness properties was proposed to predict the governing buckling mode (or failure mode), which are categorized into: (1) Symmetric Flange Local Buckling (SFB) mode, (2) Anti-symmetric Local Buckling (ALB) mode, and (3) Coupled Buckling (CB) mode (Ozkula et al. 2017). The buckled configuration and hysteretic feature of each failure mode are briefly summarized herein. Failure mode classifications and certain phenomena discussed in this section are referenced in Chapter 4 to help explain the column behaviors observed during testing.

2.8.1 Symmetric Flange Local Buckling (SFB) Mode

For highly ductile sections with relatively low web and flange slenderness ratios (mostly shallow columns, e.g., W12 and W14 columns), SFB is the common governing failure mode. It involves in-plane plastic hinging at the column ends (or only at the bottom end of first-story columns in an SMF in real application) without out-of-plane, global-type member buckling. In the plastic hinge regions, at least a half-wave local buckle is observed

at each half-width flange in a *symmetric* (or 'mirrored') configuration with respect to the web plane as shown in Figure 2.9; for example, both top and bottom half-width flanges of the northeast flange in Figure 2.9(a) buckle outward locally, and their respective apexes are aligned. In addition, web local buckling, if occurs, is limited for this failure mode. Figure 2.10 illustrates the cross-sectional view of the SFB configuration. The corresponding column response exhibits large ductility capacity and limited axial shortening even under high axial compression (Newell and Uang, 2008). In fact, strength degradation is moderate and happens gradually for columns with SFB mode.

2.8.2 Anti-symmetric Local Buckling (ALB) Mode

As the section slenderness ratios increase, both flange and web local buckling modes occur simultaneously as the web cannot provide sufficient rotational restraint to maintain fix-ended boundary condition for the half-width, unstiffened flange elements. Figure 2.12 shows this combined local buckling mode, which features at least a half-wave local buckle at each half-width flange in an *anti-symmetric* (or 'opposite') configuration with respect to the web plane. Considering the northeast flange in Figure 2.12(a) for example, the top and bottom half-width flanges of the same flange buckle outward and inward, respectively, and their respective apexes are not aligned; the apex of the outward flange local buckle usually locates closer to the end plate compared to that of the inward one. In addition, as the web tries to remain perpendicular to the flanges at the web-flange junctions, it buckles locally in the direction that complies with the flange local buckling configuration; Figure 2.11 demonstrates the cross-sectional view of this phenomenon. Ultimately, ALB refers to the in-plane, plastic hinging failure mode with this combined local buckling configuration. Once ALB occurs, drastic strength degradation prevails, accompanied by significant column axial shortening. As a result, the column ductility

capacity is relatively limited compared to the SFB case. The ductility capacity associated with this failure mode is sensitive to the axial force level.

For specimens with ALB failure mode that sustain the AISC loading protocol in strong-axis bending, the ALB sequence initiates with one *half-wave buckle set* (i.e., one half-wave buckle at each unstiffen flange and stiffened web element) as shown in Figure 2.12(a). At higher drifts, some ALB specimens also develop an additional half-wave buckle set, making a full-wave buckle set, as shown in Figure 2.12(b). This full-wave ALB configuration usually results in severely deformed column ends, which initiates an out-of-plane, rigid-body translation of the column portion between the buckled regions; this movement should not be confused with lateral-torsional buckling or flexural buckling.

2.8.3 Coupled Buckling (CB) Mode

Coupled Buckling (CB) mode involves both local buckling and global-type, lateral-torsional buckling (LTB). The sequence of these local and global instabilities may not be obvious for all specimens since the two reciprocal phenomena are *coupled*. In obvious cases, two observations include: (1) local buckling at column proceeds LTB, and (2) LTB proceeds local buckling. Figure 2.13(a) shows the buckled configuration of the former sequence of which local buckling usually exhibits the ALB pattern as shown. The latter buckled configuration shown in Figure 2.13(b) is similar to the former one regarding the out-of-plane, LTB-type buckling behavior. However, local buckling pattern of the latter case as shown in Figure 2.14(a) only exhibits one half-wave local buckle in either the top or bottom half-width flange (of the same flange), not both like the SFB or ALB pattern; therefore, this type of flange local buckling should not be confused with the conventional local buckling as in SFB or ALB mode. Instead, it was triggered by LTB, which induces nonuniform stress distribution across the flange width because each flange bends about its

strong axis (explained in the following paragraph). In this report, LTB-induced flange local buckling refers to this phenomenon. Furthermore, LTB buckling configuration can be further subdivided into two cases: single and reverse curvatures; Figure 2.13(a) and Figure 2.13(b) refer to the former case, while Figure 2.13(c) refers to the latter case.

Twisting and out-of-plane bending associated with the LTB movements caused stress distribution to be nonuniform across the flange width. To demonstrate this phenomenon, strains at the upper and lower flange edges are plotted against each other in Figure 2.15 [see West End of Figure 2.13(b) for the strain gauge locations in the specimen under consideration]. Both strains are initially the same in magnitude (data points move along the 1:1 or 45° line), indicating a uniform bending stress distribution across the flange width due to in-plane bending of the specimen. Tendency of LTB then can be observed in the plot as the strains started to deviate from the 1:1 line, which initiates at $SDA = 0.015$ rad. Physically, flaking of the whitewash as shown in Figure 2.16(a) also illustrates this nonuniform stress distribution due to LTB; it exhibits a *sloped* flaking pattern as the upper flange portion experiences more compression and flakes off more mill scale compared to the lower portion. As twisting and out-of-plane movements become more visually observable at higher *SDA* levels, the out-of-plane, torsional, and warping stresses induced by LTB increase drastically. As a result, the strains become more nonuniform and the sloped flaking pattern grows drastically as shown in Figure 2.16(b) and Figure 2.16(c). In this case, the conventional way of defining the plastic hinge zone or length becomes difficult and may not be meaningful.

Chapter 2, 3, 4, and 5 in part are currently being prepared for submission for publication of the material. Chansuk, P., Ozkula, G., and Uang, C.-M. (2018). “ATC-106

Phase 2: Seismic behavior and design of deep, slender wide-flange structural steel beam-columns." *Report No. SSRP-18/02*, University of California, San Diego, La Jolla, CA. The thesis author was the primary investigator and author of this material.

Table 2.1 Test Matrix (Phase 2)

Group No.	Section	Specimen Designation	L (ft)	Slenderness			Column Axial Load		Parameter of Interest	Predicted Buckling Mode[a]
				$\frac{b_f}{2t_f}$	$\frac{h}{t_w}$	$\frac{L}{r_y}$	C_a	P (kips)		
11	W24×176	11M	17½	4.81	28.7	69.1	0.4	930	1M Repeat	Coupled Buckling
		11H-VA					0.3 to 0.6	698 to 1396	Varying Axial Load Effect	
		11H-BC					0.6	1396	Boundary Condition Effect	
12	W30×261	12LM	17½	4.59	28.7	59.5	0.3	1040	Section Depth Effect (Similar to Group 1)	Coupled Buckling
		12LM-P							Loading Sequence Effect	
13	W30×173	13M	17½	7.04	40.8	61.4	0.4	916	Section Depth Effect (Similar to Group 2)	In-plane Plastic Hinging
		13M-BC							Boundary Condition Effect	
14	W30×90	14L	17⅔	8.52	57.5	101.4	0.2	237	More Slender than Group 5	In-plane Plastic Hinging
15	W18×192	15L	17⅔	3.27	16.7	76.0	0.2	506	More Compact than Group 1	Coupled Buckling
16	W18×130	16M	17⅔	4.65	23.9	78.5	0.4	690	Section Depth Effect (Similar to Group 1)	
		16M-BC							Boundary Condition Effect	
17	W18×76	17L	17⅔	8.11	37.8	81.2	0.2	201	Section Depth Effect (Similar to Group 3)	In-plane Plastic Hinging

[a] Per the prediction of Ozkula et al. (2017).

Table 2.1 Test Matrix (Phase 2), Continued

Group No.	Section	Specimen Designation	L (ft)	Slenderness			Column Axial Load		Parameter of Interest	Predicted Buckling Mode[a]
				$\frac{b_f}{2t_f}$	$\frac{h}{t_w}$	L/r_y	C_a	P (kips)		
21	W18×130	21M-VAU	17⅔	4.65	23.9	78.5	-0.2 to 0.4	-345 to 690	Varying Axial (VA) Load	Coupled Buckling
		21M-VAU-BC					-0.2 to 0.4	-345 to 690	VA with Boundary Condition	
		21M-NF					0.4	690	Loading Sequence	
		21M-VAM					0.1 to 0.7	172 to 1206	Varying Axial Load	
22	W30×148	22L	18	4.44	41.6	94.7	0.2	392	New $b_f/2t_f - h/t_w$ domain	Coupled Buckling
23	W18×60	23L	14	5.44	38.7	100.0	0.2	158	New $b_f/2t_f - h/t_w$ domain	Coupled Buckling
24	W14×82	24L	14	5.92	22.4	67.7	0.2	216	Section Depth Effect	In-Plane Hinging with ALB
25	W14×53	25L	14	6.11	30.9	87.5	0.2	140	Section Depth Effect	Coupled Buckling
26	W14×132	26LM	14	7.15	17.7	44.7	0.3	524	Shallow Column	SFB
		26LM-VAM					0 to 0.6	0 to 1048	Varying Axial Load	
27	W24×84	27L	18	5.86	45.9	110.8	0.2	222	4L Repeat	Coupled Buckling

[a] Per the prediction of Ozkula et al. (2017).

Table 2.2 Steel Mechanical Properties

Group No.	Section	Comp.	F_y (ksi)	F_u (ksi)	Elong[e] (%)	Heat No.
11	W24×176	Flange	52.1	83.5	33.2	27469
		Web	51.4	82.7	36.1	
12	W30×261	Flange	54.6	75.6	38.3	451709
		Web	59.6	74.4	41.0	
13	W30×173	Flange	57.3	73.6	41.7	450564
		Web	67.2	79.7	37.0	
14	W30×90	Flange	58.3	73.7	37.1	417509
		Web	62.7	75.9	38.1	
15	W18×192	Flange	55.3	77.4	36.3	432017
		Web	60.8	77.1	39.6	
16[a]	W18×130	Flange	49.9	79.0	34.5	12986
		Web	53.3	78.8	34.8	
16[b]		Flange	52.1	71.2	40.9	354162
		Web	56.6	71.9	40.1	
17	W18×76	Flange	57.3	75.3	38.5	7505
		Web	54.8	66.1	32.3	
21	W18×130	Flange	54.8	70.9	39.1	471309
		Web	59.0	72.0	41.7	
22	W30×148	Flange	54.6	79.6	35.5	3G3357
		Web	66.2	83.3	34.5	
23	W18×60	Flange	49.4	68.1	37.3	59055727
		Web	55.4	69.0	35.6	
24	W14×82	Flange	51.6	68.4	38.7	59070575
		Web	54.4	69.5	36.9	
25	W14×53	Flange	54.8	70.4	35.9	438715
		Web	62.6	73.6	34.6	
26[c]	W14×132	Flange	51.5	70.8	38.4	456819
		Web	50.0	69.0	35.6	
26[d]		Flange	55.0	72.5	39.0	456821
		Web	55.7	71.6	39.0	
27	W24×84	Flange	54.1	80.8	35.2	36829
		Web	58.4	81.9	32.4	

[a] Group 16: Specimen 16M.

[b] Group 16: Specimen 16M-BC.

[c] Group 26: Specimen 26LM.

[d] Group 26: Specimen 26LM-VAM.

[e] Elongations are based on a 2-in. gauge length.

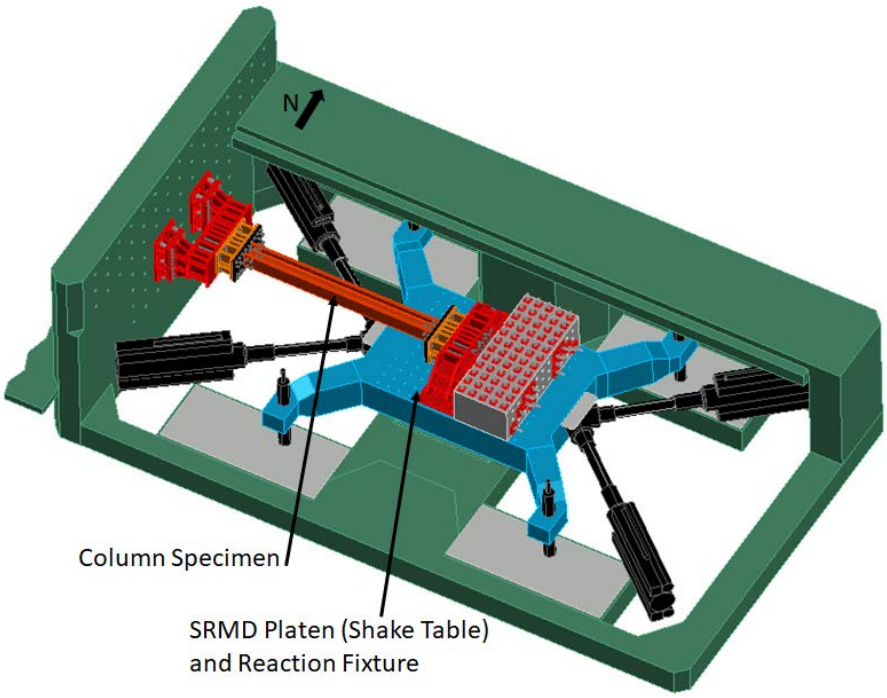

(a) Schematic View

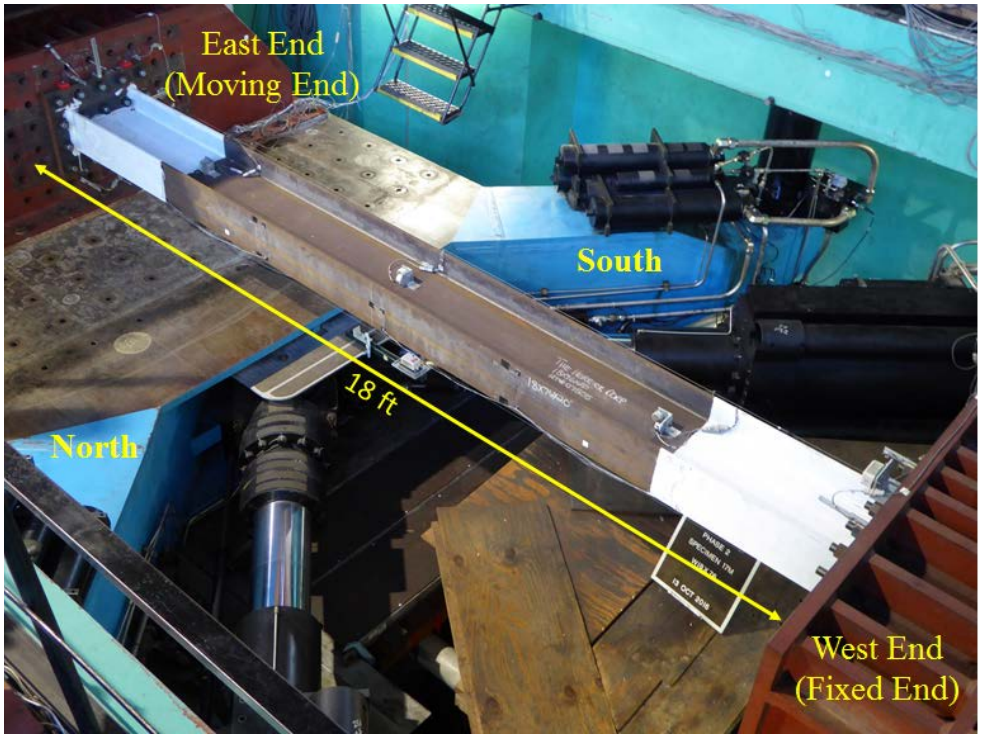

(b) Overview of Specimen

Figure 2.1 Test Setup

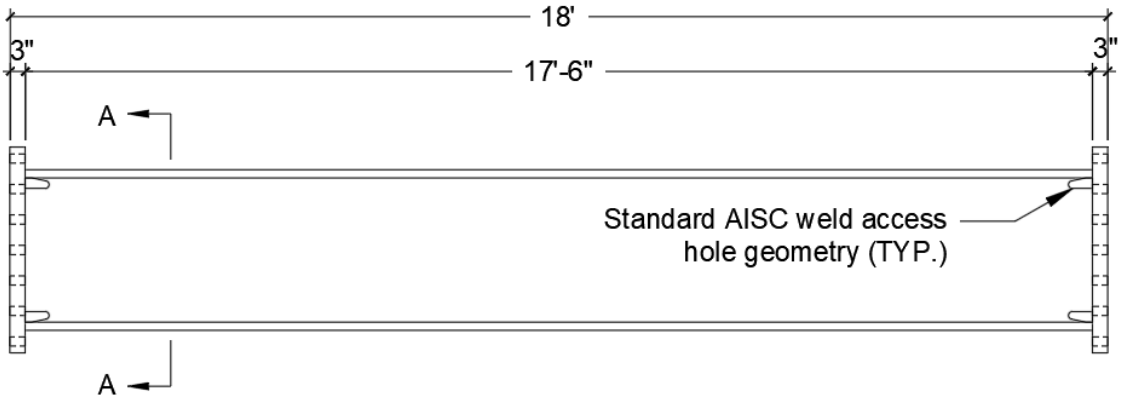

PLAN

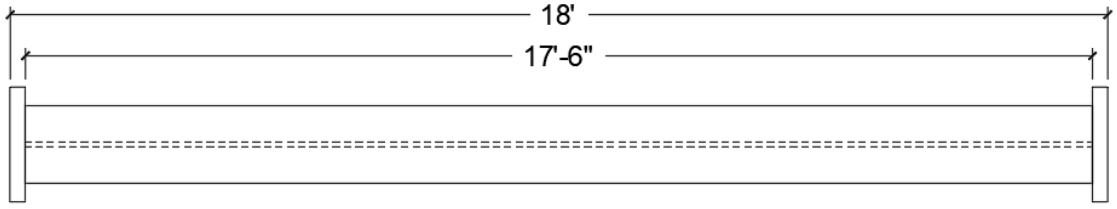

ELEVATION

(a) Overall Dimensions

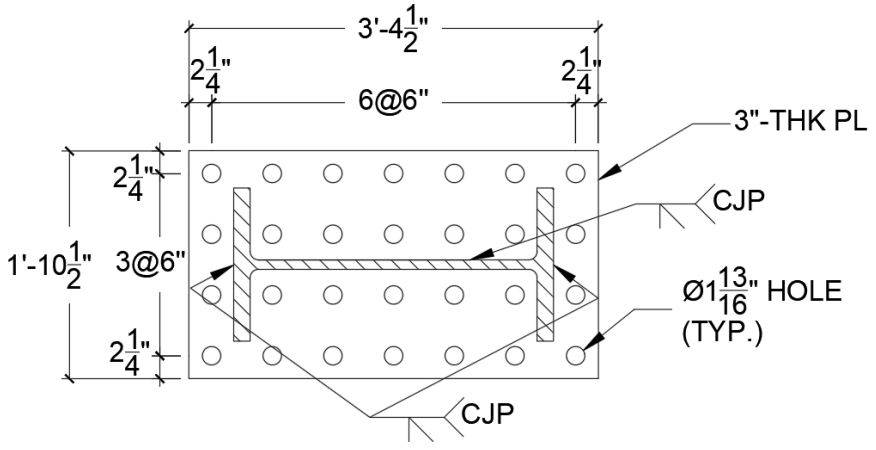

(b) Section A-A

Figure 2.2 Specimen Geometries and End Details (Groups 11 to 13)

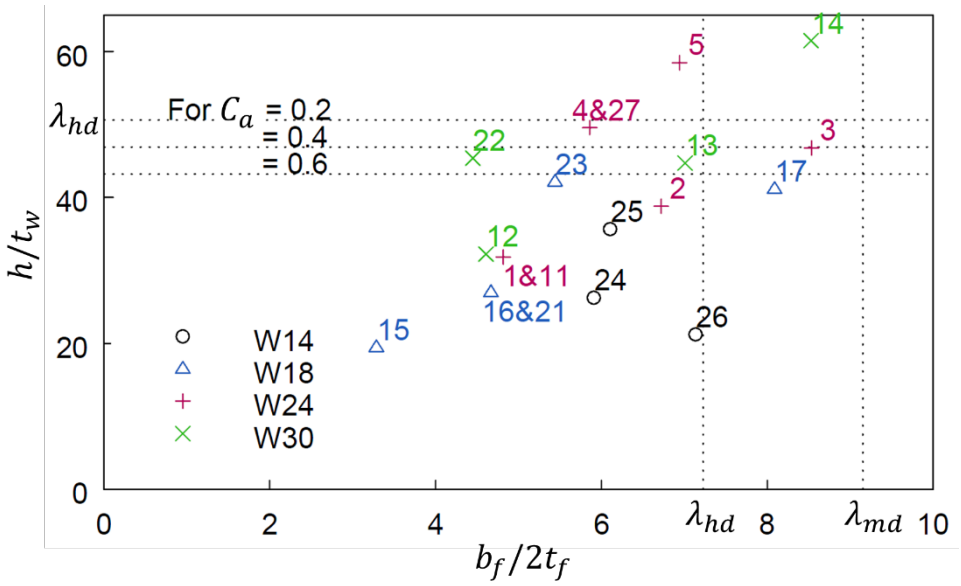

Figure 2.3 Distribution of Width-to-Thickness Ratios Annotated with Group Numbers

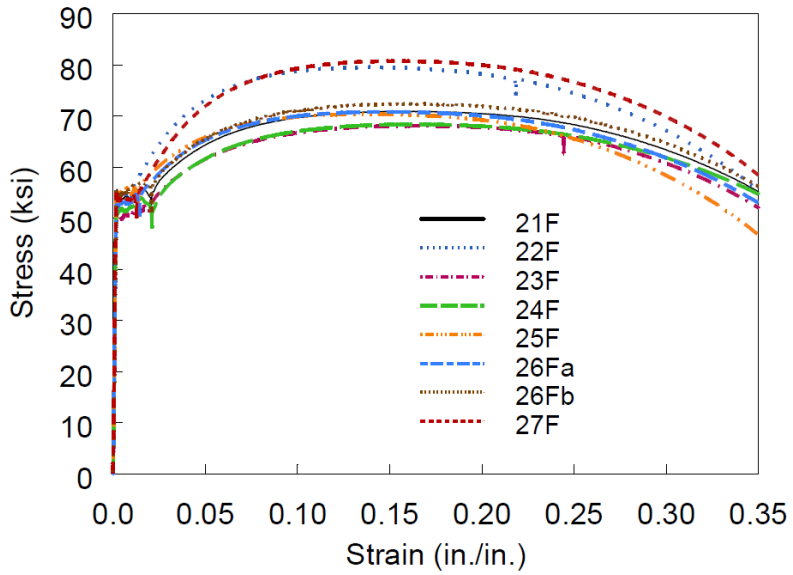

Figure 2.4 Samples of Engineering Strain versus Stress Curves

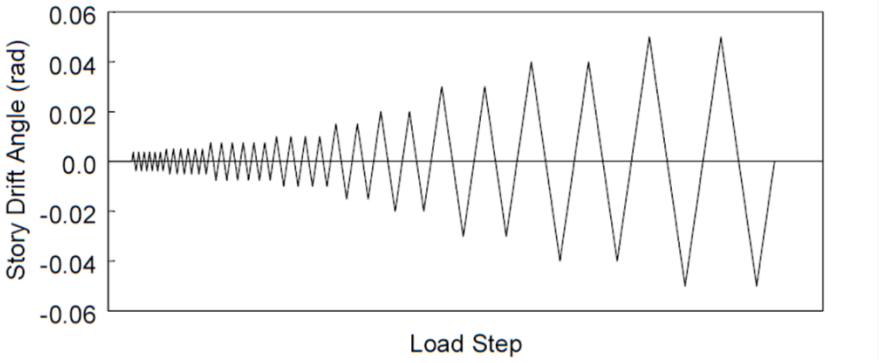

(a) AISC Story Drift Angle Loading Protocol

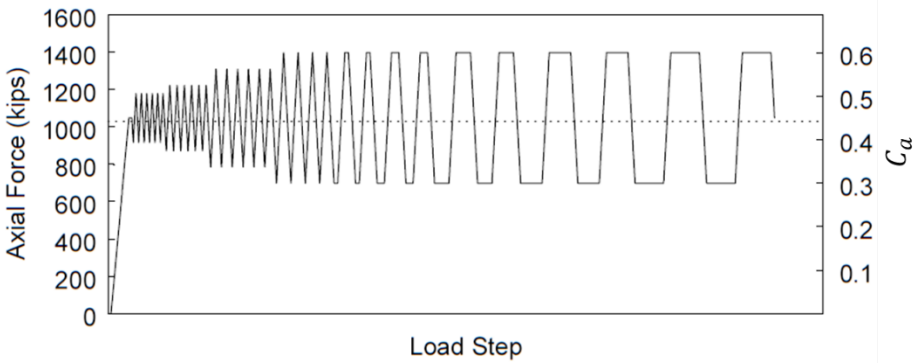

(b) Varying Axial Load Sequence (Specimen 11H-VA)

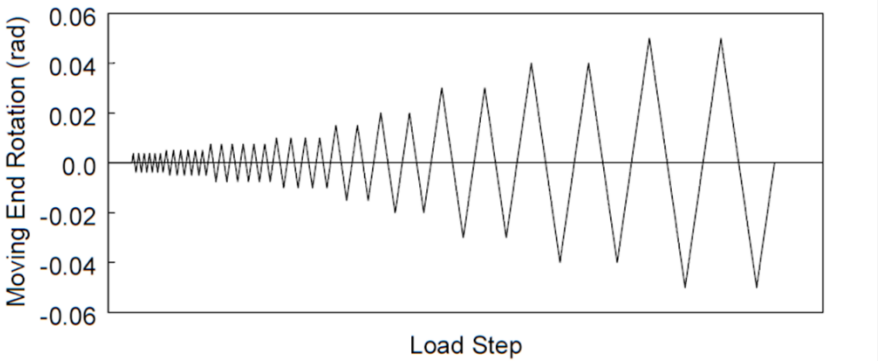

(c) Moving-end Rotation Sequence (ξ = 1.0)

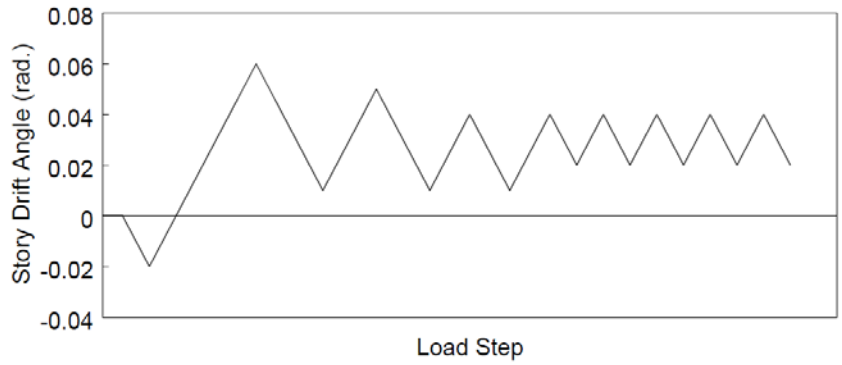

(d) Near-fault Loading Protocol

Figure 2.5 Cyclic Loading Schemes

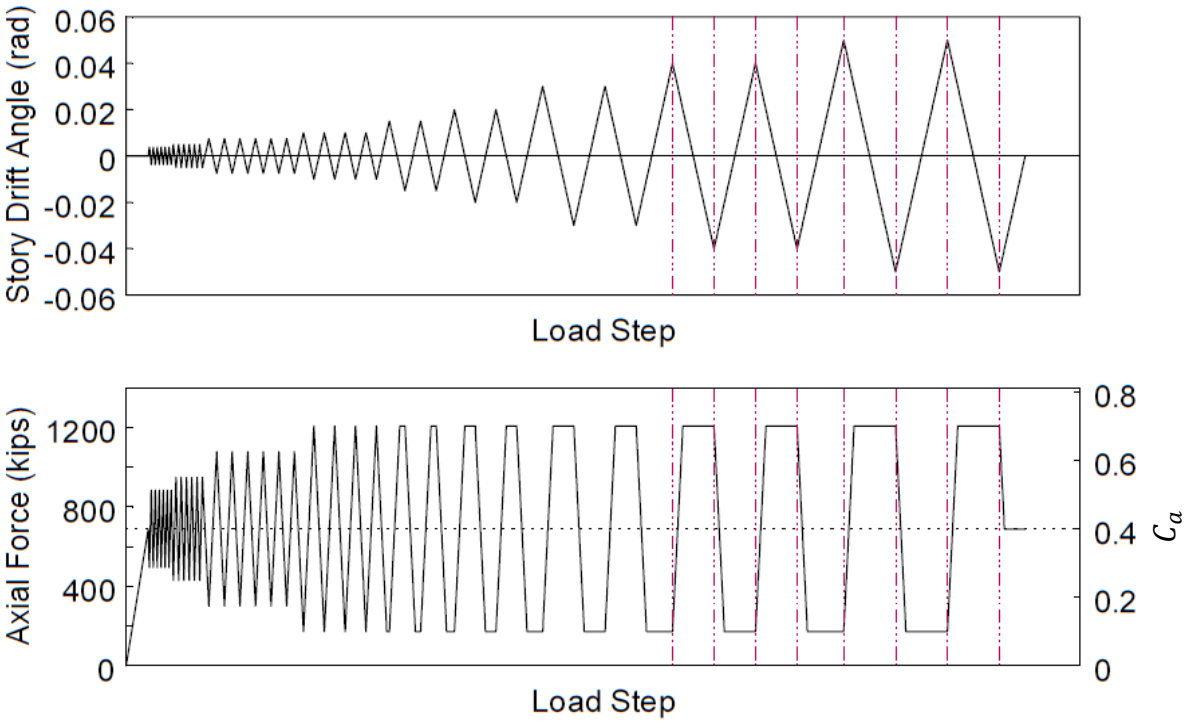

(a) Specimen 21M-VAM

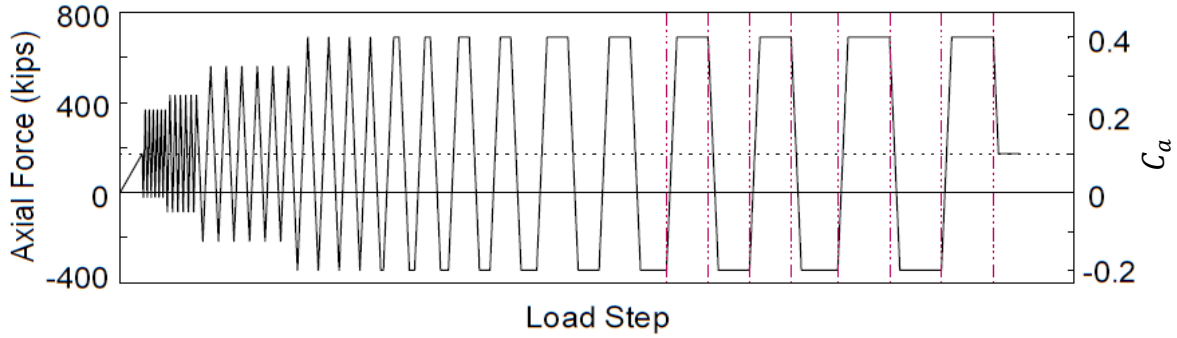

(b) Specimens 21M-VAU and 21M-VAU-BC

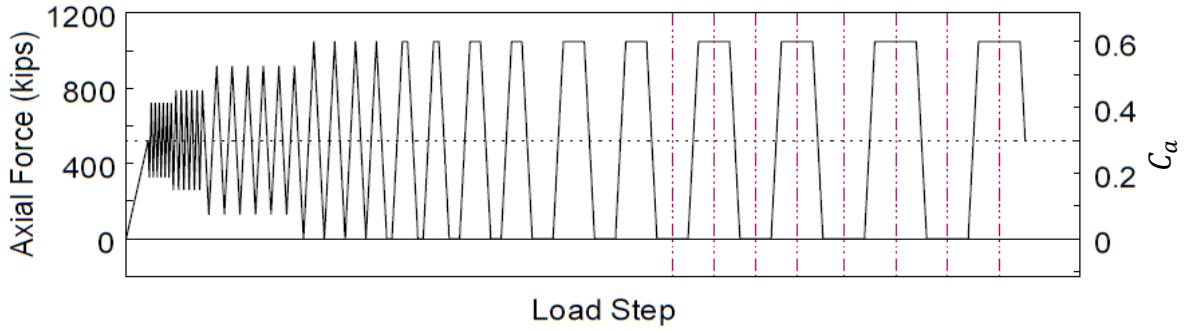

(c) Specimen 26LM-VAM

Figure 2.6 Varying Axial Load Sequences

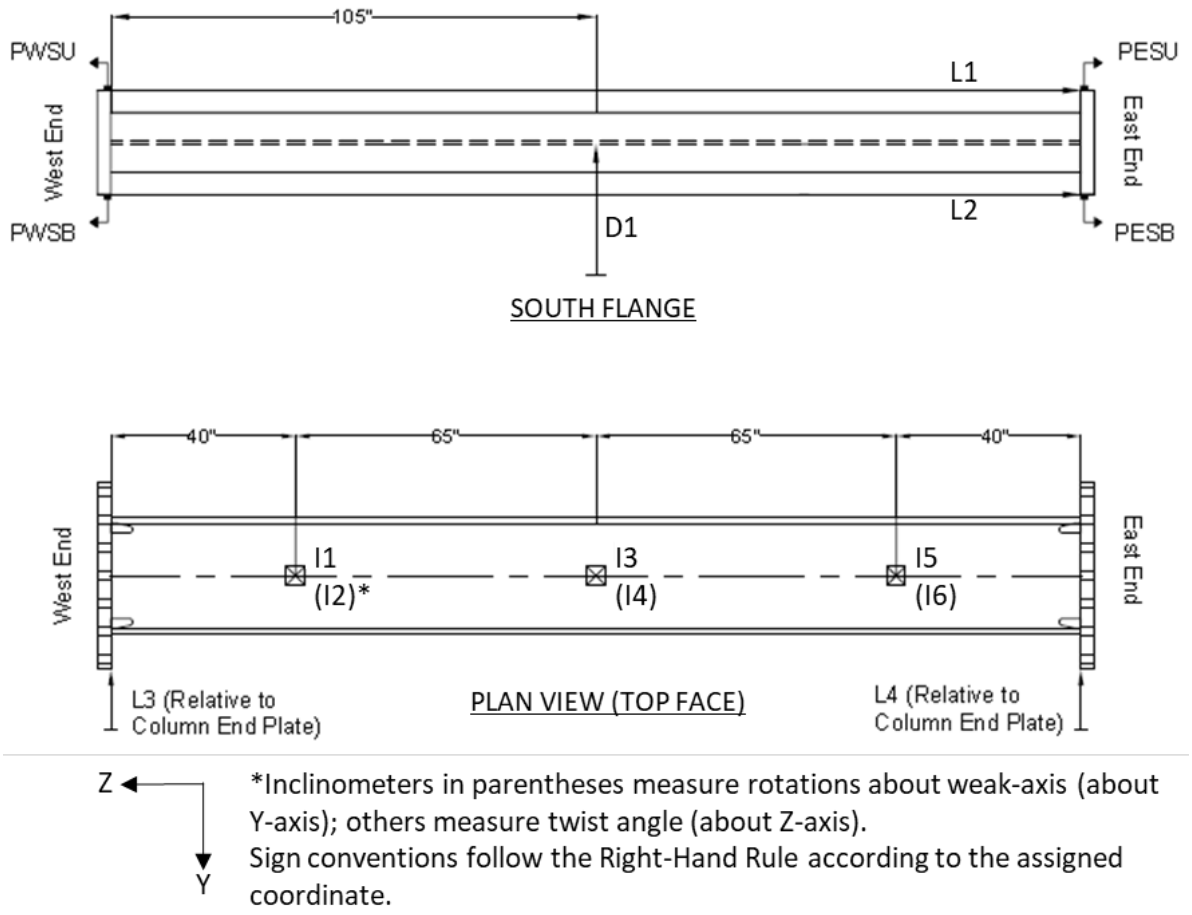

Figure 2.7 Typical Displacement Transducer and Inclinometer Layout

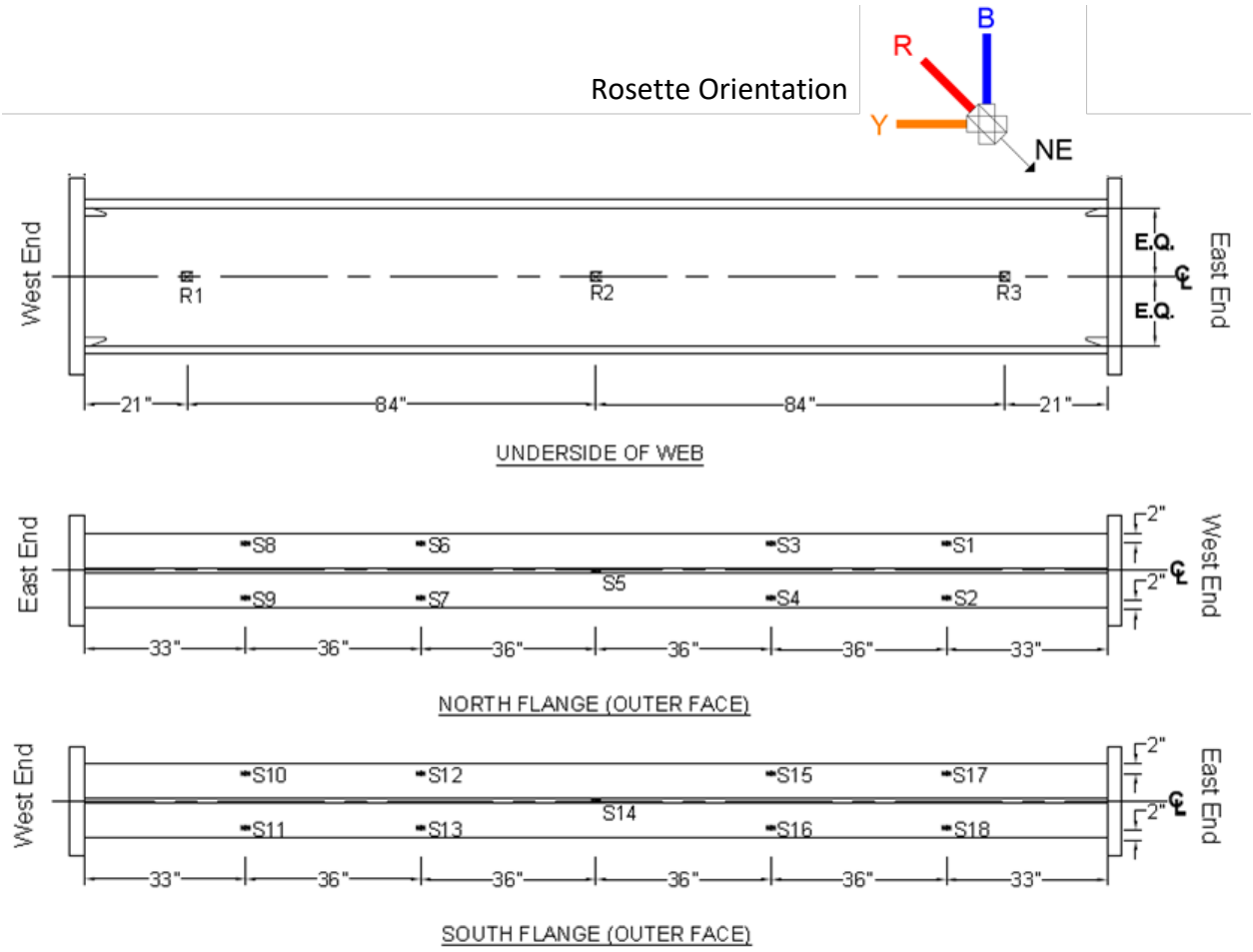

Figure 2.8 Typical Rosette and Uniaxial Strain Gauge Layout

(a) East End (b) Web at West End (c) West End

Figure 2.9 Symmetric Flange Local Buckling (SFB) Mode of W14×176 Section with $C_a = 0.61$ (Newell and Uang 2008)

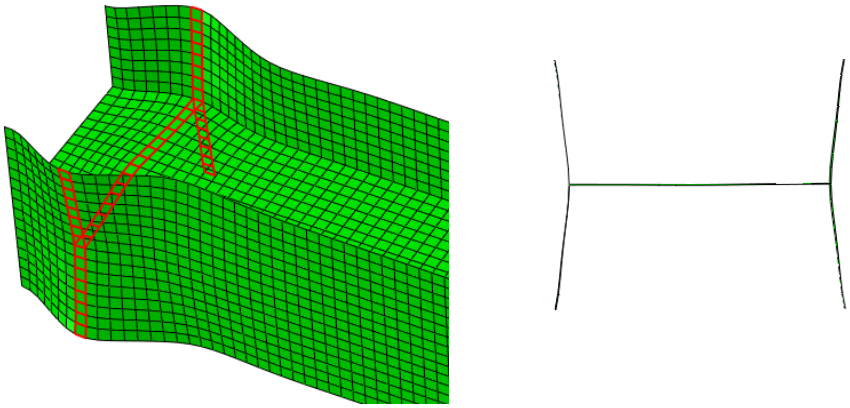

(a) Overall (b) Cross-sectional View

Figure 2.10 Flange Local Buckling Configuration in SFB

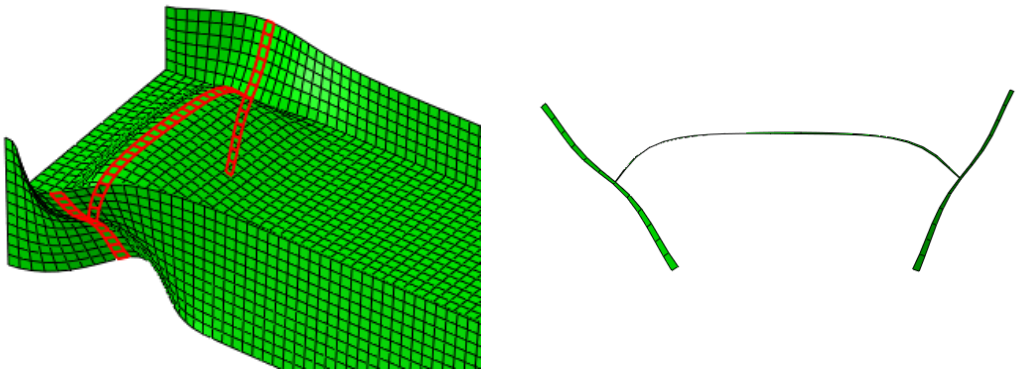

(a) Overall (b) Cross-sectional View

Figure 2.11 Flange and Web Local Buckling Configuration in ALB

East End Overall West End

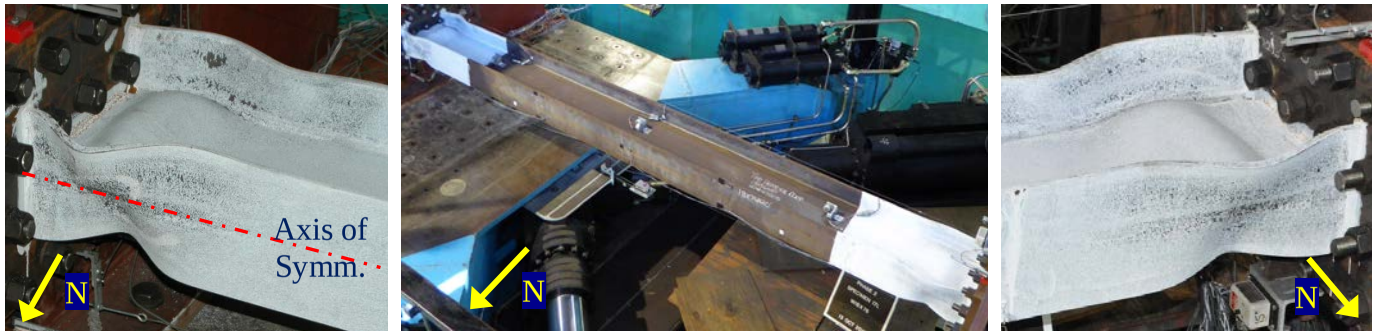

(a) *SDA* = 0.03 rad

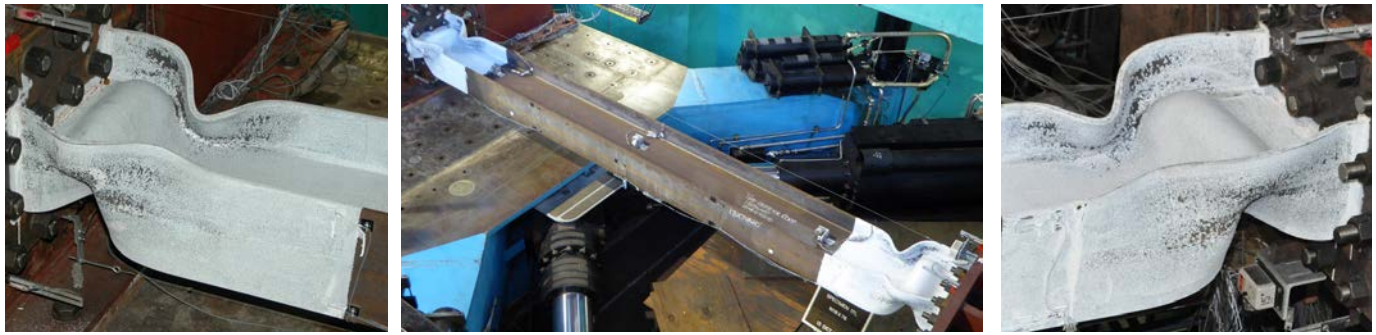

(b) *SDA* = 0.05 rad

Figure 2.12 Anti-symmetric Local Buckling (ALB) Mode of W18×76 Column with C_a = 0.2 (Specimen 17L)

East End Overall West End

(a) Single-Curvature Coupled Buckling Mode of W24×84 Column with C_a = 0.2 (Specimen 27L)

(b) Single-Curvature Coupled Buckling Mode of W18×130 Column with C_a = 0.4 (Specimen 16M)

(c) Reserve-Curvature Coupled Buckling Mode of W24×176 Column with C_a = 0.2 (Specimen 1L)

Figure 2.13 Coupled Buckling (CB) Mode

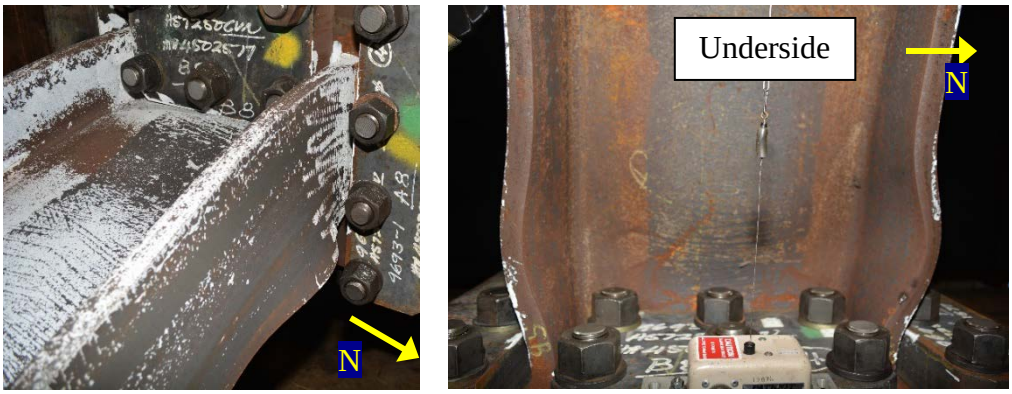

(a) Northwest Flange (b) West End

Figure 2.14 LTB-Induced Flange Local Buckling (Specimen 16M with W18×130 Section and C_a = 0.4)

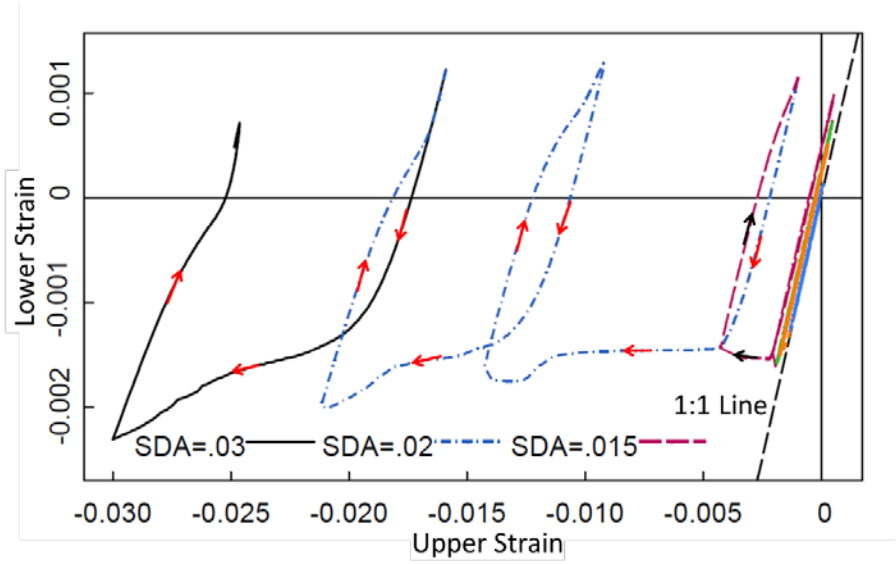

Figure 2.15 Nonuniform Strain Profile across the Northwest Flange [see Figure 2.13(b)]

(a) *SDA* = 0.015 rad (b) *SDA* = 0.02 rad (c) *SDA* = 0.03 rad

Figure 2.16 Nonuniform (or Sloped) Flaking of Whitewash at West End (Specimen 16M with W18×130 Section, C_a = 0.4)

3. DATA REDUCTION

3.1 Introduction

In NIST beam-column testing (details discussed in Chapter 2), the use of bolted end-plate connections to tie the specimens to reaction fixtures did not constitute ideal rigid boundary conditions; some relative rotations between the specimen ends and the reaction fixtures were observed. Flexibility of these connections varied in moment-rotation characteristics for each specimen and affected each specimen's responses differently. Thus, in order to investigate other variables of interest, it is necessary to remove this connection flexibility effect from the test responses. This thesis theoretically investigates elastic beam-column behavior corresponding to rigid- and flexible-end boundary conditions, utilizing the Timoshenko theory; theoretical expressions that considered both shear deformation and the second-order effects were derived and used to correct the test lateral-drift responses to eliminate the effect of end-connection flexibility. Once achieved, the corrected test data would represent the responses corresponding to ideal (or rigid) boundary conditions.

3.2 Theoretical Investigation of Elastic Beam-column Behavior

Elastic flexural stiffnesses of a prismatic beam-column are a function of boundary conditions and applied axial loads. Two boundary types were investigated in this theoretical study: (1) ideal or rigid boundary conditions, and (2) flexible or partially-restrained boundary conditions. Figure 3.1 and Figure 3.2 show the deformed configurations of fixed-fixed and fixed rotating columns, respectively, with respect to these two boundary types. Elastic flexural stiffnesses of these cases are investigated in this section with respect to Euler and Timoshenko theories. Euler beam theory assumes

negligible shear deformation, while Timoshenko beam theory accounts for the shear deformation by assuming a uniform shear stress profile in a cross-section. When the geometries of test specimens are considered in this study, results show that the effect of shear deformation on elastic flexural stiffnesses cannot be ignored. Slope-deflection equations and stiffness relationships of Timoshenko beam-columns with ideal and flexible end conditions are derived in Sections 3.2.2.2 and 3.2.2.3, respectively.

3.2.1 Euler Member

3.2.1.1 Euler Beam with Ideal Boundary Conditions

Euler assumptions state that plane sections remain plane and shear deformation is negligible. Following the displacement and force notations of a two-node member shown in Figure 3.3, the elastic flexural stiffness matrix, $\bar{\boldsymbol{K}}$, of an Euler beam with ideal boundary conditions is expressed as follows:

$$\begin{Bmatrix} V_1 \\ M_1 \\ V_2 \\ M_2 \end{Bmatrix} = \underbrace{\frac{EI}{L}\begin{bmatrix} \frac{12}{L^2} & \frac{6}{L} & -\frac{12}{L^2} & \frac{6}{L} \\ \frac{6}{L} & 4 & -\frac{6}{L} & 2 \\ -\frac{12}{L^2} & -\frac{6}{L} & \frac{12}{L^2} & -\frac{6}{L} \\ \frac{6}{L} & 2 & -\frac{6}{L} & 4 \end{bmatrix}}_{\bar{\boldsymbol{K}}} \begin{Bmatrix} v_1 \\ \alpha_1 \\ v_2 \\ \alpha_2 \end{Bmatrix} \tag{3.1}$$

This formulation neglects the axial load and shear deformation effects.

3.2.1.2 Euler Beam-Column with Ideal Boundary Conditions

When an axial load is applied to a member, the member's elastic flexural stiffness changes due to the second-order *P*-δ and *P*-Δ effects. Slope-deflection equations can be derived by applying Euler compatibility and constitutive law to equilibriums of a member

in its deformed configuration. This derivation is well established (e.g., Chen and Lui 1987); the flexural stiffness relationships of an Euler beam-column with ideal boundary conditions are:

$$\begin{Bmatrix} V_1 \\ M_1 \\ V_2 \\ M_2 \end{Bmatrix} = \underbrace{\begin{bmatrix} \bar{K}_{11} & \bar{K}_{12} & \bar{K}_{13} & \bar{K}_{14} \\ \bar{K}_{21} & \bar{K}_{22} & \bar{K}_{23} & \bar{K}_{24} \\ \bar{K}_{31} & \bar{K}_{32} & \bar{K}_{33} & \bar{K}_{34} \\ \bar{K}_{41} & \bar{K}_{42} & \bar{K}_{43} & \bar{K}_{44} \end{bmatrix}}_{\bar{\boldsymbol{K}}_{\boldsymbol{C}} \text{ or } \bar{\boldsymbol{K}}_{\boldsymbol{T}}} \begin{Bmatrix} v_1 \\ \alpha_1 \\ v_2 \\ \alpha_2 \end{Bmatrix} \tag{3.2}$$

where the stiffness matrix subscripts "*C*" and "*T*" distinguish the types of axial load being applied to the member, i.e., "Compression" and "Tension", respectively. Regardless of the axial load directions, the axial load magnitude (i.e., absolute value) P can be normalized as

$$\varphi = \sqrt{P/EI} \tag{3.3}$$

and in a dimensionless form as

$$\Phi = \varphi L = \left(\sqrt{P/EI}\right)L \tag{3.4}$$

The two parameters defined above are used to simplify expressions of both beam-columns under axial compression and axial tension.

Member with Axial Compression

Defining

$$\bar{\Psi}_C = 2(1 - \cos\Phi) - \Phi\sin\Phi \tag{3.5}$$

coefficients for the symmetric flexural stiffness matrix, $\bar{\boldsymbol{K}}_{\boldsymbol{C}}$, in Eq. (3.2) are

$$\bar{K}_{C,11} = \frac{EI}{L^3\bar{\Psi}_C}\Phi^3 \sin\Phi$$

$$\bar{K}_{C,12} = \frac{EI}{L^2\bar{\Psi}_C}\Phi^2(1-\cos\Phi)$$

$$\bar{K}_{C,22} = \frac{EI}{L\bar{\Psi}_C}\Phi(\sin\Phi - \Phi\cos\Phi)$$

$$\bar{K}_{C,24} = \frac{EI}{L\bar{\Psi}_C}\Phi(\Phi - \sin\Phi) \tag{3.6}$$

$$-\bar{K}_{C,13} = -\bar{K}_{C,31} = \bar{K}_{C,33} = \bar{K}_{C,11}$$

$$-\bar{K}_{C,23} = -\bar{K}_{C,32} = -\bar{K}_{C,34} = -\bar{K}_{C,43} = \bar{K}_{C,14} = \bar{K}_{C,21} = \bar{K}_{C,41} = \bar{K}_{C,12}$$

$$\bar{K}_{C,44} = \bar{K}_{C,22};\ \bar{K}_{C,42} = \bar{K}_{C,24}$$

Following expressions predict internal moment and shear along the member length when axial compression is present:

(a) when $v_1 = 1$, $v_2 = 0$, $\alpha_1 = 0$, and $\alpha_2 = 0$,

$$M_{v_1}(x) = \frac{EI}{L^2\bar{\Psi}_C}\Phi^2\{\cos[\varphi(L-x)] - \cos(\varphi x)\}$$

$$V_{v_1}(x) = -\frac{EI}{L^3\bar{\Psi}_C}\Phi^3 \sin\Phi$$

(b) when $v_1 = 0$, $v_2 = 0$, $\alpha_1 = 1$, and $\alpha_2 = 0$,

$$M_{\alpha_1}(x) = \frac{EI}{L\bar{\Psi}_C}\Phi\{\Phi\cos[\varphi(L-x)] - \sin[\varphi(L-x)] - \sin(\varphi x)\} \tag{3.7}$$

$$V_{\alpha_1}(x) = -\frac{EI}{L^2\bar{\Psi}_C}\Phi^2(1-\cos\Phi)$$

(c) when $v_1 = 0$, $v_2 = 1$, $\alpha_1 = 0$, and $\alpha_2 = 0$,

$$M_{v_2}(x) = -M_{v_1}(x)$$

$$V_{v_2}(x) = -V_{v_1}(x)$$

(d) when $v_1 = 0$, $v_2 = 0$, $\alpha_1 = 0$, and $\alpha_2 = 1$,

$$M_{\alpha_2}(x) = -\frac{EI}{L\bar{\Psi}_C}\Phi\{\Phi\cos(\varphi x) - \sin(\varphi x) - \sin[\varphi(L-x)]\}$$

$$V_{\alpha_2}(x) = V_{\alpha_1}(x)$$

Using superposition, internal moment and shear along the member length can be determined if the end lateral displacements (v_1 and v_2) and rotations (α_1 and α_2) are known:

$$M_{total}(x) = M_{v_1}(x)v_1 + M_{\alpha_1}(x)\alpha_1 + M_{v_2}(x)v_2 + M_{\alpha_2}(x)\alpha_2 \tag{3.8}$$

$$V_{total}(x) = V_{v_1}(x)v_1 + V_{\alpha_1}(x)\alpha_1 + V_{v_2}(x)v_2 + V_{\alpha_2}(x)\alpha_2 \tag{3.9}$$

Eqs. (3.8) and (3.9) are the most general forms when all four degrees of freedom are unrestrained. They can also be written in the stiffness matrix format as in Eq. (3.2) for $x = 0$ and $x = L$ to establish the coefficients for $\bar{\boldsymbol{K}}_{\boldsymbol{C}}$. $\bar{K}_{C,11}$ predicts the theoretical Euler lateral stiffness considering stiffness reduction due to axial compression for specimens with ideal fixed-fixed boundary conditions. In testing, flexibility of end connections was observed. Therefore, elastic behavior of an Euler beam-column with flexible end restraints is studied in Section 3.2.1.3 to address this issue.

Member with Axial Tension

Defining

$$\bar{\Psi}_T = -2(1 - \cosh\Phi) - \Phi\sinh\Phi \tag{3.10}$$

coefficients for the symmetric flexural stiffness matrix, $\bar{\boldsymbol{K}}_{\boldsymbol{T}}$, in Eq. (3.2) are

$$\overline{K}_{T,11} = -\frac{EI}{L^3\overline{\Psi}_T}\Phi^3 \sinh\Phi$$

$$\overline{K}_{T,12} = \frac{EI}{L^2\overline{\Psi}_T}\Phi^2(1-\cosh\Phi)$$

$$\overline{K}_{T,22} = \frac{EI}{L\overline{\Psi}_T}\Phi(\sinh\Phi - \Phi\cosh\Phi)$$

$$\overline{K}_{T,24} = \frac{EI}{L\overline{\Psi}_T}\Phi(\Phi - \sinh\Phi) \tag{3.11}$$

$$-\overline{K}_{T,13} = -\overline{K}_{T,31} = \overline{K}_{T,33} = \overline{K}_{T,11}$$

$$-\overline{K}_{T,23} = -\overline{K}_{T,32} = -\overline{K}_{T,34} = -\overline{K}_{T,43} = \overline{K}_{T,14} = \overline{K}_{T,21} = \overline{K}_{T,41} = \overline{K}_{T,12}$$

$$\overline{K}_{T,44} = \overline{K}_{T,22};\ \overline{K}_{T,42} = \overline{K}_{T,24}$$

The following expresses moment and shear equations along the member length:

(a) when $v_1 = 1$, $v_2 = 0$, $\alpha_1 = 0$, and $\alpha_2 = 0$,

$$M_{v_1}(x) = \frac{EI}{L^2\overline{\Psi}_T}\Phi^2\{\cosh[\varphi(L-x)] - \cosh(\varphi x)\}$$

$$V_{v_1}(x) = \frac{EI}{L^3\overline{\Psi}_T}\Phi^3 \sinh\Phi$$

(b) when $v_1 = 0$, $v_2 = 0$, $\alpha_1 = 1$, and $\alpha_2 = 0$,

$$M_{\alpha_1}(x) = \frac{EI}{L\overline{\Psi}_T}\Phi\{\Phi\cosh[\varphi(L-x)] - \sinh[\varphi(L-x)] - \sinh(\varphi x)\} \tag{3.12}$$

$$V_{\alpha_1}(x) = -\frac{EI}{L^2\overline{\Psi}_T}\Phi^2(1-\cosh\Phi)$$

(c) when $v_1 = 0$, $v_2 = 1$, $\alpha_1 = 0$, and $\alpha_2 = 0$,

$$M_{v_2}(x) = -M_{v_1}(x)$$

$$V_{v_2}(x) = -V_{v_1}(x)$$

(d) when $v_1 = 0$, $v_2 = 0$, $\alpha_1 = 0$, and $\alpha_2 = 1$,

$$M_{\alpha_2}(x) = -\frac{EI}{L\overline{\Psi}_T}\Phi\{\Phi\cosh(\varphi x) - \sinh(\varphi x) - \sinh[\varphi(L-x)]\}$$

$$V_{\alpha_2}(x) = V_{\alpha_1}(x)$$

3.2.1.3 Euler Beam-Column with Flexible Boundary Conditions

Ideal boundary conditions are difficult to achieve in full-scale testing in this research program. To predict elastic behavior of an Euler beam-column with flexible end restraints, end rotational springs with equal stiffness of

$$K_\theta = \beta\left(\frac{EI}{L}\right) \tag{3.13}$$

are included in the theoretical derivation of the member flexural stiffness matrix as in Eq. (3.14).

$$\begin{Bmatrix} V_1 \\ M_1 \\ V_2 \\ M_2 \end{Bmatrix} = \underbrace{\begin{bmatrix} \overline{K}'_{11} & \overline{K}'_{12} & \overline{K}'_{13} & \overline{K}'_{14} \\ \overline{K}'_{21} & \overline{K}'_{22} & \overline{K}'_{23} & \overline{K}'_{24} \\ \overline{K}'_{31} & \overline{K}'_{32} & \overline{K}'_{33} & \overline{K}'_{34} \\ \overline{K}'_{41} & \overline{K}'_{42} & \overline{K}'_{43} & \overline{K}'_{44} \end{bmatrix}}_{\overline{\boldsymbol{K}}'_{\boldsymbol{C}} \text{ or } \overline{\boldsymbol{K}}'_{\boldsymbol{T}}} \begin{Bmatrix} v_1 \\ \theta_1 \\ v_2 \\ \theta_2 \end{Bmatrix} \tag{3.14}$$

The procedure to establish the flexural stiffness coefficients is similar to that presented in Section 3.2.2.3; the only difference is that the derivation in this section is based on the Euler beam assumptions, which neglect the effect of shear deformation.

Member with Axial Compression

Defining

$$\overline{\Psi}'_C = 2(\beta^2 + \beta\Phi^2)(1 - \cos\Phi) - \Phi(\beta^2 - 2\beta - \Phi^2)\sin\Phi - 2\beta\Phi^2 \tag{3.15}$$

coefficients for the symmetric flexural stiffness matrix, $\overline{\boldsymbol{K}}'_{\boldsymbol{C}}$, are derived as follows:

$$\bar{K}'_{C,11} = \frac{EI}{L^3}\left\{\frac{\Phi^3[\beta \sin\Phi - \Phi(1-\cos\Phi)]}{(2\beta+\Phi^2)(1-\cos\Phi) - \beta\Phi\sin\Phi}\right\}$$

$$\bar{K}'_{C,12} = \frac{EI}{L^2}\left[\frac{\beta\Phi^2(1-\cos\Phi)}{(2\beta+\Phi^2)(1-\cos\Phi) - \beta\Phi\sin\Phi}\right]$$

$$\bar{K}'_{C,22} = \frac{EI}{L\bar{\Psi}'_C}\Phi[(\beta^2+\beta\Phi^2)\sin\Phi - \beta^2\Phi\cos\Phi]$$

$$\bar{K}'_{C,24} = \frac{EI}{L\bar{\Psi}'_C}\beta^2\Phi(\Phi - \sin\Phi) \tag{3.16}$$

$$-\bar{K}'_{C,13} = -\bar{K}'_{C,31} = \bar{K}'_{C,33} = \bar{K}'_{C,11}$$

$$-\bar{K}'_{C,23} = -\bar{K}'_{C,32} = -\bar{K}'_{C,34} = -\bar{K}'_{C,43} = \bar{K}'_{C,14} = \bar{K}'_{C,21} = \bar{K}'_{C,41} = \bar{K}'_{C,12}$$

$$\bar{K}'_{C,44} = \bar{K}'_{C,22};\ \bar{K}'_{C,42} = \bar{K}'_{C,24}$$

Eq. (3.17) expresses internal moment and shear along the member length:

(a) when $v_1 = 1$, $v_2 = 0$, $\theta_1 = 0$, and $\theta_2 = 0$,

$$M_{v_1}(x) = \frac{EI}{L^2}\left\{\frac{\beta\Phi^2\{\cos[\varphi(L-x)] - \cos(\varphi x)\}}{(2\beta+\Phi^2)(1-\cos\Phi) - \beta\Phi\sin\Phi}\right\}$$

$$V_{v_1}(x) = \frac{EI}{L^3}\left\{\frac{\Phi^3[\Phi(1-\cos\Phi) - \beta\sin\Phi]}{(2\beta+\Phi^2)(1-\cos\Phi) - \beta\Phi\sin\Phi}\right\}$$

(b) when $v_1 = 0$, $v_2 = 0$, $\theta_1 = 1$, and $\theta_2 = 0$,

$$M_{\theta_1}(x) = \frac{EI}{L\bar{\Psi}'_C}\Phi\{\beta^2\Phi\cos[\varphi(L-x)] - (\beta^2+\beta\Phi^2)\sin[\varphi(L-x)] - \beta^2\sin(\varphi x)\} \tag{3.17}$$

$$V_{\theta_1}(x) = -\frac{EI}{L^2}\left[\frac{\beta\Phi^2(1-\cos\Phi)}{(2\beta+\Phi^2)(1-\cos\Phi) - \beta\Phi\sin\Phi}\right]$$

(c) when $v_1 = 0$, $v_2 = 1$, $\theta_1 = 0$, and $\theta_2 = 0$,

$$M_{v_2}(x) = -M_{v_1}(x)$$

$$V_{v_2}(x) = -V_{v_1}(x)$$

(d) when $v_1 = 0$, $v_2 = 0$, $\theta_1 = 0$, and $\theta_2 = 1$,

$$M_{\theta_2}(x) = -\frac{EI}{L\overline{\Psi}'_C}\Phi\{\beta^2\Phi\cos(\varphi x) - (\beta^2 + \beta\Phi^2)\sin(\varphi x) - \beta^2\sin[\varphi(L-x)]\}$$

$$V_{\theta_2}(x) = V_{\alpha_1}(x)$$

Member with Axial Tension

Defining

$$\overline{\Psi}'_T = -2(\beta^2 - \beta\Phi^2)(1-\cosh\Phi) - \Phi(\beta^2 - 2\beta + \Phi^2)\sinh\Phi - 2\beta\Phi^2 \qquad (3.18)$$

coefficients for the symmetric flexural stiffness matrix, $\overline{\boldsymbol{K}}'_{\boldsymbol{T}}$, are derived as follows:

$$\overline{K}'_{T,11} = -\frac{EI}{L^3}\left\{\frac{\Phi^3[\beta\sinh\Phi - \Phi(1-\cosh\Phi)]}{(-2\beta+\Phi^2)(1-\cosh\Phi) - \beta\Phi\sinh\Phi}\right\}$$

$$\overline{K}'_{T,12} = \frac{EI}{L^2}\left[\frac{\beta\Phi^2(1-\cosh\Phi)}{(-2\beta+\Phi^2)(1-\cosh\Phi) - \beta\Phi\sinh\Phi}\right]$$

$$\overline{K}'_{T,22} = \frac{EI}{L\overline{\Psi}'_T}\Phi[(\beta^2 - \beta\Phi^2)\sinh\Phi - \beta^2\Phi\cosh\Phi]$$

$$\overline{K}'_{T,24} = \frac{EI}{L\overline{\Psi}'_T}\beta^2\Phi(\Phi - \sinh\Phi) \qquad (3.19)$$

$$-\overline{K}'_{T,13} = -\overline{K}'_{T,31} = \overline{K}'_{T,33} = \overline{K}'_{T,11}$$

$$-\overline{K}'_{T,23} = -\overline{K}'_{T,32} = -\overline{K}'_{T,34} = -\overline{K}'_{T,43} = \overline{K}'_{T,14} = \overline{K}'_{T,21} = \overline{K}'_{T,41} = \overline{K}'_{T,12}$$

$$\overline{K}'_{T,44} = \overline{K}'_{T,22};\ \overline{K}'_{T,42} = \overline{K}'_{T,24}$$

Eq. (3.20) expresses internal moment and shear along the member length:

(a) when $v_1 = 1$, $v_2 = 0$, $\alpha_1 = 0$, and $\alpha_2 = 0$,

$$M_{v_1}(x) = \frac{EI}{L^2}\left\{\frac{\beta\Phi^2\{\cosh[\varphi(L-x)] - \cosh(\varphi x)\}}{(-2\beta + \Phi^2)(1-\cosh\Phi) - \beta\Phi\sinh\Phi}\right\}$$

$$V_{v_1}(x) = \frac{EI}{L^3}\left\{\frac{\Phi^3[-\Phi(1-\cosh\Phi) + \beta\sinh\Phi]}{(-2\beta + \Phi^2)(1-\cosh\Phi) - \beta\Phi\sinh\Phi}\right\}$$

(b) when $v_1 = 0$, $v_2 = 0$, $\alpha_1 = 1$, and $\alpha_2 = 0$,

$$M_{\alpha_1}(x) = \frac{EI}{L\bar{\Psi}_T'}\Phi\{\beta^2\Phi\cosh[\varphi(L-x)] - (\beta^2 - \beta\Phi^2)\sinh[\varphi(L-x)] - \beta^2\sinh(\varphi x)\}$$

$$V_{\alpha_1}(x) = -\frac{EI}{L^2}\left[\frac{\beta\Phi^2(1-\cosh\Phi)}{(-2\beta + \Phi^2)(1-\cosh\Phi) - \beta\Phi\sinh\Phi}\right] \tag{3.20}$$

(c) when $v_1 = 0$, $v_2 = 1$, $\alpha_1 = 0$, and $\alpha_2 = 0$,

$$M_{v_2}(x) = -M_{v_1}(x)$$

$$V_{v_2}(x) = -V_{v_1}(x)$$

(d) when $v_1 = 0$, $v_2 = 0$, $\alpha_1 = 0$, and $\alpha_2 = 1$,

$$M_{\alpha_2}(x) = -\frac{EI}{L\bar{\Psi}_T'}\Phi\{\beta^2\Phi\cosh(\varphi x) - (\beta^2 - \beta\Phi^2)\sinh(\varphi x) - \beta^2\sinh[\varphi(L-x)]\}$$

$$V_{\alpha_2}(x) = V_{\alpha_1}(x)$$

3.2.2 Timoshenko Member

3.2.2.1 Timoshenko Beam with Ideal Boundary Conditions

Euler beam theory does not consider the effect of shear deformation. Timoshenko beam theory represents a simplification of more precise beam theories that accounts for

shear deformations by assuming a uniform shear stress distribution in a cross-section. Constitutive law for shear force is expressed as (Graff 1975)

$$V = GA_s\gamma \tag{3.21}$$

where G is the shear modulus, γ is the shear strain, and A_s $(= kA)$ is the shear area; k is the Timoshenko shear coefficient, which varies based on the shape of the cross-section. For an I-section bent about its strong-axis, k can be determined as follows (Cowper 1966):

$$k = \frac{10(1+\nu)(1+3m)^2}{(12+72m+150m^2+90m^3)+\nu(11+66m+135m^2+90m^3)+30n^2(m+m^2)+5\nu n^2(8m+9m^2)} \tag{3.22}$$

where Poisson's ratio $\nu = 0.3$ for steel, $m = \frac{2b_f t_f}{h_0 t_w}$, $h_0 =$ distance between the flange centroids, and $n = \frac{b_f}{h_0}$.

Flexural stiffness relationships of a two-node Timoshenko beam are well established as follows (e.g., Przemieniecki 1985):

$$\begin{Bmatrix} V_1 \\ M_1 \\ V_2 \\ M_2 \end{Bmatrix} = \underbrace{\frac{EI}{L}\begin{bmatrix} \frac{12}{(1+\Pi)L^2} & \frac{6}{(1+\Pi)L} & -\frac{12}{(1+\Pi)L^2} & \frac{6}{(1+\Pi)L} \\ \frac{6}{(1+\Pi)L} & \frac{4+\Pi}{1+\Pi} & -\frac{6}{(1+\Pi)L} & \frac{2-\Pi}{1+\Pi} \\ -\frac{12}{(1+\Pi)L^2} & -\frac{6}{(1+\Pi)L} & \frac{12}{(1+\Pi)L^2} & -\frac{6}{(1+\Pi)L} \\ \frac{6}{(1+\Pi)L} & \frac{2-\Pi}{1+\Pi} & -\frac{6}{(1+\Pi)L} & \frac{4+\Pi}{1+\Pi} \end{bmatrix}}_{\boldsymbol{K}} \begin{Bmatrix} v_1 \\ \alpha_1 \\ v_2 \\ \alpha_2 \end{Bmatrix} \tag{3.23}$$

where

$$\Pi = \frac{12EI}{GA_sL^2} \tag{3.24}$$

K_{11} represents the Timoshenko lateral stiffness neglecting axial load effect. The elastic flexural stiffnesses of a Timoshenko beam-column are derived in the following section.

3.2.2.2 Timoshenko Beam-Column with Ideal Boundary Conditions

To establish the governing differential equations for a Timoshenko beam-column, Timoshenko compatibility and constitutive laws are applied to equilibriums of a member in its deformed configuration. The derived flexural stiffness relationships are shown in the following form:

$$\begin{Bmatrix} V_1 \\ M_1 \\ V_2 \\ M_2 \end{Bmatrix} = \underbrace{\begin{bmatrix} K_{11} & K_{12} & K_{13} & K_{14} \\ K_{21} & K_{22} & K_{23} & K_{24} \\ K_{31} & K_{32} & K_{33} & K_{34} \\ K_{41} & K_{42} & K_{43} & K_{44} \end{bmatrix}}_{\boldsymbol{K_C} \text{ or } \boldsymbol{K_T}} \begin{Bmatrix} v_1 \\ \alpha_1 \\ v_2 \\ \alpha_2 \end{Bmatrix} \tag{3.25}$$

Member with Axial Compression

Figure 3.4 depicts the free body diagram of an axially loaded beam in its deformed configuration. The equilibriums of an infinitesimal member length can be expressed as follows:

$$\frac{dV}{dx} + w(x) = 0 \tag{3.26}$$

$$\frac{dM}{dx} + V(x) + P\frac{dv}{dx} = 0 \tag{3.27}$$

Timoshenko compatibility and constitutive laws can be expressed as follows:

$$M(x) = EI(x)\frac{d\alpha}{dx} \tag{3.28}$$

$$V(x) = GA_s(x)\left[\frac{dv}{dx} - \alpha(x)\right] \tag{3.29}$$

Substitute Eqs. (3.28) and (3.29) into Eq. (3.27) to derive a lateral displacement and flexural rotation relationship as follows:

$$\frac{dv}{dx} = \frac{-1}{\rho + \varphi^2}\left[\frac{d^2\alpha}{dx^2} - \rho\alpha(x)\right] \tag{3.30a}$$

where

$$\rho = \frac{GA_s}{EI} \tag{3.30b}$$

Differentiating Eq. (3.27), substituting in Eq. (3.30a), and setting $w(x) = 0$ gives a third-order ordinary differential equation for flexural rotation below.

$$\frac{d^3\alpha}{dx^3} + \varphi^2\frac{d\alpha}{dx} = 0 \tag{3.31}$$

The solution of this equation takes the form of $\alpha(x) = Ce^{\lambda x}$. Substituting this into Eq. (3.31) gives the characteristic equation for the Timoshenko member under compression:

$$(\lambda^3 + \varphi^2\lambda)Ce^{\lambda x} = 0 \tag{3.32}$$

The solution is

$$\lambda = 0, -i\varphi, i\varphi \tag{3.33}$$

Thus, the general solution for the slope equation can be expressed as follows:

$$\alpha(x) = C_1e^{i\varphi x} + C_2e^{-i\varphi x} + C_3 \tag{3.34a}$$

or

$$\alpha(x) = C_1\sin\varphi x + C_2\cos\varphi x + C_3 \tag{3.34b}$$

Substituting Eq. (3.34b) into Eq. (3.30a) and integrating once gives a deflection equation below.

$$v(x) = \frac{-1}{\varphi}\left[C_1\cos\varphi x - C_2\sin\varphi x - \frac{\varphi\rho}{\varphi^2 + \rho}C_3x\right] + C_4 \tag{3.35}$$

To derive the flexural stiffness matrix of a two-node element with four degrees of freedom (lateral displacement and rotation at each end), four sets of boundary conditions

are applied to the slope-deflection equations. The resulting system of equations are solved to determine the unknown coefficients. Firstly, a unit end rotation is imposed at the left end (node 1) of the element while other degrees of freedom remain fixed.

$$v(0) = 0;\ v(L) = 0; \alpha(0) = 1; \alpha(L) = 0 \tag{3.36}$$

Solving the above system of equations gives:

$$\begin{gathered} C_1 = \frac{1}{\Psi_C}[-(1+\mu)\sin\Phi + \Phi\cos\Phi] \\ C_2 = \frac{1}{\Psi_C}[(1+\mu)(1-\cos\Phi) - \Phi\sin\Phi] \\ C_3 = \frac{1}{\Psi_C}(1+\mu)(1-\cos\Phi) \\ C_4 = \frac{L}{\Phi}C_1 \end{gathered} \tag{3.37}$$

where dimensionless factors are defined as

$$\mu = \frac{P}{GA_s} \tag{3.38}$$

$$\Psi_C = 2(1+\mu)(1-\cos\Phi) - \Phi\sin\Phi \tag{3.39}$$

Substituting Eq. (3.37) into Eqs. (3.34b) and (3.35) gives closed-form solutions for the lateral displacement and flexural rotation along the member length corresponding to the applied unit rotation at node 1 [i.e., $\alpha_1 = \alpha(0) = 1$]. Applying the Timoshenko constitutive law, closed-form solutions for the moment $M_{\alpha_1}(x)$ and shear $V_{\alpha_1}(x)$ along the member length can be expressed using Eqs. (3.28) and (3.27) as:

$$\begin{gathered} M_{\alpha_1}(x) = \frac{EI}{L\Psi_C}\Phi\{\Phi\cos[\varphi(L-x)] - (1+\mu)\sin[\varphi(L-x)] - (1+\mu)\sin(\varphi x)\} \\ V_{\alpha_1}(x) = -\frac{EI}{L^2\Psi_C}\Phi^2(1-\cos\Phi) \end{gathered} \tag{3.40}$$

This same process is carried out for the three other cases: (a) a unit lateral displacement is applied at node 1 [i.e., $v_1 = v(0) = 1$] while other DOFs remain fixed, (b) a unit lateral displacement is applied at node 2 [i.e., $v_2 = v(L) = 1$] while other DOFs remain fixed, and (c) a unit rotation is applied at node 2 [i.e., $\alpha_2 = \alpha(L) = 1$] while other DOFs remain fixed. Mathematically, these boundary conditions can be expressed as follows:

$$v(0) = 1;\ v(L) = 0;\ \alpha(0) = 0;\ \alpha(L) = 0 \tag{3.41}$$

$$v(0) = 0;\ v(L) = 1;\ \alpha(0) = 0;\ \alpha(L) = 0 \tag{3.42}$$

$$v(0) = 0;\ v(L) = 0; \alpha(0) = 0;\ \alpha(L) = 1 \tag{3.43}$$

Solving the above three sets of boundary conditions yields expressions for $M_{v_1}(x)$ and $V_{v_1}(x)$, $M_{v_2}(x)$ and $V_{v_2}(x)$, as well as $M_{\alpha_2}(x)$ and $V_{\alpha_2}(x)$, respectively. The results are shown below.

$$\begin{gathered} M_{v_1}(x) = \frac{EI}{L^2\Psi_C}\Phi^2(1+\mu)\{\cos[\varphi(L-x)] - \cos(\varphi x)\} \\ V_{v_1}(x) = -\frac{EI}{L^3\Psi_C}\Phi^3 \sin\Phi \\ M_{v_2}(x) = -M_{v_1}(x) \\ V_{v_2}(x) = -V_{v_1}(x) \\ M_{\alpha_2}(x) = -\frac{EI}{L\Psi_C}\Phi\{\Phi\cos(\varphi x) - (1+\mu)\sin(\varphi x) - (1+\mu)\sin[\varphi(L-x)]\} \\ V_{\alpha_2}(x) = V_{\alpha_1}(x) \end{gathered} \tag{3.44}$$

Eqs. (3.40) and (3.44) can also be expressed in the stiffness matrix format as in Eq. (3.25) to establish the flexural stiffness coefficients as follows:

$$K_{C,11} = \frac{EI}{L^3\Psi_C}\Phi^3 \sin\Phi$$

$$K_{C,12} = \frac{EI}{L^2\Psi_C}\Phi^2(1-\cos\Phi)$$

$$K_{C,21} = \frac{EI}{L^2\Psi_C}\Phi^2(1+\mu)(1-\cos\Phi)$$

$$K_{C,22} = \frac{EI}{L\Psi_C}\Phi[(1+\mu)\sin\Phi - \Phi\cos\Phi] \tag{3.45}$$

$$K_{C,24} = \frac{EI}{L\Psi_C}\Phi[\Phi - (1+\mu)\sin\Phi]$$

$$-K_{C,13} = -K_{C,31} = K_{C,33} = K_{C,11}$$

$$-K_{C,32} = -K_{C,34} = K_{C,14} = K_{C,12}$$

$$-K_{C,23} = -K_{C,43} = K_{C,41} = K_{C,21}$$

$$K_{C,44} = K_{C,22};\ K_{C,42} = K_{C,24}$$

Member with Axial Tension

Eqs. (3.26) and (3.27) express the equilibriums of an infinitesimal member length in its deformed configuration under axial compression. Under axial tension with the magnitude P, Eq. (3.27) becomes

$$\frac{dM}{dx} + V(x) - P\frac{dv}{dx} = 0 \tag{3.46}$$

The same Timoshenko compatibility and constitutive laws as discussed before are applied to Eqs. (3.26) and (3.46), which give:

$$\frac{dv}{dx} = \frac{-1}{\rho - \varphi^2}\left[\frac{d^2\alpha}{dx^2} - \rho\alpha(x)\right] \tag{3.47}$$

Differentiating Eq. (3.46), substituting into Eq. (3.47), and setting $w(x) = 0$ gives a third-order ordinary differential equation below.

$$\frac{d^3\alpha}{dx^3} - \varphi^2 \frac{d\alpha}{dx} = 0 \tag{3.48}$$

The solution of this equation takes the form of $\alpha(x) = Ce^{\lambda x}$. Substituting this into Eq. (3.48) results in the characteristic equation for the Timoshenko member under tension:

$$(\lambda^3 - \varphi^2\lambda)Ce^{\lambda x} = 0 \tag{3.49}$$

The solution is

$$\lambda = 0, -\varphi, \varphi \tag{3.50}$$

Thus, the general solutions for the slope-deflection equations can be expressed as follows:

$$\alpha(x) = C_1 e^{\varphi x} + C_2 e^{-\varphi x} + C_3 \tag{3.51}$$

$$v(x) = \frac{-1}{\varphi}\left[C_1 e^{\varphi x} - C_2 e^{-\varphi x} - \frac{\varphi\rho}{\varphi^2 - \rho} C_3 x\right] + C_4 \tag{3.52}$$

The same process as described before is used to derive the flexural stiffness matrix. Moment and shear equations along the member length can be expressed as follows:

(a) when $v_1 = 1$, $v_2 = 0$, $\alpha_1 = 0$, and $\alpha_2 = 0$,

$$M_{v_1}(x) = \frac{EI}{L^2\Psi_T}\Phi^2(1-\mu)\{\cosh[\varphi(L-x)] - \cosh(\varphi x)\}$$

$$V_{v_1}(x) = \frac{EI}{L^3\Psi_T}\Phi^3 \sinh\Phi$$

(b) when $v_1 = 0$, $v_2 = 0$, $\alpha_1 = 1$, and $\alpha_2 = 0$,

$$M_{\alpha_1}(x) = \frac{EI}{L\Psi_T}\Phi\{\Phi\cosh[\varphi(L-x)] - (1-\mu)\sinh[\varphi(L-x)] - (1-\mu)\sinh(\varphi x)\} \tag{3.53}$$

$$V_{\alpha_1}(x) = -\frac{EI}{L^2\Psi_T}\Phi^2(1-\cosh\Phi)$$

(c) when $v_1 = 0$, $v_2 = 1$, $\alpha_1 = 0$, and $\alpha_2 = 0$,

$$M_{v_2}(x) = -M_{v_1}(x)$$

$$V_{v_2}(x) = -V_{v_1}(x)$$

(d) when $v_1 = 0$, $v_2 = 0$, $\alpha_1 = 0$, and $\alpha_2 = 1$,

$$M_{\alpha_2}(x) = -\frac{EI}{L\Psi_T}\Phi\{\Phi\cosh(\varphi x) - (1-\mu)\sinh(\varphi x) - (1-\mu)\sinh[\varphi(L-x)]\}$$

$$V_{\alpha_2}(x) = V_{\alpha_1}(x)$$

where

$$\Psi_T = -2(1-\mu)(1-\cosh\Phi) - \Phi\sinh\Phi \tag{3.54}$$

Finally, the flexural stiffness matrix, $\boldsymbol{K_T}$, can be expressed in the form of Eq. (3.25), where

$$K_{T,11} = -\frac{EI}{L^3\Psi_T}\Phi^3\sinh\Phi$$

$$K_{T,12} = \frac{EI}{L^2\Psi_T}\Phi^2(1-\cosh\Phi)$$

$$K_{T,21} = \frac{EI}{L^2\Psi_T}\Phi^2(1-\mu)(1-\cosh\Phi)$$

$$K_{T,22} = \frac{EI}{L\Psi_T}\Phi[(1-\mu)\sinh\Phi - \Phi\cosh\Phi]$$

$$K_{T,24} = \frac{EI}{L\Psi_T}\Phi[\Phi - (1-\mu)\sinh\Phi] \tag{3.55}$$

$$-K_{T,13} = -K_{T,31} = K_{T,33} = K_{T,11}$$

$$-K_{T,32} = -K_{T,34} = K_{T,14} = K_{T,12}$$

$$-K_{T,23} = -K_{T,43} = K_{T,41} = K_{T,21}$$

$$K_{T,44} = K_{T,22};\ K_{T,42} = K_{T,24}$$

3.2.2.3 Timoshenko Beam-Column with Flexible Boundary Conditions

Chapter 2 describes boundary conditions of the beam-column test specimens. Due to out-of-plane flexibility of the end plates and elongation of the pretensioned rods, unintended rotations at column ends were unavoidable during testing. To remove the rigid body motion caused by these rotations from the measured lateral drift, a data reduction procedure is presented in Section 3.3. The process involves analyzing the actual testing condition to include the effect of connection flexibility. To provide a theoretical basis for the proposed data reduction procedure, behavior of a beam-column with end rotational springs is presented herein. Figure 3.5 shows the system of a member with end rotational springs, comprising of four nodes and eight degrees of freedom. The rotational spring stiffness constant is assumed equal at both ends in the form of $\beta(EI/L)$. Two approaches were used in establishing stiffness relationships of the system: (1) the governing differential equations discussed in Section 3.2.2.2 were re-solved using different sets of boundary conditions, and (2) the method of stiffness matrix condensation was implemented on the stiffness matrices $\boldsymbol{K_C}$ and $\boldsymbol{K_T}$ already derived in Section 3.2.2.2. Both approaches gave consistent results.

Method of Differential Equations

Regarding the first approach, the unknown coefficients in Eqs. (3.34b) and (3.35) can be re-solved based on new sets of boundary conditions that take into consideration the end rotational springs.

Figure 3.6 demonstrates the relationship between the spring forces and the member internal moments at ends corresponding to the application of a unit end rotation at node 1 [see Eq. (3.56)]. Ultimately, four new sets of boundary conditions corresponding to the

applications of a unit rotation and a unit lateral displacement at each end can be expressed as follow:

$$v(0) = 0;\ v(L) = 0;$$
$$\frac{\beta EI}{L}[1 - \alpha(0)] = -EI\left.\frac{d\alpha}{dx}\right|_{x=0};\ \frac{\beta EI}{L}[0 - \alpha(L)] = EI\left.\frac{d\alpha}{dx}\right|_{x=L} \tag{3.56}$$

$$v(0) = 0;\ v(L) = 0;$$
$$\frac{\beta EI}{L}[0 - \alpha(0)] = -EI\left.\frac{d\alpha}{dx}\right|_{x=0};\ \frac{\beta EI}{L}[1 - \alpha(L)] = EI\left.\frac{d\alpha}{dx}\right|_{x=L} \tag{3.57}$$

$$v(0) = 1;\ v(L) = 0;$$
$$\frac{\beta EI}{L}[0 - \alpha(0)] = -EI\left.\frac{d\alpha}{dx}\right|_{x=0};\ \frac{\beta EI}{L}[0 - \alpha(L)] = EI\left.\frac{d\alpha}{dx}\right|_{x=L} \tag{3.58}$$

$$v(0) = 0;\ v(L) = 1;$$
$$\frac{\beta EI}{L}[0 - \alpha(0)] = -EI\left.\frac{d\alpha}{dx}\right|_{x=0};\ \frac{\beta EI}{L}[0 - \alpha(L)] = EI\left.\frac{d\alpha}{dx}\right|_{x=L} \tag{3.59}$$

Solving the above system of equations and repeating the same process as described in Section 3.2.2.2 give the flexural stiffness matrix of a Timoshenko beam-column with flexible boundary conditions, $\boldsymbol{K'}$. Results are the same as those derived from the method of stiffness matrix condensation.

Method of Stiffness Matrix Condensation

$\boldsymbol{K'}$ can also be derived using the matrix condensation method (McGuire et al. 2014). The flexural stiffness coefficients in $\boldsymbol{K_C}$ or $\boldsymbol{K_T}$ derived in Section 3.2.2.2 can be assembled into the stiffness relationships of the system shown in Figure 3.5 to study the effect of flexible boundary conditions. This is achieved by mobilizing one degree of freedom at a time with a unit displacement (while others remain fixed) to formulate each column of the

stiffness matrix in Eq. (3.60). Enforcing the equilibrium requirements $V_1 = V_i$ and $V_2 = V_j$ and the compatibility requirements $v_1 = v_i$ and $v_2 = v_j$ gives the following:

$$\begin{Bmatrix} M_i \\ M_j \\ V_1 \\ M_1 \\ V_2 \\ M_2 \end{Bmatrix} = \left[\begin{array}{cc|cccc} K_{22}+\frac{\beta EI}{L} & K_{24} & K_{21} & -\frac{\beta EI}{L} & K_{23} & 0 \\ K_{42} & K_{44}+\frac{\beta EI}{L} & K_{41} & 0 & K_{43} & -\frac{\beta EI}{L} \\ \hline K_{12} & K_{14} & K_{11} & 0 & K_{13} & 0 \\ -\frac{\beta EI}{L} & 0 & 0 & \frac{\beta EI}{L} & 0 & 0 \\ K_{32} & K_{34} & K_{31} & 0 & K_{33} & 0 \\ 0 & -\frac{\beta EI}{L} & 0 & 0 & 0 & \frac{\beta EI}{L} \end{array}\right] \begin{Bmatrix} \alpha_i \\ \alpha_j \\ v_1 \\ \theta_1 \\ v_2 \\ \theta_2 \end{Bmatrix} \tag{3.60}$$

Eq. (3.60) is in the partitioned form of

$$\begin{Bmatrix} \boldsymbol{P}_b \\ \boldsymbol{P}_c \end{Bmatrix} = \begin{bmatrix} \boldsymbol{K}_{bb} & \boldsymbol{K}_{bc} \\ \boldsymbol{K}_{cb} & \boldsymbol{K}_{cc} \end{bmatrix} \begin{Bmatrix} \boldsymbol{\Delta}_b \\ \boldsymbol{\Delta}_c \end{Bmatrix}$$

where $\boldsymbol{\Delta}_b$ represents the internal rotational degrees of freedom to be eliminated, and $\boldsymbol{\Delta}_c$ is the preselected degrees of freedom that will remain after matrix condensation. Ultimately,

$$\boldsymbol{K'} = \boldsymbol{K}_{cc} - \boldsymbol{K}_{cb}\boldsymbol{K}_{bb}^{-1}\boldsymbol{K}_{bc} \tag{3.61}$$

The resulting flexural stiffness matrix is expressed in the following format

$$\begin{Bmatrix} V_1 \\ M_1 \\ V_2 \\ M_2 \end{Bmatrix} = \underbrace{\begin{bmatrix} K'_{11} & K'_{12} & K'_{13} & K'_{14} \\ K'_{21} & K'_{22} & K'_{23} & K'_{24} \\ K'_{31} & K'_{32} & K'_{33} & K'_{34} \\ K'_{41} & K'_{42} & K'_{43} & K'_{44} \end{bmatrix}}_{\boldsymbol{K'_C} \text{ or } \boldsymbol{K'_T}} \begin{Bmatrix} v_1 \\ \theta_1 \\ v_2 \\ \theta_2 \end{Bmatrix} \tag{3.62}$$

Member with Axial Compression

Eq. (3.63) expresses internal moment and shear along the member length:

(a) when $v_1 = 1$, $v_2 = 0$, $\theta_1 = 0$, and $\theta_2 = 0$,

$$M_{v_1}(x) = \frac{EI}{L^2}\left\{\frac{\beta\Phi^2(1+\mu)\{\cos[\varphi(L-x)] - \cos(\varphi x)\}}{[2\beta(1+\mu)+\Phi^2](1-\cos\Phi) - \beta\Phi\sin\Phi}\right\}$$

$$V_{v_1}(x) = \frac{EI}{L^3}\left\{\frac{\Phi^3[\Phi(1-\cos\Phi) - \beta\sin\Phi]}{[2\beta(1+\mu)+\Phi^2](1-\cos\Phi) - \beta\Phi\sin\Phi}\right\}$$

(b) when $v_1 = 0$, $v_2 = 0$, $\theta_1 = 1$, and $\theta_2 = 0$,

$$M_{\theta_1}(x) = \frac{EI}{L\Psi_C'}\Phi\{\beta^2\Phi\cos[\varphi(L-x)] - [\beta^2(1+\mu)+\beta\Phi^2]\sin[\varphi(L-x)] - \beta^2(1+\mu)\sin(\varphi x)\}$$

$$V_{\theta_1}(x) = -\frac{EI}{L^2}\left\{\frac{\beta\Phi^2(1-\cos\Phi)}{[2\beta(1+\mu)+\Phi^2](1-\cos\Phi) - \beta\Phi\sin\Phi}\right\} \tag{3.63}$$

(c) when $v_1 = 0$, $v_2 = 1$, $\theta_1 = 0$, and $\theta_2 = 0$,

$$M_{v_2}(x) = -M_{v_1}(x)$$

$$V_{v_2}(x) = -V_{v_1}(x)$$

(d) when $v_1 = 0$, $v_2 = 0$, $\theta_1 = 0$, and $\theta_2 = 1$,

$$M_{\theta_2}(x) = -\frac{EI}{L\Psi_C'}\Phi\{\beta^2\Phi\cos(\varphi x) - [\beta^2(1+\mu)+\beta\Phi^2]\sin(\varphi x) - \beta^2(1+\mu)\sin[\varphi(L-x)]\}$$

$$V_{\theta_2}(x) = V_{\alpha_1}(x)$$

where

$$\Psi_C' = 2[\beta^2(1+\mu)+\beta\Phi^2](1-\cos\Phi) - \Phi[\beta^2 - 2\beta(1+\mu) - \Phi^2]\sin\Phi - 2\beta\Phi^2 \tag{3.64}$$

In the stiffness matrix format,

$$K'_{C,11} = \frac{EI}{L^3}\left\{\frac{\Phi^3[\beta \sin\Phi - \Phi(1-\cos\Phi)]}{[2\beta(1+\mu)+\Phi^2](1-\cos\Phi)-\beta\Phi\sin\Phi}\right\}$$

$$K'_{C,12} = \frac{EI}{L^2}\left\{\frac{\beta\Phi^2(1-\cos\Phi)}{[2\beta(1+\mu)+\Phi^2](1-\cos\Phi)-\beta\Phi\sin\Phi}\right\}$$

$$K'_{C,21} = \frac{EI}{L^2}\left\{\frac{\beta\Phi^2(1+\mu)(1-\cos\Phi)}{[2\beta(1+\mu)+\Phi^2](1-\cos\Phi)-\beta\Phi\sin\Phi}\right\}$$

$$K'_{C,22} = \frac{EI}{L\Psi'_C}\Phi\{[\beta^2(1+\mu)+\beta\Phi^2]\sin\Phi - \beta^2\Phi\cos\Phi\} \tag{3.65}$$

$$K'_{C,24} = \frac{EI}{L\Psi'_C}\beta^2\Phi[\Phi-(1+\mu)\sin\Phi]$$

$$-K'_{C,13} = -K'_{C,31} = K'_{C,33} = K'_{C,11}$$

$$-K'_{C,32} = -K'_{C,34} = K'_{C,14} = K'_{C,12}$$

$$-K'_{C,23} = -K'_{C,43} = K'_{C,41} = K'_{C,21}$$

$$K'_{C,44} = K'_{C,22};\ K'_{C,42} = K'_{C,24}$$

Member with Axial Tension

Eq. (3.66) expresses internal moment and shear along the member length:

(a) when $v_1 = 1$, $v_2 = 0$, $\theta_1 = 0$, and $\theta_2 = 0$,

$$M_{v_1}(x) = \frac{EI}{L^2}\left\{\frac{\beta\Phi^2(1-\mu)\{\cosh[\varphi(L-x)]-\cosh(\varphi x)\}}{[-2\beta(1-\mu)+\Phi^2](1-\cosh\Phi)-\beta\Phi\sinh\Phi}\right\}$$

$$V_{v_1}(x) = \frac{EI}{L^3}\left\{\frac{\Phi^3[-\Phi(1-\cosh\Phi)+\beta\sinh\Phi]}{[-2\beta(1-\mu)+\Phi^2](1-\cosh\Phi)-\beta\Phi\sinh\Phi}\right\} \tag{3.66}$$

(b) when $v_1 = 0$, $v_2 = 0$, $\theta_1 = 1$, and $\theta_2 = 0$,

$$M_{\theta_1}(x) = \frac{EI}{L\Psi'_T}\Phi\{\beta^2\Phi\cosh[\varphi(L-x)]$$

$$-[\beta^2(1-\mu)-\beta\Phi^2]\sinh[\varphi(L-x)] - \beta^2(1-\mu)\sinh(\varphi x)\}$$

$$V_{\theta_1}(x) = -\frac{EI}{L^2}\left\{\frac{\beta\Phi^2(1-\cosh\Phi)}{[-2\beta(1-\mu)+\Phi^2](1-\cosh\Phi)-\beta\Phi\sinh\Phi}\right\}$$

(c) when $v_1 = 0$, $v_2 = 1$, $\theta_1 = 0$, and $\theta_2 = 0$,

$$M_{v_2}(x) = -M_{v_1}(x)$$

$$V_{v_2}(x) = -V_{v_1}(x)$$

(d) when $v_1 = 0$, $v_2 = 0$, $\theta_1 = 0$, and $\theta_2 = 1$,

$$M_{\theta_2}(x) = -\frac{EI}{L\Psi_T'}\Phi\{\beta^2\Phi\cosh(\varphi x) - [\beta^2(1-\mu)-\beta\Phi^2]\sinh(\varphi x)$$

$$-\beta^2(1-\mu)\sinh[\varphi(L-x)]\}$$

$$V_{\theta_2}(x) = V_{\alpha_1}(x)$$

where

$$\begin{aligned}\Psi_T' = &-2[\beta^2(1-\mu)-\beta\Phi^2](1-\cosh\Phi)\\ &-\Phi[\beta^2-2\beta(1-\mu)+\Phi^2]\sinh\Phi-2\beta\Phi^2\end{aligned} \tag{3.67}$$

In the stiffness matrix format,

$$K_{T,11}' = -\frac{EI}{L^3}\left\{\frac{\Phi^3[\beta\sinh\Phi-\Phi(1-\cosh\Phi)]}{[-2\beta(1-\mu)+\Phi^2](1-\cosh\Phi)-\beta\Phi\sinh\Phi}\right\}$$

$$K_{T,12}' = \frac{EI}{L^2}\left\{\frac{\beta\Phi^2(1-\cosh\Phi)}{[-2\beta(1-\mu)+\Phi^2](1-\cosh\Phi)-\beta\Phi\sinh\Phi}\right\}$$

$$K_{T,21}' = \frac{EI}{L^2}\left\{\frac{\beta\Phi^2(1-\mu)(1-\cosh\Phi)}{[-2\beta(1-\mu)+\Phi^2](1-\cosh\Phi)-\beta\Phi\sinh\Phi}\right\} \tag{3.68}$$

$$K_{T,22}' = \frac{EI}{L\Psi_T'}\Phi\{[\beta^2(1-\mu)-\beta\Phi^2]\sinh\Phi-\beta^2\Phi\cosh\Phi\}$$

$$K_{T,24}' = \frac{EI}{L\Psi_T'}\beta^2\Phi[\Phi-(1-\mu)\sinh\Phi]$$

$$-K_{T,13}' = -K_{T,31}' = K_{T,33}' = K_{T,11}'$$

$$-K'_{T,32} = -K'_{T,34} = K'_{T,14} = K'_{T,12}$$

$$-K'_{T,23} = -K'_{T,43} = K'_{T,41} = K'_{T,21}$$

$$K'_{T,44} = K'_{T,22};\ K'_{T,42} = K'_{T,24}$$

3.2.3 Comparisons

Flexural stiffness expressions derived with respect to the Timoshenko elastic beam theory are similar in structure to those derived based on the Euler elastic beam theory. The only difference is the inclusion of variable μ [see Eq. (3.38)] in the Timoshenko expressions for beam-columns. As GA_S approaches infinity (i.e., the member has infinite shear rigidity), μ becomes zero, and the Timoshenko expressions converge to the Euler expressions.

The [1,1] term in each flexural stiffness matrix represents the theoretical lateral stiffness of the member under consideration. Given geometric properties of the test specimens and their applied axial load magnitudes, the theoretical Euler and Timoshenko lateral stiffnesses, assuming ideal boundary conditions, can be calculated according to Sections 3.2.1.2 and 3.2.2.2, respectively; these are $\overline{K}_{C,11}$ and $K_{C,11}$, respectively. Ignoring the effect of axial loads, the corresponding Euler and Timoshenko lateral stiffnesses can also be determined according to Sections 3.2.1.1 and 3.2.2.1, respectively; these are $\overline{K}_{11}$ and K_{11}, respectively. Results are shown in Table 3.1. Since all specimens in Phase 2 test program were subjected to strong-axis bending, the effect of axial compression on stiffness reduction is insignificant; $\overline{K}_{11}$ and $\overline{K}_{C,11}$ are similar in magnitude, which is also true for K_{11} and $K_{C,11}$. However, the effect of shear deformation on lateral stiffness is significant as demonstrated by the percent difference between $\overline{K}_{C,11}$ and $K_{C,11}$; these values carry the

Euler and Timoshenko beam assumptions, respectively. Indeed, the Euler beam theory ignores shear deformation and, as a result, overestimates the member lateral stiffness.

In addition, the two theoretical quantities ($\overline{K}_{C,11}$ and $K_{C,11}$) are also compared with the measured lateral stiffnesses (K_{me}) of each test specimen. Indeed, Timoshenko beam theory, which considers shear deformation, can predict stiffness values closer to the measured values; the difference between the theoretical lateral stiffness $K_{C,11}$, assuming ideal boundary conditions, and the measured lateral stiffness K_{me} results from flexibility of the member end connections, which is unavoidable in testing. Due to this reason, behavior of Timoshenko beam-columns with flexible end restraints is studied in Section 3.2.2.3. By idealizing the member end connection flexibility as a rotational spring, the derived lateral stiffness relationship from Section 3.2.2.3 can be used to calibrated with the test data (i.e., the lateral force vs. measured drift response) to determine the *equivalent* end rotational spring stiffness $\beta(EI/L)$, which represents and quantifies connection flexibility. The calibrated β values are also reported in Table 3.1. Ultimately, after considering both the effects of axial load and end connection flexibility, theoretical Timoshenko flexural stiffnesses corelate well with test data in elastic range. Finite element analysis results are also consistent with this conclusion (results not shown). Consequently, Timoshenko beam-column equations are used in the data reduction process discussed in Section 3.3.

3.3 Drift Correction Procedure

Ideal rigid boundary conditions were difficult to achieve in this testing program as some relative rotations between the specimen ends and the reaction fixtures were observed despite the use of fully-restrained connections. Furthermore, moment-rotation characteristics of these fully-restrained connections varied for each specimen. To make

meaningful comparisons between the specimen responses, it is necessary to correct the test data to eliminate the effect of end connection flexibility. The theoretical study of elastic beam-column behavior corresponding to rigid- and flexible-end boundary conditions, utilizing the Timoshenko theory, is discussed in Sections 3.2.2.2 and 3.2.2.3, respectively; theoretical expressions that considered both shear deformation and the second-order effects were derived. All test results were corrected according to the theoretical study to represent ideal (or rigid) boundary conditions; the procedure is summarized in this section.

Figure 2.2(b) shows bolted end connections of typical specimens. Despite that 1½-in. diameter high-strength bolts were used to fasten the end plates to fixed fixtures, unintended end rotations were unavoidable due to the out-of-plane flexibility of the end plates and elongation of the bolts. These end rotations due to connection flexibility caused rigid-body rotation of the specimens. Accordingly, the *measured* (or imposed) lateral drift at the moving end of the specimens, Δ_m, can be expressed as:

$$\Delta_m = \Delta_{me} + \Delta_{mc} + \Delta_{mp} \tag{3.69}$$

where Δ_{me} and Δ_{mp} represent the elastic and plastic components of the measured lateral drift due to column straining, respectively, and Δ_{mc} is the drift resulting from rigid-body rotation of the column due to connection flexibility. Removing Δ_{mc} from Δ_m gives the corrected story drift corresponding to ideal boundary conditions. Since it is difficult to measure Δ_{mc} experimentally, this component was removed using the following procedure.

Assuming that Δ_{mc} remains elastic, Δ_{me}+Δ_{mc} collectively represents the elastic component of Δ_m. Accordingly, the plastic component of Δ_m can be extracted as follows:

$$\Delta_{mp} = \Delta_m - \frac{V}{K_{me}} \tag{3.70}$$

where V is the measured column shear (i.e., lateral force), and K_{me} is the measured elastic stiffness (i.e., the initial slope of the Δ_m versus V response). Corrected lateral drift due to the column deformation only is then the sum of the theoretical elastic drift, Δ_e, and the experimentally determined Δ_{mp}:

$$\Delta = \Delta_e + \Delta_{mp} \tag{3.71}$$

where

$$\Delta_e = \frac{V}{K_e} \tag{3.72}$$

K_e is the best estimate of the elastic lateral stiffness and is represented by the theoretical lateral stiffness of a Timoshenko beam-column with ideal boundary conditions, considering both the second-order effect and the shear deformation effect. Calculation of K_e is discussed in the following sections for fixed-fixed boundary condition case, fixed-rotating boundary condition case, and varying-axial load case. Eq. (3.71) can be re-written as follows:

$$\Delta = \Delta_e + \Delta_{mp} = \frac{V}{K_e} + \left(\Delta_m - \frac{V}{K_{me}}\right) \tag{3.73}$$

Then, the corrected story drift angle (*SDA*) is defined as the corrected drift, Δ, divided by the column clear length, L (i.e., excluding end plate thicknesses).

$$SDA = \frac{\Delta}{L} \tag{3.74}$$

3.3.1 Specimens with Fixed-fixed Boundary Conditions and Constant Axial Compression

Lateral Drift and End Moment Calculation

The lateral movement measured at the center of the SRMD platen, Δ_T, reflects the exact lateral drift at the moving (or east) end of the column; see Figure 3.7(a). Thus,

$$\Delta_m = \Delta_T \tag{3.75}$$

This drift includes the effect of rigid-body rotation due to connection flexibility. In testing, the connection rotations were practically the same in magnitude and direction at both column ends due to symmetry of the test setup; this allowed the inflection point to be assumed to still remain at the midspan [see Figure 3.8(a)]. With this assumption, east and west end moments including *P*-Δ effect are computed as follows:

$$M_W = M_E = \frac{1}{2}[V(L - \Delta_s) + P\Delta_m] \tag{3.76}$$

where $\Delta_s =$ axial shortening, and $P =$ applied axial load (see Figure 3.9 for sign conventions). The calculated end moment can be normalized by either the plastic moment, M_p, or the reduced plastic moment, M_{pc}, of the section (ASCE-WRC 1971):

For $P/P_y \geq 0.15$,

$$M_{pc} = 1.18\left(1 - \frac{P}{P_y}\right)M_p \tag{3.77a}$$

For $P/P_y < 0.15$,

$$M_{pc} = M_p \tag{3.77b}$$

The measured yield stresses from tensile coupon testing (see Table 2.2) are used to compute P_y and M_p.

Corrected Lateral Drift

Eq. (3.78) expresses the theoretical elastic shear-drift relationship of a beam-column with ideal fixed-fixed boundary conditions with the inflection point at the midspan.

$$V = K_{C,11}\Delta \tag{3.78}$$

Thus, K_e based on the Timoshenko theory considering both shearing and second-order effects (compression case) is

$$K_e = K_{C,11} = \frac{EI}{L^3\Psi_C}\Phi^3 \sin\Phi \tag{3.79}$$

which is used in Eq. (3.73) to compute the corrected drift. The dimensionless factors are defined as

$$\Phi = \varphi L = \sqrt{\frac{P}{EI}}L \tag{3.80}$$

$$\mu = \frac{P}{GA_s} \tag{3.81}$$

$$\Psi_C = 2(1+\mu)(1-\cos\Phi) - \Phi\sin\Phi \tag{3.82}$$

where $P =$ axial force magnitude (i.e., absolute value), $E =$ elastic modulus, $I =$ moment of inertia about the bending axis, and $G =$ shear modulus. A_s is the effective shear area, accounting for the fact that shear stress and shear strain are not uniformly distributed over the cross section (Cowper 1966); it also varies based on bending direction. Therefore, calculation of A_s is discussed below for strong- and weak-axis bending cases, respectively.

For a wide-flange member bent about its strong axis, shear stress distribution concentrates mostly in the web. Defining

$$A_s = kA \tag{3.83}$$

where A is the member's cross-sectional area, Cowper (1966) provides an extensive expression for the Timoshenko shear coefficient:

$$k = \frac{10(1+\nu)(1+3m)^2}{(12+72m+150m^2+90m^3)+\nu(11+66m+135m^2+90m^3)+30n^2(m+m^2)+5\nu n^2(8m+9m^2)} \quad (3.84)$$

where Poisson's ratio $\nu = 0.3$ for steel, $m = \frac{2b_f t_f}{h_0 t_w}$, $h_0 =$ distance between the flange centroids, and $n = \frac{b_f}{h_0}$. Alternatively, A_s can be reasonably estimated as the web area, i.e., $(d - 2t_f)t_w$, of the section as shown in Figure 3.10.

For a wide-flange member bent about its weak axis, shear stress distribution concentrates mostly in the flanges. Neglecting the web contribution in resisting shear, the effective shear area becomes

$$A_s = kA_f \quad (3.85)$$

where A_f is the total flange area ($= 2b_f t_f$), and k associated with the shear stress distribution in a rectangular cross section (i.e., the flanges) is (Cowper 1966)

$$k = \frac{10(1+\nu)}{12+11\nu} \quad (3.86)$$

An example correction of the column shear-drift response of Specimen 13M subjected to strong-axis bending is shown in Figure 3.11. Note that the calculated values of K_{me} and K_e are 177.18 and 231.26 kips/in., respectively; the measured lateral stiffness was reduced by 23% due to flexibility of the end connections.

By idealizing the connection flexibility at both column ends as end rotational springs with an equivalent spring stiffness of

$$K_\theta = \beta\left(\frac{EI}{L}\right) \quad (3.87)$$

Eq. (3.88) was calibrated with the elastic portion of shear-drift test responses to determine β and K_θ

$$V = K'_{C,11}\Delta_m \tag{3.88}$$

where

$$K'_{C,11} = \frac{EI}{L^3}\left\{\frac{\Phi^3[\beta \sin\Phi - \Phi(1-\cos\Phi)]}{[2\beta(1+\mu)+\Phi^2](1-\cos\Phi)-\beta\Phi\sin\Phi}\right\} \tag{3.89}$$

The results are listed in Table 3.1. Note that a connection can be considered "fully restrained" for β greater than 20 (Commentary of AISC 2016c).

3.3.2 Specimens with Fixed-rotating Boundary Conditions and Constant Axial Compression

Lateral Drift and End Moment Calculation

For fixed-rotating boundary condition tests conducted in Phase 2 program, cyclic end rotations in-phase with and proportional to cyclic lateral drifts were prescribed to the east or moving end; thus, the east end rotation can be expressed as follows:

$$\theta_m = \xi_m\left(\frac{\Delta_m}{L}\right) \tag{3.90}$$

where ξ_m is the rotation-to-drift ratio and is set equal to 1 for Specimens 13M-BC and 16M-BC and 1.1 for Specimen 11H-BC.

Forces, moments, displacements, and rotations applied to the specimens in all three primary directions of interest were recorded at the center of the SRMD platen [see Figure 3.7(b)]. The column east end was connected to the SRMD platen a distance L_T away from this reference point. Because of this setup, prescribing θ_m to the SRMD platen for it to rotate about its center, which simulated the east end rotation, resulted in a displacement of the column east end. To maintain a consistent loading protocol, this displacement was

accounted for in the lateral-drift loading protocol prescribed to the platen. Accordingly, the lateral drift at the column moving end can be obtained from the following relationship.

$$\Delta_m = \Delta_T - \theta_m L_T \tag{3.91}$$

Given Δ_m and θ_m, lateral movements of the platen, Δ_T, can be determined from Eq. (3.91).

Figure 3.8 compares deformed configurations of a column with ideal fixed-fixed boundary conditions and a column with ideal fixed-rotating boundary conditions. The inflection point of the fixed-rotating column locates closer to the rotating end, depending on the magnitude of the end rotation in proportion to the applied lateral drift (i.e., ξ_m). Due to the unsymmetrical nature of the fixed-rotating boundary condition tests, the inflection point location also moves once the column exhibits inelastic behavior. Therefore, the approach described in Section 3.3.1 cannot be used to determine end moments. Instead, utilizing the recorded strong-axis moment applied by the SRMD platen, M_T, a moment equilibrium can be applied to the entire system so that the moment at the column west end can be calculated; Figure 3.7(b) demonstrates this free body diagram. Thus, west end moment becomes

$$M_W = V(L + L_T - \Delta_s) + P\Delta_T - M_T \tag{3.92}$$

Enforcing moment equilibrium in the column, the following equation calculates east end moment:

$$M_E = V(L - \Delta_s) + P\Delta_m - M_W \tag{3.93a}$$

or

$$M_E = M_T - P\theta_m L_T - VL_T \tag{3.93b}$$

The accuracy of the calculated moment was confirmed by comparing it with that computed from the strain gauge data when the column responded in the elastic range (results not shown).

Corrected Lateral Drift

Because the west and east end moments were not the same in magnitude like those observed in the fixed-fixed boundary condition case, connection rotation at each column end also differed in magnitude. Consequently, in addition to the applied end rotation at the moving end, connection flexibility also influenced the location of inflection point in the specimens. The following steps determine K_e for fixed-rotating specimens, which is used in Eq. (3.73) to remove the effect of connection flexibility from the lateral drift responses: (1) determine the equivalent end rotational spring stiffness and locate the inflection point in the specimens, (2) based on the determined inflection point location, calculate an equivalent moving-end rotation assuming both column-end connections are rigid, and (3) calculate K_e based on the equivalent moving-end rotation determined in (2). The theoretical expressions provided by Chansuk et al. (2018) were utilized in this calculation.

Step 1: Determine the equivalent end rotational spring stiffness and inflection point location

By idealizing the connection flexibility at both ends of the specimens as end rotational springs with an identical equivalent stiffness of $\beta(EI/L)$, Eq. (3.94) expresses the theoretical elastic lateral stiffness relationship of a fixed-rotating beam-column with flexible end restraints:

$$V = \left(K'_{C,11} - \frac{\xi_m}{L} K'_{C,12}\right) \Delta_m \tag{3.94}$$

where $K'_{C,11}$ is per Eq. (3.89) and

$$K'_{C,12} = \frac{EI}{L^2}\left\{\frac{\beta\Phi^2(1-\cos\Phi)}{[2\beta(1+\mu)+\Phi^2](1-\cos\Phi)-\beta\Phi\sin\Phi}\right\} \tag{3.95}$$

Eq. (3.94) is calibrated with the measured shear-drift elastic response to back-calculate β. Once β is determined, internal moment along the member can be expressed using the superposition principle:

$$M'(x) = \left[M'_{v_1}(x) - \frac{\xi_m}{L}M'_{\theta_1}(x)\right]\Delta_m \tag{3.96}$$

where

$$M'_{v_1}(x) = \frac{EI}{L^2}\left\{\frac{\beta\Phi^2(1+\mu)\{\cos[\varphi(L-x)]-\cos(\varphi x)\}}{[2\beta(1+\mu)+\Phi^2](1-\cos\Phi)-\beta\Phi\sin\Phi}\right\} \tag{3.97}$$

$$M'_{\theta_1}(x) = \frac{EI}{L\Psi'_C}\Phi\{\beta^2\Phi\cos[\varphi(L-x)] - [\beta^2(1+\mu)+\beta\Phi^2]\sin[\varphi(L-x)] - \beta^2(1+\mu)\sin(\varphi x)\} \tag{3.98}$$

The dimensionless factor Ψ'_C is defined as

$$\Psi'_C = 2[\beta^2(1+\mu)+\beta\Phi^2](1-\cos\Phi) - \Phi[\beta^2 - 2\beta(1+\mu) - \Phi^2]\sin\Phi - 2\beta\Phi^2 \tag{3.99}$$

Physically, $M'_{v_1}(x)$ and $M'_{\theta_1}(x)$ represent the moment distribution along the member length due to a unit lateral displacement and a unit rotation, respectively, at the moving end; where x is measured from the moving end. Setting Eq. (3.96) to zero and solving for x give the inflection point location, x_{IP}, in the specimen.

Step 2: Determine an equivalent moving-end rotation

To eliminate the effect of rigid-body rotation caused by connection flexibility that contributed to the measured lateral drift, the specimen is assumed to have ideal fixed-rotating boundary conditions, i.e., rigid end connections, and sustain an equivalent moving-end rotation of

$$\theta = \xi\left(\frac{\Delta}{L}\right) \tag{3.100}$$

Essentially, if the specimen sustained θ and Δ at the moving end with ideal boundary conditions, it would have the same inflection point location as if it sustained θ_m and Δ_{m} with flexible end connections, i.e., both the ideal and real configurations are equivalent. θ is determined as follows.

Eq. (3.101) expresses the theoretical internal moment along a beam-column with ideal fixed-rotating boundary conditions:

$$M(x) = \left[M_{v_1}(x) - \frac{\xi}{L}M_{\alpha_1}(x)\right]\Delta \tag{3.101}$$

where

$$M_{v_1}(x) = \frac{EI}{L^2\Psi_C}\Phi^2(1+\mu)\{\cos[\varphi(L-x)] - \cos(\varphi x)\} \tag{3.102}$$

$$M_{\alpha_1}(x) = \frac{EI}{L\Psi_C}\Phi\{\Phi\cos[\varphi(L-x)] - (1+\mu)\sin[\varphi(L-x)] - (1+\mu)\sin(\varphi x)\} \tag{3.103}$$

Substituting x_{IP} determined in Step 1 into Eq. (3.101) gives

$$M(x_{IP}) = \left[M_{v_1}(x_{IP}) - \frac{\xi}{L}M_{\alpha_1}(x_{IP})\right]\Delta \tag{3.104}$$

Accordingly, ξ can be calibrated such that $M(x_{IP}) = 0$ to make the inflection point location of the ideal configuration identical to that of the actual configuration. θ is then calculated per Eq. (3.100).

Step 3: Calculate K_e

Eq. (3.105) expresses the theoretical elastic shear-drift relationship of the specimen with the equivalent ideal fixed-rotating boundary conditions.

$$V = \left(K_{C,11} - \frac{\xi}{L}K_{C,12}\right)\Delta \tag{3.105}$$

Thus, K_e based on the Timoshenko theory considering both shearing and second-order effects (compression case) becomes

$$K_e = K_{C,11} - \frac{\xi}{L} K_{C,12} \tag{3.106}$$

where $K_{C,11}$ is calculated as in Eq. (3.79) and

$$K_{C,12} = \frac{EI}{L^2 \Psi_C} \Phi^2 (1 - \cos \Phi) \tag{3.107}$$

The calculated K_e is then used in Eq. (3.73) to compute the corrected drift. An example correction of the shear-drift response of Specimen 13M-BC is shown in Figure 3.12. Note that the calculated values of K_{me} and K_e are 88.45 and 106.31 kips/in., respectively. Table 3.2 summarizes key variables associated with this drift correction procedure for each fixed-rotating specimen.

3.3.3 Specimens with Fixed-fixed Boundary Conditions and Varying Axial Load Sequences

Lateral Drift and End Moment Calculation

This process is the same as that described in Section 3.3.1 since the specimens sustain fixed-fixed boundary conditions.

Corrected Lateral Drift

Because the applied axial load varies during testing, the member elastic flexural stiffness varies accordingly due to the beam-column effect. In strong-axis bending, this effect is insignificant because the strong-axis moment of inertia is relatively high. Nonetheless, to capture this phenomenon and establish a standard procedure for future uses, the theoretical lateral stiffness relationship of a beam-column with flexible end restrains as in Eq. (3.108) is calibrated with the column shear-drift test response in the elastic range to determine the equivalent end rotational spring stiffness $\beta(EI/L)$.

$$V = (K'_{C,11} \text{ or } K'_{T,11})\,\Delta_m \tag{3.108}$$

where $K'_{C,11}$ is expressed as in Eq. (3.89) for when the axial force is in compression and

$$K'_{T,11} = -\frac{EI}{L^3}\left\{\frac{\Phi^3[\beta \sinh\Phi - \Phi(1-\cosh\Phi)]}{[-2\beta(1-\mu)+\Phi^2](1-\cosh\Phi)-\beta\Phi\sinh\Phi}\right\} \tag{3.109}$$

for when the axial force is in tension. In computing Φ, P is always positive. Using the determined β, K_{me} is estimated as either $K'_{C,11}$ or $K'_{T,11}$ per Eq. (3.89) and (3.109), respectively, for each loading step in the response history: it varies based on each corresponding axial load magnitude and direction.

Eq. (3.110) expresses the theoretical elastic shear-drift relationship of a beam-column with ideal fixed-fixed boundary conditions subjected to varying axial loads.

$$V = (K_{C,11} \text{ or } K_{T,11})\,\Delta \tag{3.110}$$

Thus, K_e for axial compression case is estimated as $K_{C,11}$ per Eq. (3.79). For axial tension case,

$$K_e = K_{T,11} = -\frac{EI}{L^3\Psi_T}\Phi^3\sinh\Phi \tag{3.111}$$

where

$$\Psi_T = -2(1-\mu)(1-\cosh\Phi) - \Phi\sinh\Phi \tag{3.112}$$

Similarly, K_e is calculated for each loading step in the response history based on each respective axial load magnitude and direction. Ultimately, the corrected drift is determined using Eq. (3.73) based on the calculated varying K_{me} and K_e.

Chapter 2, 3, 4, and 5 in part are currently being prepared for submission for publication of the material. Chansuk, P., Ozkula, G., and Uang, C.-M. (2018). “ATC-106 Phase 2: Seismic behavior and design of deep, slender wide-flange structural steel beam-

columns." *Report No. SSRP-18/02*, University of California, San Diego, La Jolla, CA. The thesis author was the primary investigator and author of this material.

Table 3.1 Lateral Stiffness Comparisons: Fixed-fixed Boundary Condition Tests

Specimen	Section	μ	$\bar{K}_{11}$	$\bar{K}_{C,11}$	K_{11}	$K_{C,11}$	K_{me}	β	K_θ	Difference[a]
		[×10^{-3}]	[kips/in.]		[kips/in.]		[kips/in.]	[-]	[×10^6 kips/in.]	[%]
11M	W24×176	4.84	213.44	208.17	172.76	168.63	131.94	17.88	14.02	23.5
12LM	W30×261	3.47	492.26	485.70	365.37	360.71	243.79	9.61	17.38	34.7
12LM-P	W30×261	3.47	492.26	486.36	365.37	361.18	236.60	12.52	22.65	34.7
13M	W30×173	4.44	309.26	304.03	235.08	231.26	177.18	15.45	17.56	31.5
14L	W30×90	1.60	131.85	130.51	110.90	109.80	96.65	37.29	18.41	18.9
15L	W18×192	2.72	141.35	138.49	121.70	119.29	97.09	21.70	11.49	16.1
16M	W18×130	5.36	89.85	85.97	78.18	74.88	63.91	31.66	10.65	14.8
17L	W18×76	2.49	48.58	47.46	42.98	42.01	39.24	76.88	13.99	13.0
21M-NF	W18x130	4.84	89.85	85.96	78.18	74.87	67.59	25.67	8.71	14.8
22L	W30×148	1.86	230.67	228.51	186.22	184.53	143.67	17.28	15.50	23.8
23L	W18×60	1.98	72.22	71.11	62.53	61.59	55.84	50.80	8.63	15.5
24L	W14×82	2.96	64.66	63.14	56.18	54.89	46.90	31.34	4.77	15.0
25L	W14×53	2.60	39.71	38.72	35.25	34.39	32.06	74.63	6.97	12.6
26L	W14×132	5.85	112.29	108.57	92.65	89.67	76.71	30.24	7.99	21.1
27L	W24×84	1.84	81.84	80.62	71.26	70.22	61.03	35.20	11.20	14.8

[a] Difference $= \left(\bar{K}_{C,11} - K_{C,11}\right)/K_{C,11}$.

Table 3.2 Fixed-rotating Boundary Condition Tests: Data Reduction Related Parameters

Specimen	Section	L_T	ξ_m	P[a]	μ	β	K_θ	x_{IP}	ξ	K_e	K_{me}	Stiffness Reduction[b]
		[in.]	[-]	[kips]	[$\times 10^{-3}$]	[-]	[$\times 10^6$ kips/in.]	[in.]	[-]	[kips/in.]		[%]
11H-BC	W24×176	28	1.12	1393	7.32	21.20	16.62	43.9	1.18	64.92	55.70	14.2
13M-BC	W30×173	28	1.00	914	4.44	16.54	18.80	53.1	1.07	106.31	88.45	16.8
16M-BC	W18×130	27	1.00	688	5.39	30.80	10.36	61.8	1.05	34.16	30.38	11.1

[a] Mean measured axial load (positive for compression).

[b] Member lateral stiffness reduction due to the effect of connection flexibility estimated as $(K_e - K_{me})/K_e$.

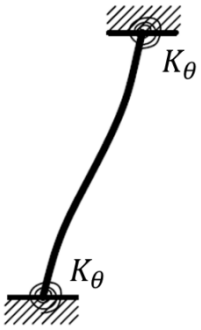

(a) Ideal or Rigid Boundary Conditions

(b) Flexible or Partially Restrained Boundary Conditions

Figure 3.1 Fixed-fixed Beam-columns

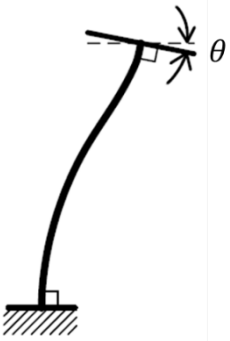

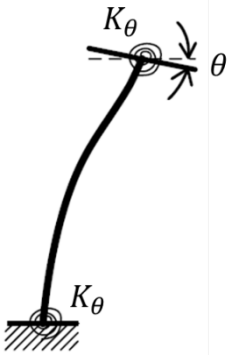

(c) Ideal or Rigid Boundary Conditions

(d) Flexible or Partially Restrained Boundary Conditions

Figure 3.2 Fixed-rotating Beam-columns

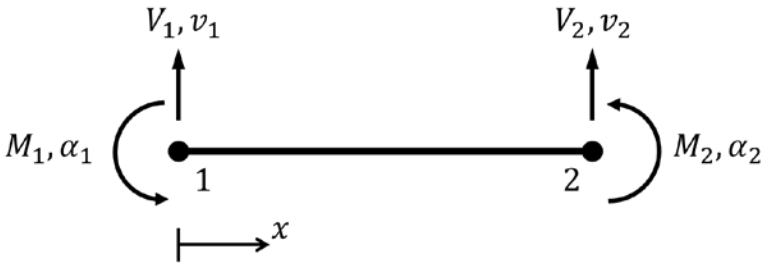

Figure 3.3 Two-node Member with Four Degrees of Freedom

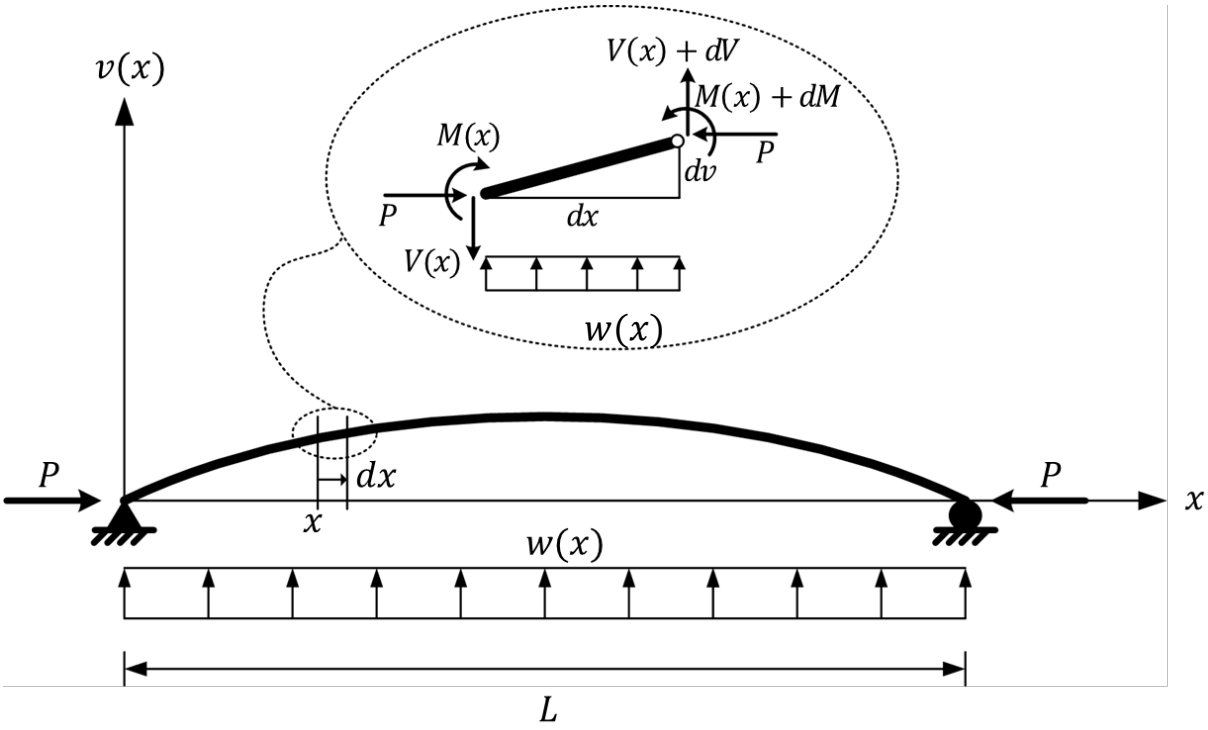

Figure 3.4 Equilibriums of an Axially Loaded Beam in its Deformed Configuration

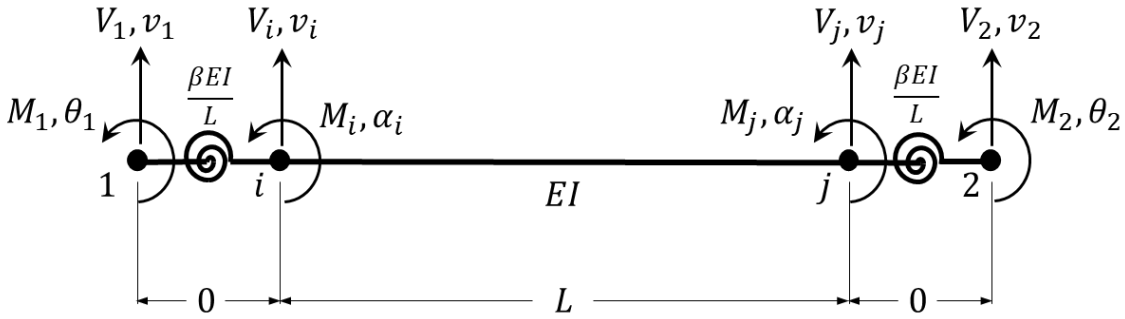

Figure 3.5 Four-node Member with End Rotational Springs

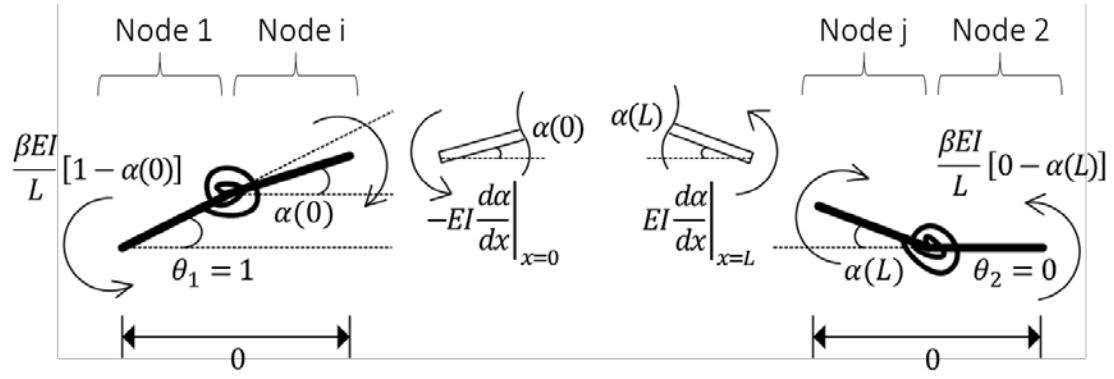

Figure 3.6 Rotational Spring Moment and Member Internal Moment Relationship

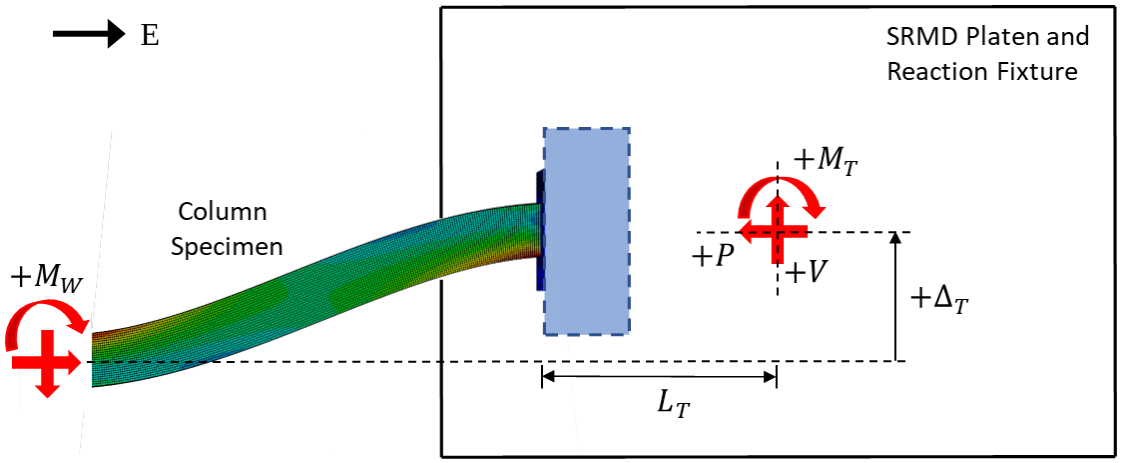

(a) Fixed-fixed Boundary Condition

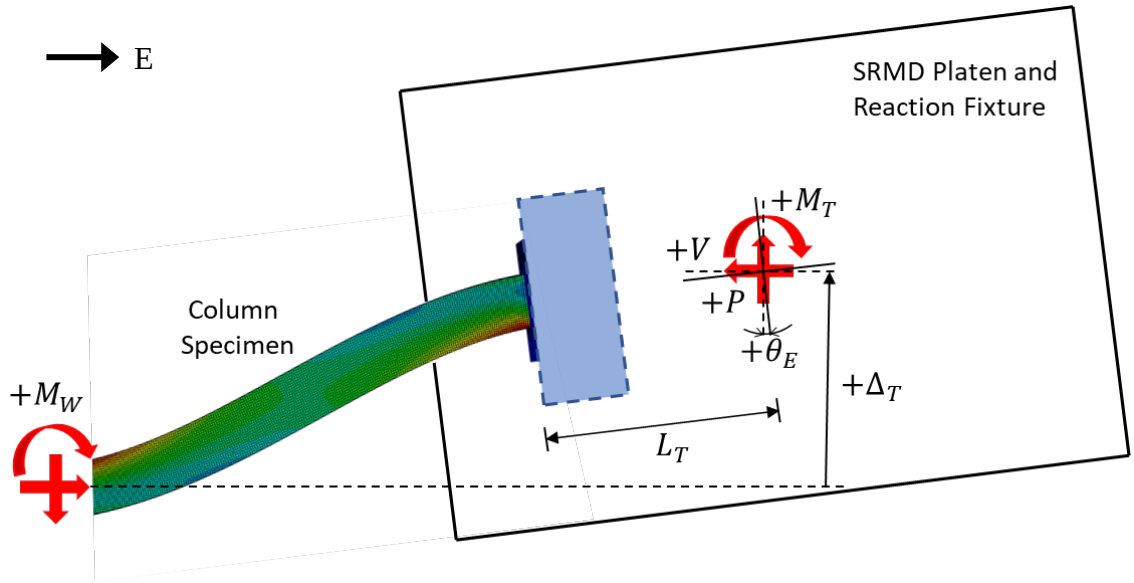

(b) Fixed-rotating Boundary Condition

Figure 3.7 Platen Free Body Diagram

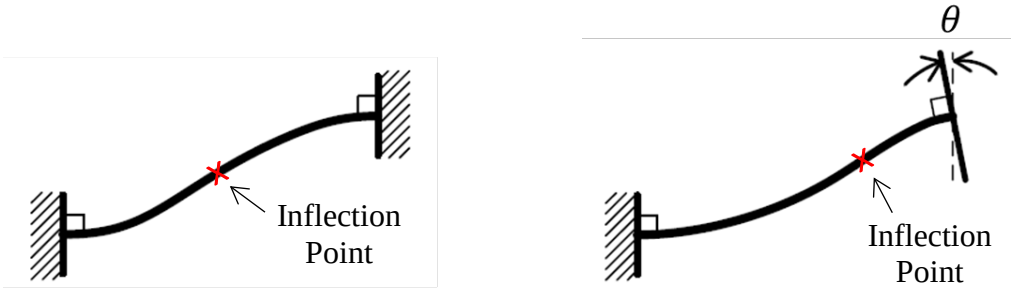

(a) Fixed-fixed Boundary Condition (b) Fixed-rotating Boundary Condition

Figure 3.8 Boundary Condition Effect

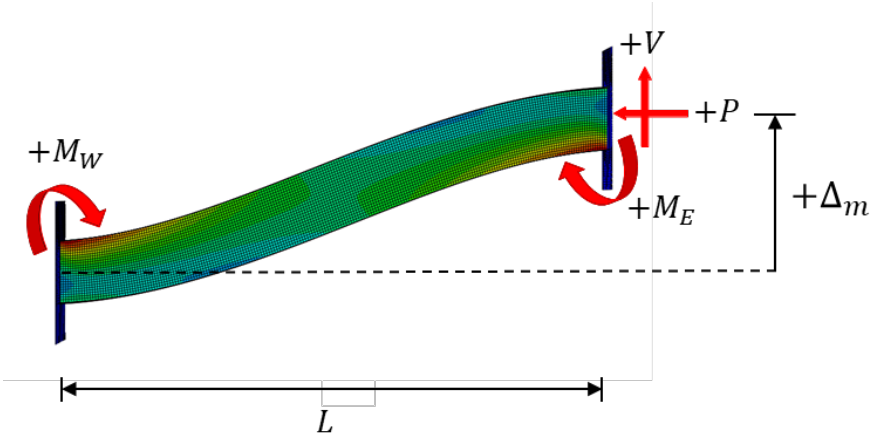

Figure 3.9 Sign Convention

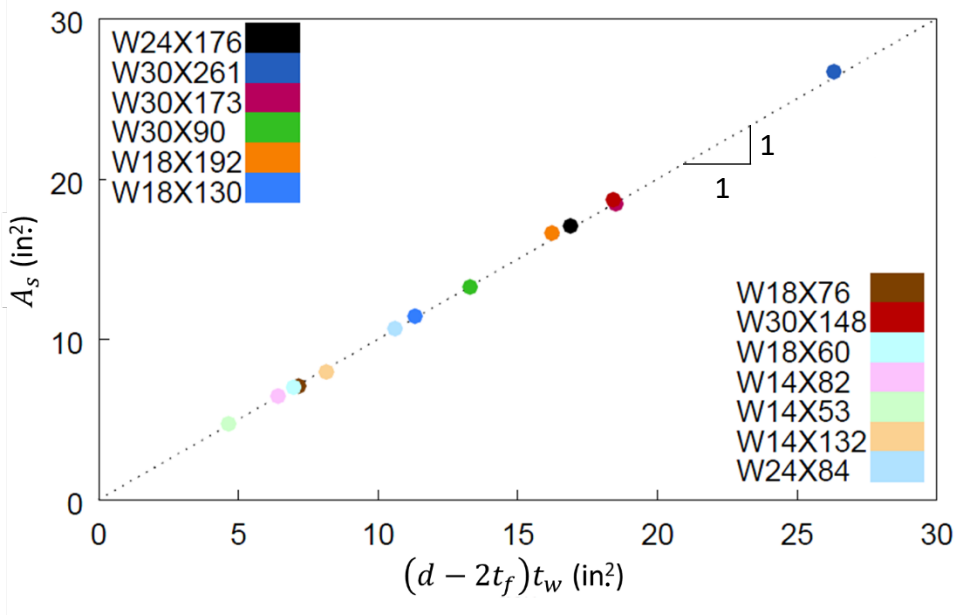

Figure 3.10 Web Area vs. Shear Area per Eq. (3.22)

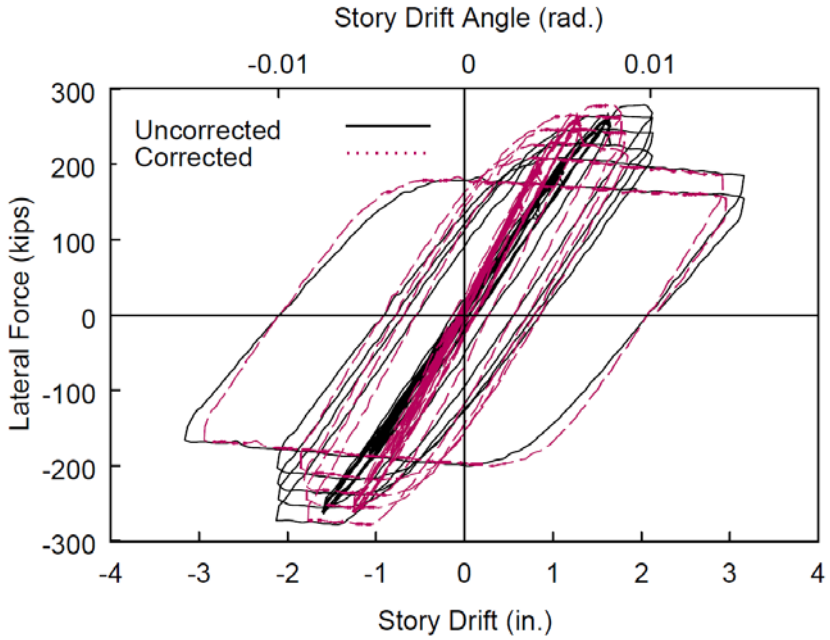

Figure 3.11 Corrected versus Uncorrected Hysteresis Response of Specimen 13M

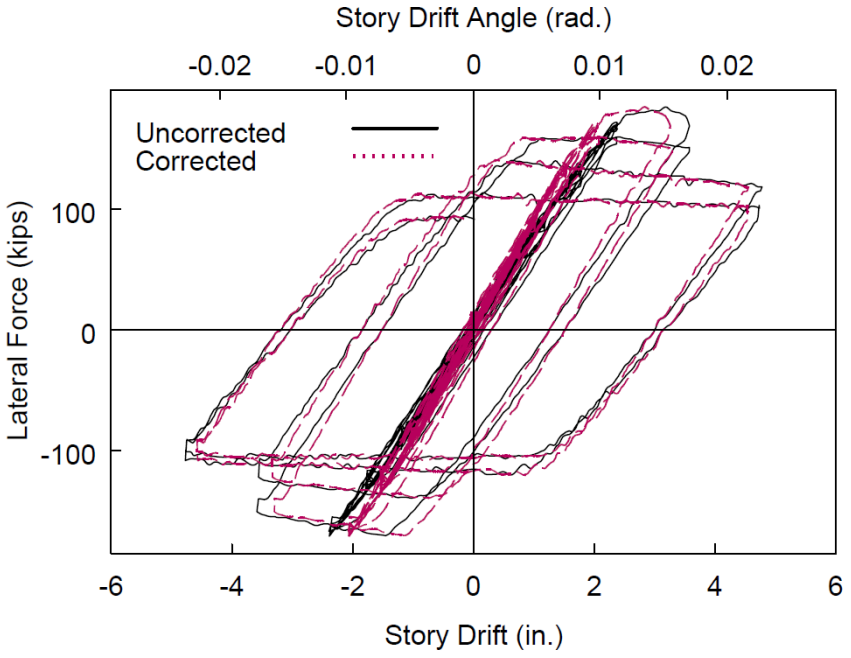

Figure 3.12 Corrected versus Uncorrected Hysteresis Response of Specimen 13M-BC

4. TEST RESULTS

4.1 Introduction

With respect to the scope of this thesis, measured responses and observed behavior of certain specimens from NIST Phase 2 testing are presented in this chapter. Figures are included to illustrate the progression of yielding, buckling, and the overall deformed configuration of each specimen as the magnitudes of the story drift angle (*SDA*) increased. Global responses of the specimens are presented in the form of lateral force (i.e., column shear), end moment, and axial shortening versus story drift plots. An out-of-plane (OOP) displacement at the column midspan is also reported for some specimens. For simplicity, story drift angle in radian is also referred to as percent drift (e.g., 0.01 rad *SDA* corresponds to 1% drift). As discussed in Section 2.5, the AISC loading protocol applied 6, 6, 6, 4, and 2 cycles at 0.375%, 0.5%, 0.75%, 1%, and 1.5% drift and greater to the specimens, respectively.

Since all specimens bended in reverse curvature in strong-axis due to the applied lateral drift and boundary conditions, the column flanges diagonal to each other at member ends experienced the same in-plane bending effect (either tension or compression). With respect to the test setup as shown in Figure 4.1, the northwest and southeast flanges were under flexural compression in the positive drift, and the same for the southwest and northeast flanges in negative drift. The terms “flange(s) under compression” or “compression flange(s)” and “flange(s) under tension” or “tension flange(s)” are used in this chapter for briefness to describe this in-plane flexural effect in the specimens due to the applied cyclic story drift. To further facilitate column behavior explanation, positive and negative excursions referred to when a specimen was displaced in the positive and

negative directions, respectively. In addition, failure mode classifications and certain phenomena defined in Section 2.8 are referenced here to help explain column behavior during testing.

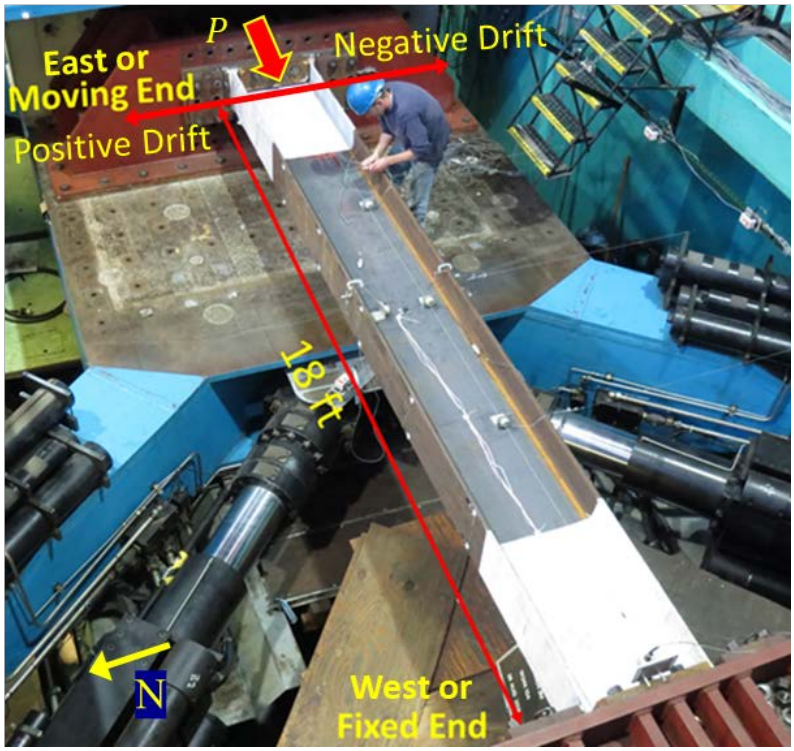

Figure 4.1 Test Setup and Specimen Orientation

4.2 Group 11 Specimens: Section W24×176

4.2.1 General

Group 11 comprised three W24×176 columns labeled as Specimens 11M, 11H-VA, and 11H-BC. The shape was identical to that of Group 1 specimens in Phase 1 testing, which experienced the CB failure mode. Specimen 11M was subjected to constant axial compression with $C_a = 0.4$ and served as a re-test of Specimen 1M in Phase 1 testing to confirm that the same CB mode could be reproduced. Specimen 11H-VA underwent varying axial compression ($C_a = 0.3$ to 0.6) to simulate an exterior column response. Both

Specimens 11M and 11H-VA were tested with fixed-fixed boundary conditions. Specimen 11H-BC was subjected to constant axial compression with $C_a = 0.6$ and the end rotation sequence (see Section 2.6) to simulate rotation at the top end of first-story columns in real application.

4.2.2 Specimen 11M

The governing failure mode of Specimen 11M is CB with the single-curvature global configuration. Yielding as well as local and global buckling progression is illustrated in Figure 4.2 and Figure 4.3. At 1% drift, the sloped flaking pattern initiated. At 1.5% drift, minor LTB movements initiated at the west end. In addition, web and flange local buckles with minor amplitudes were observed at both ends. Thus, the sequence of local and global instabilities was not obvious for this specimen; both appeared to initiate at 1.5% drift. LTB of the specimen aggravated at 2% and 3% drifts: during the positive excursion of each drift cycle, the positive-drift compression flanges buckled out of plane more, and the same happened for the negative-drift compression flanges during the negative excursion. As a result, the specimen experienced significant twisting and downward movement with higher out-of-plane amplitude observed toward the west end. LTB-type movement was limited at the east end; instead, it appeared to exhibit the ALB configuration. Indeed, yielding seemed more uniform and localized at the east end during 2% and 3% drifts compared to that at the west end. Nonetheless, LTB-induced flange local buckling at the bottom half-width flanges at both ends as shown with arrows in Figure 4.3 for *SDA* = 0.03 rad exacerbated corresponding to the drastic downward movement of the column. The excessive out-of-plane displacement prompted the termination of testing. During the attempt to unload the specimen after the test was terminated, the northeast flange ruptured near the end plate

across the entire flange width as shown in Figure 4.4. The rupture appeared to initiate from the column web weld access hole. Figure 4.5 shows local buckling configurations at both column ends at the end of test.

Figure 4.6 shows the global responses. Flexural strength degradation was obvious during the 3% drift cycles when LTB aggravated. Axial shortening was moderate during the 1.5% and 2% drift cycles due to the observed local buckling and moderate out-of-plane movements. As their amplitudes increased during the 3% drift cycles, axial shortening grew rapidly. As shown in Figure 4.6(d) and Figure 4.6(e) respectively, the column axial shortening history and the out-of-plane displacement history were similar in shape, indicating that the two quantities had a direct correlation due to geometry of the deformed specimen.

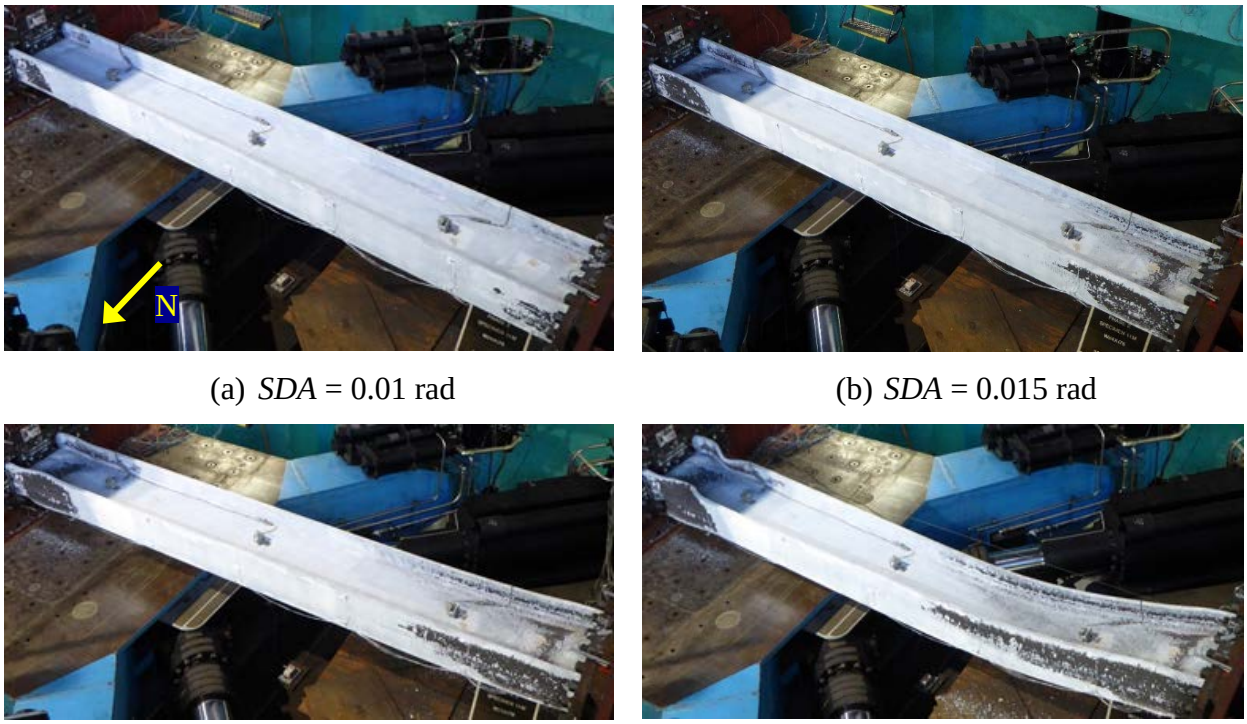

(a) *SDA* = 0.01 rad (b) *SDA* = 0.015 rad

(c) *SDA* = 0.02 rad (d) *SDA* = 0.03 rad

Figure 4.2 Specimen 11M: Overall Yielding and Buckling Progression

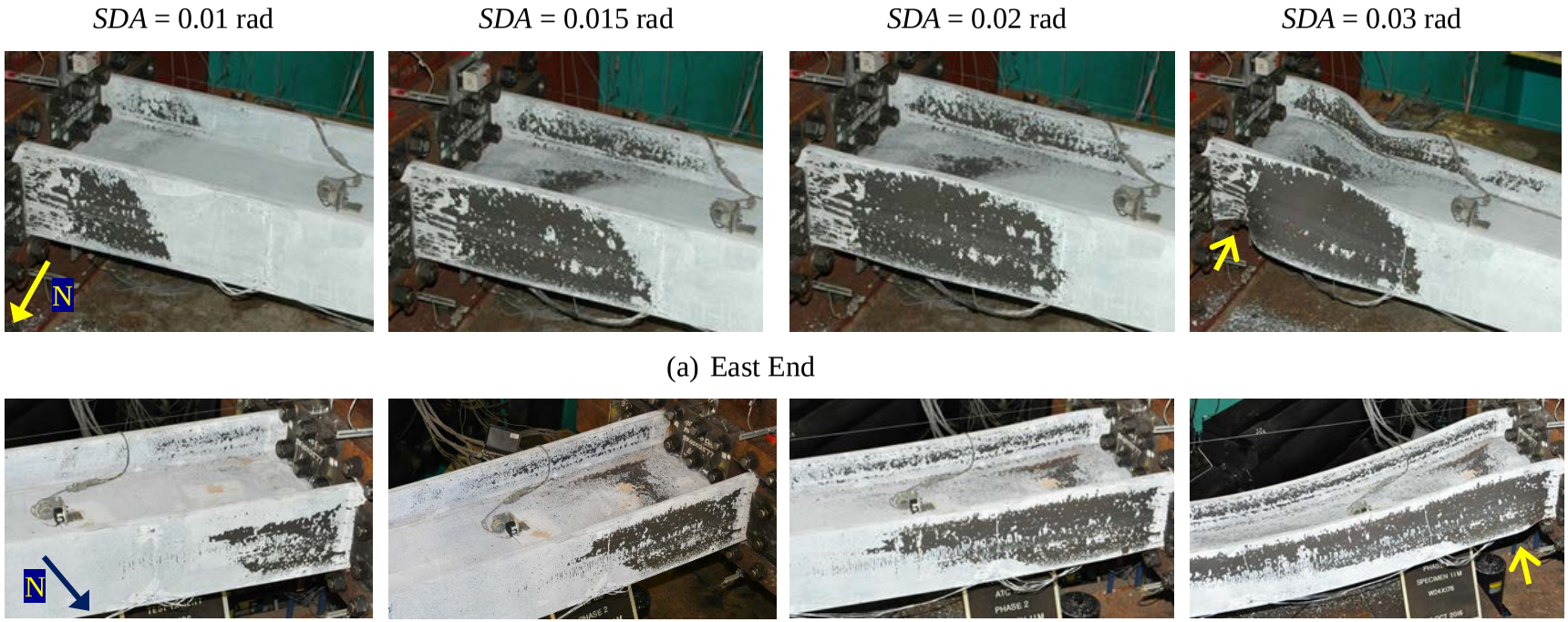

(a) East End

(b) West End

Figure 4.3 Specimen 11M: Yielding and Buckling Progression at Member Ends

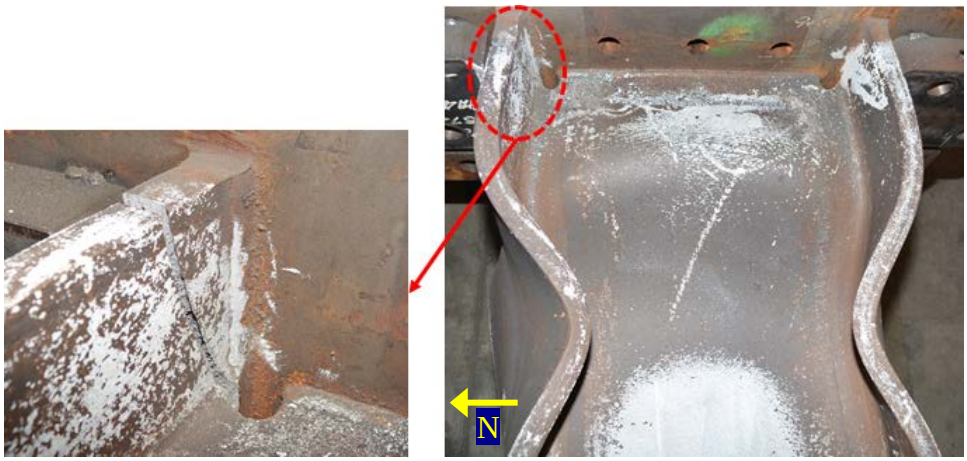

Figure 4.4 Specimen 11M: Column Fracture at End of Test (Northeast Flange)

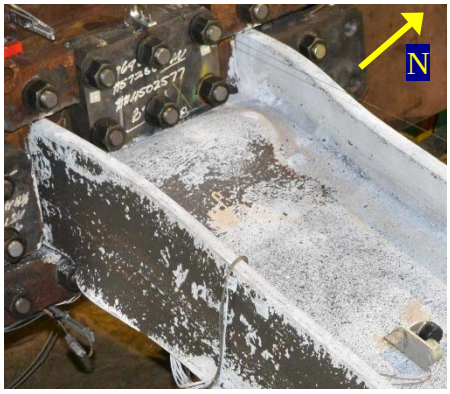

(a) Southwest Flange

(b) Northwest Flange

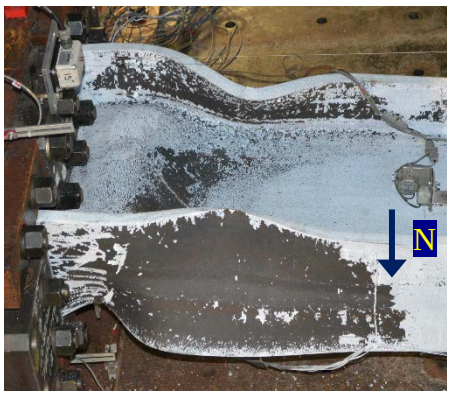

(c) Northeast Flange

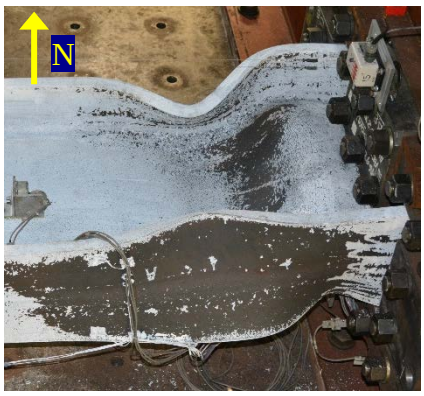

(d) Southeast flange

Figure 4.5 Specimen 11M: Local Buckling at End of Test

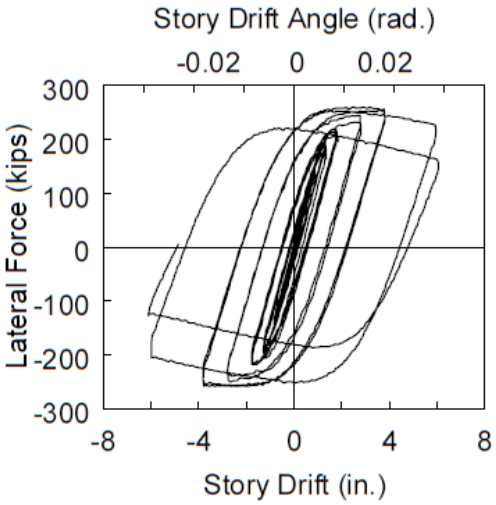

(a) Lateral Force vs. *SDA*

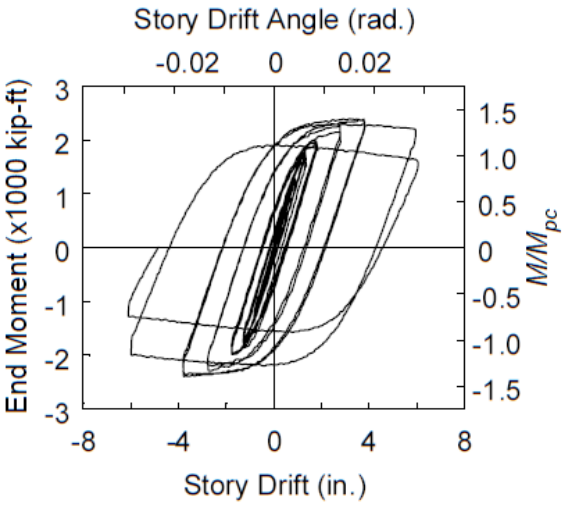

(b) End Moment vs. *SDA*

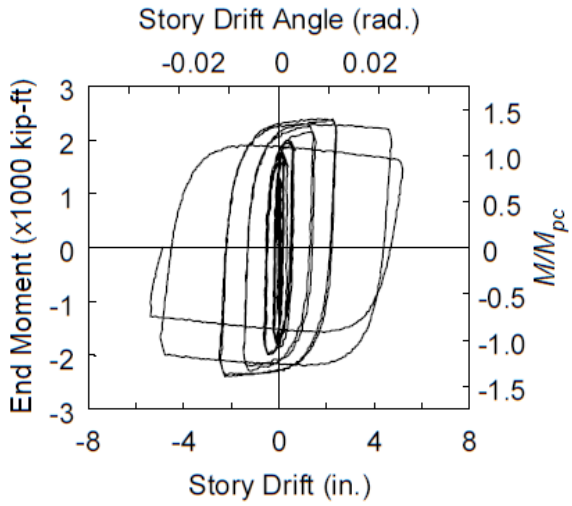

(c) End Moment vs. Plastic *SDA*

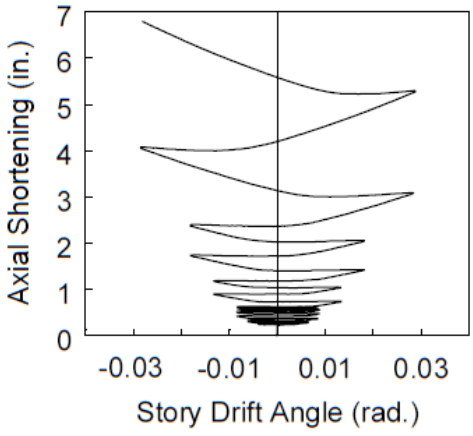

(d) Axial Shortening vs. *SDA*

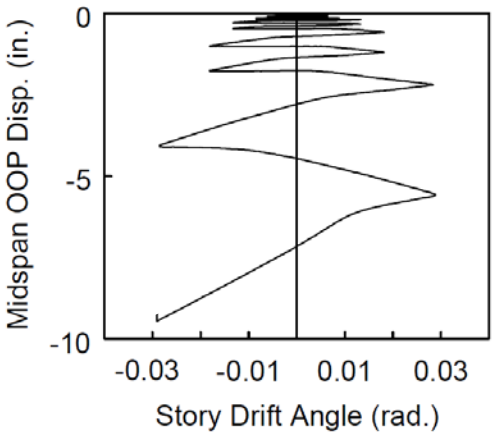

(e) Midspan OOP Disp. vs. *SDA*

Figure 4.6 Specimen 11M: Global Repsonses

4.2.3 Specimen 11H-VA

The governing failure mode of Specimen 11H-VA is CB with the single-curvature global configuration. Again, this specimen was subjected to the varying axial load sequence in conjunction with the AISC loading protocol (see Section 2.5). The lowest and highest axial compression ($C_a = 0.3$ to 0.6) was reached in the positive and negative drift, respectively. Yielding and buckling progression is illustrated in Figure 4.7 to Figure 4.9.

The sloped flaking pattern initiated at 1% drift. At 1.5% drift, minor LTB movements initiated at both ends. At 2% and 3% drifts, LTB of the specimen aggravated; during each cycle, compression flanges in the negative drift buckled downward out of plane more than those in positive drift since the former experienced a higher axial compression than the latter. Expansion of the sloped flaking pattern of the former demonstrated the immensity of their out-of-plane movements; in contrast, whitewash flaking of the latter was relatively limited corresponding to their less aggressive out-of-plane movements. The test was terminated after completing the first cycle at 3% drift due to excessive out-of-plane buckling. Figure 4.10 shows the ALB configuration (with minor amplitudes) at both column ends at the end of test.

Figure 4.11 shows the global responses. The end moment response indicated maximum flexural strengths of 1,980 and 2,580 kip-ft for the negative and positive excursions, respectively; the latter was 30% greater than the former because it sustained only half of the axial load applied to the former. Flexural strength degradation was apparent in the negative excursion of the 3% drift cycle corresponding to the severe LTB observed during testing. Axial shortening of Specimen 11H-VA grew rapidly starting at 2% drift corresponding to the aggravated out-of-plane, LTB-type movements. In Specimen 11M,

Figure 4.6(d) shows that axial shortening remained relatively constant when the specimen was unloaded in in-plane flexure. In Specimen 11H-VA, axial shortening slightly reduced in magnitude during the positive excursions due to the progressive decrease in axial compression.

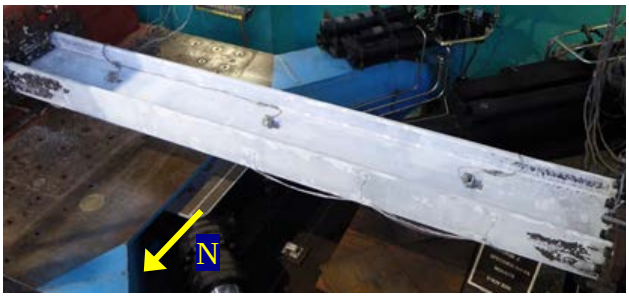

(a) *SDA* = 0.01 rad

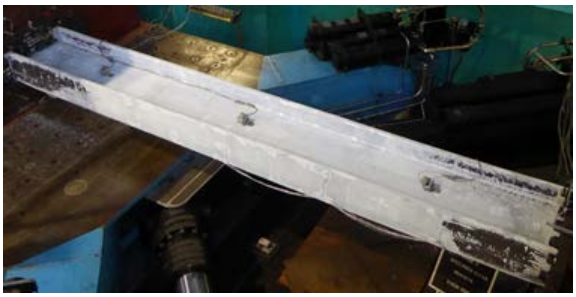

(b) *SDA* = 0.015 rad

(c) *SDA* = 0.02 rad

(d) *SDA* = 0.03 rad

Figure 4.7 Specimen 11H-VA: Overall Yielding and Buckling Progression

(a) *SDA* = 0.02 rad

(b) *SDA* = 0.03 rad

Figure 4.8 Specimen 11H-VA: Overall Yielding and Buckling Progression (Sideview)

(a) East End

(b) West End

Figure 4.9 Specimen 11H-VA: Yielding and Buckling Progression at Member Ends

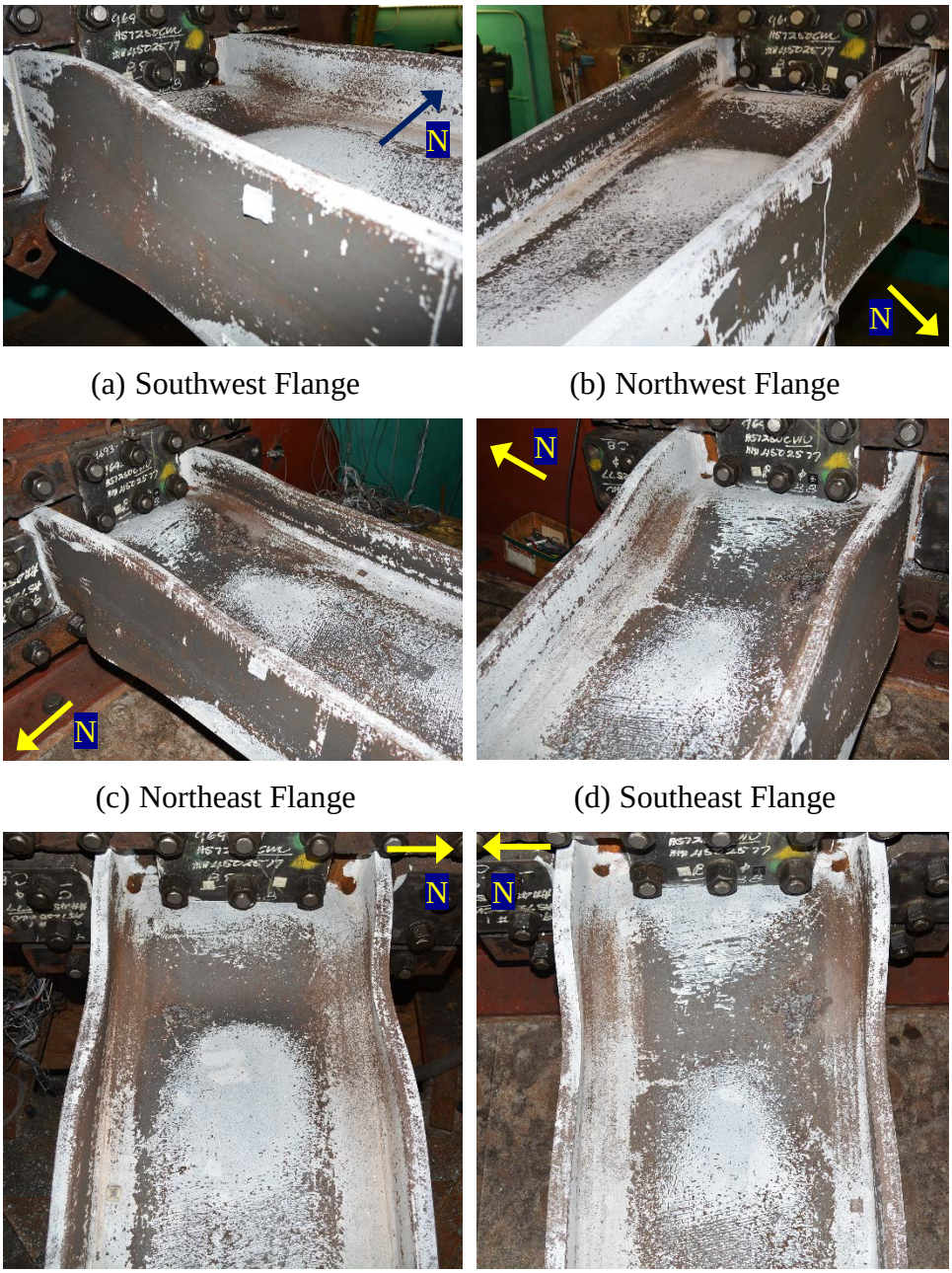

(a) Southwest Flange (b) Northwest Flange

(c) Northeast Flange (d) Southeast Flange

(e) West End (Top view) (f) East End (Top view)

Figure 4.10 Specimen 11H-VA: Local Buckling at End of Test

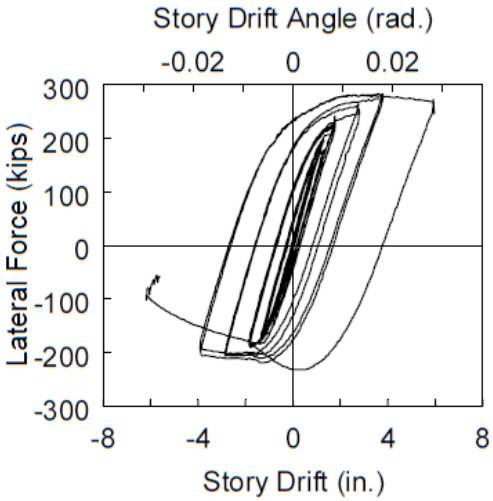

(a) Lateral Force vs. *SDA*

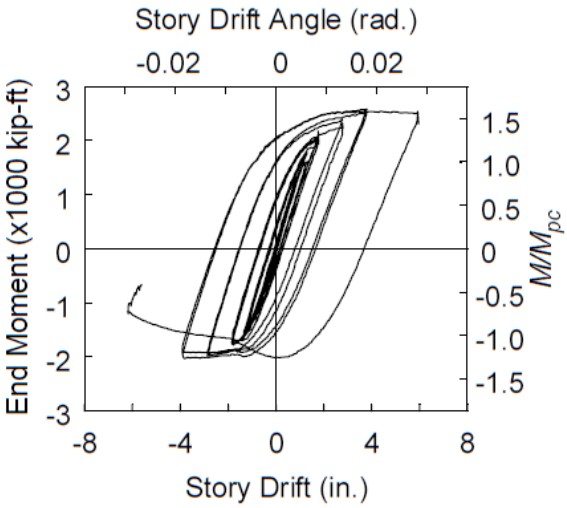

(b) End Moment vs. *SDA*

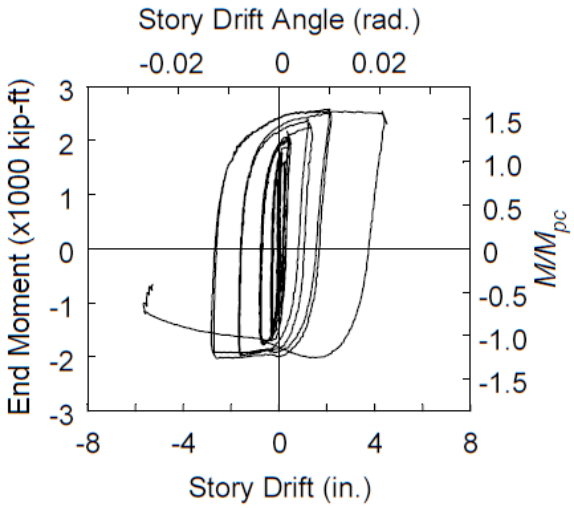

(c) End Moment vs. Plastic *SDA*

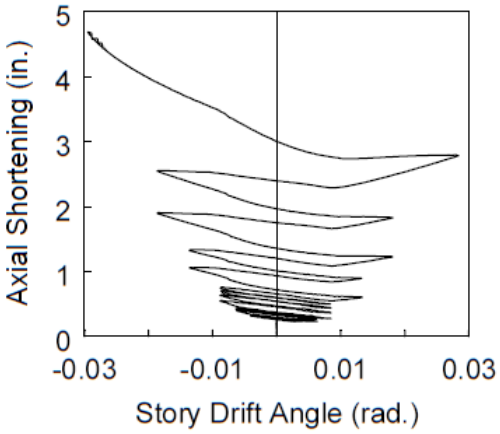

(d) Axial Shortening vs. *SDA*

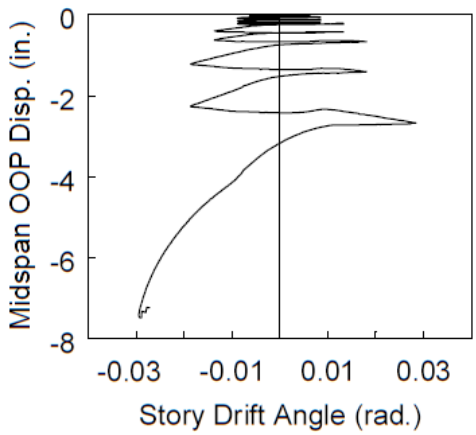

(e) Midspan OOP Disp. vs. *SDA*

Figure 4.11 Specimen 11H-VA: Global Responses

4.2.4 Specimen 11H-BC

The governing failure mode of Specimen 11H-BC is CB with the single-curvature global configuration. Yielding and buckling progression is illustrated in Figure 4.12 and Figure 4.14. No significant deformation was observed at the east (or rotating) end until 2% drift was reached. In contrast, the sloped flaking pattern initiated at 1% drift at the west (or fixed) end. At 1.5% drift, downward LTB movements initiated at the west end; a web local buckle with a minor amplitude was also observed. LTB of the specimen exacerbated at 2% drift: the west flange under compression in positive drift and that in negative drift buckled out of plane more during the positive and negative excursions of each cycle, respectively. This induced flange local buckling at the bottom half-width flanges at the west end as shown with arrows in Figure 4.14 (for *SDA* = 0.02 and 0.0225 rad) and Figure 4.13. The test was terminated after reaching 2.25% drift due to the excessive out-of-plane buckling. Note the contrast between the extents of yielding at the west (i.e., fixed) and east (i.e., rotating) ends by the end of the test.

Figure 4.15 shows the global responses. Flexural strength at the west end degraded significantly during the 2% drift cycles when LTB at the west end became more severe. In addition, the onset of LTB at 1.5% drift boosted the axial shortening rate from that point onward.

4.2.5 Concluding Remarks

Group 11 testing demonstrated that the same CB failure mode observed in Phase 1 testing could be reproduced. Furthermore, the effects of varying axial load and fixed-rotating boundary conditions did not alter the governing failure mode associated with this section.

(a) *SDA* = 0.0075 rad (b) *SDA* = 0.01 rad

(c) *SDA* = 0.015 rad (d) *SDA* = 0.02 rad

Figure 4.12 Specimen 11H-BC: Overall Yielding and Buckling Progression

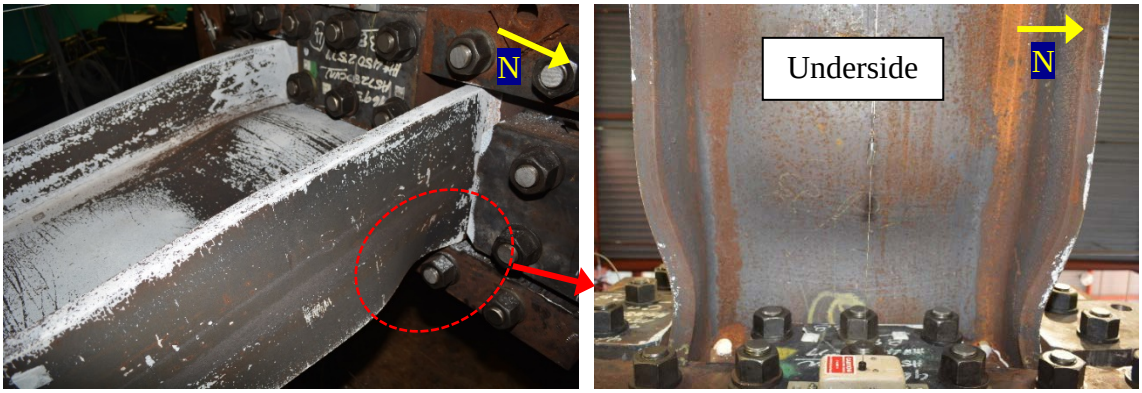

Figure 4.13 Specimen 11H-BC: LTB-induced Flange Local Buckling at End of Test (West End)

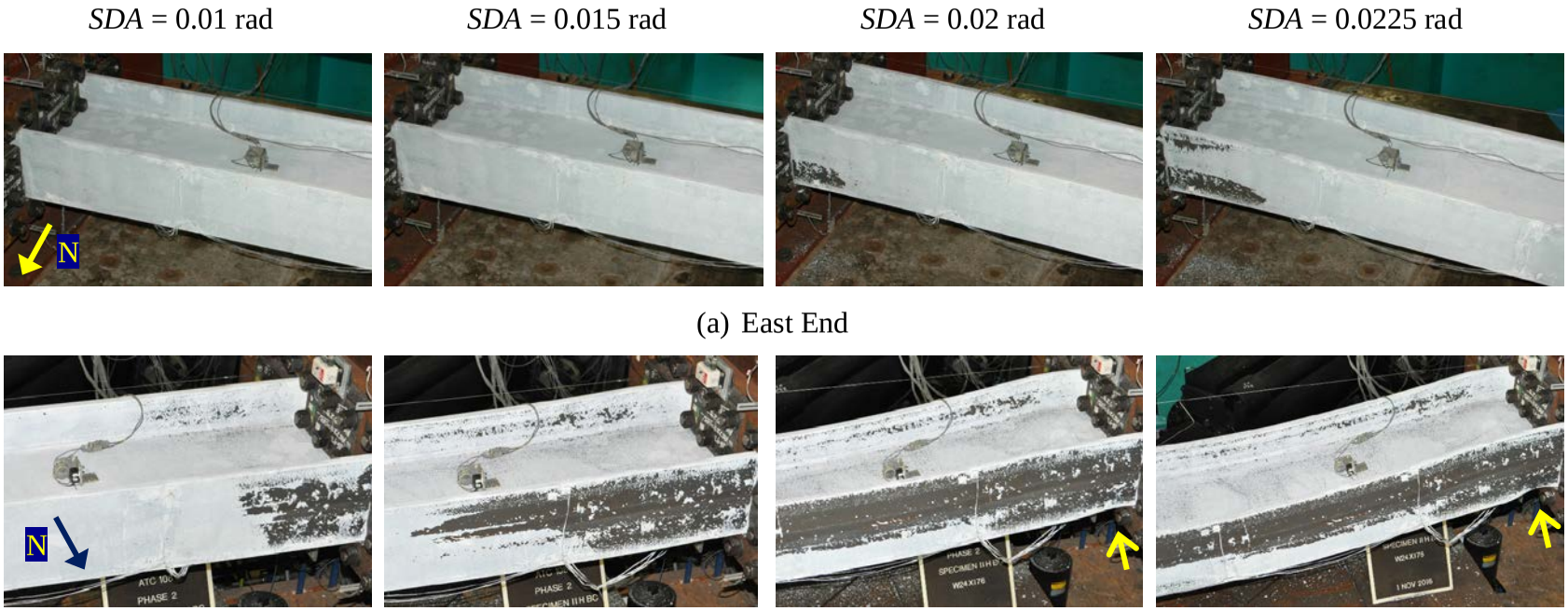

(a) East End

(b) West End

Figure 4.14 Specimen 11H-BC: Yielding and Buckling Progression at Member Ends

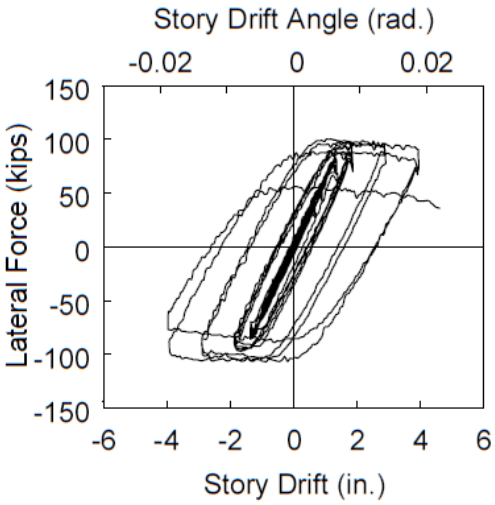

(a) Lateral Force vs. *SDA*

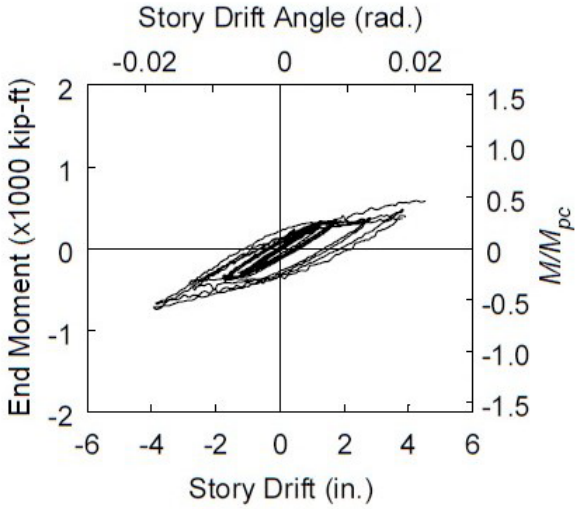

(b) East End Moment vs. *SDA*

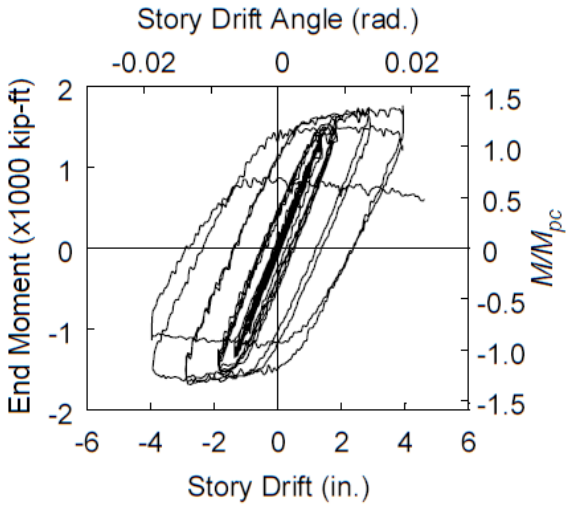

(c) West End Moment vs. *SDA*

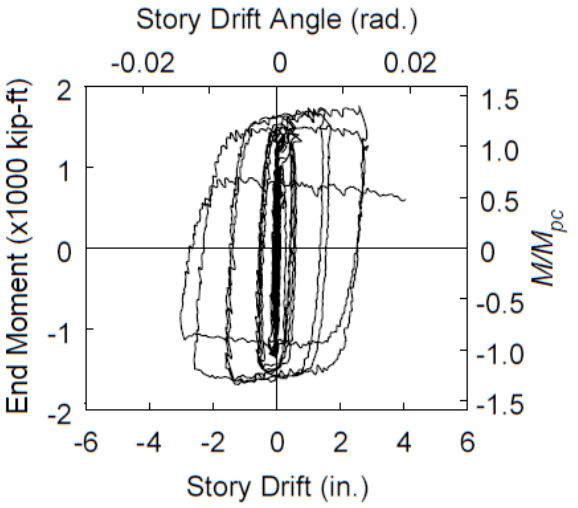

(d) West End Moment vs. Plastic *SDA*

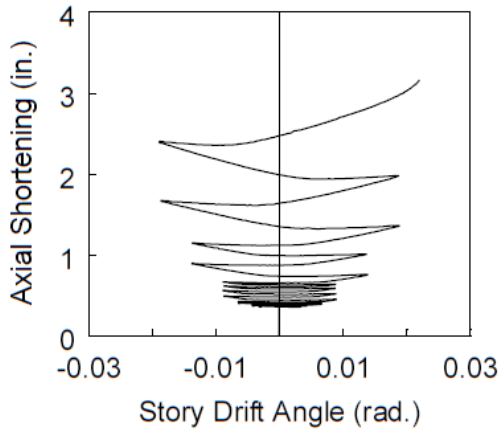

(e) Axial Shortening vs. *SDA*

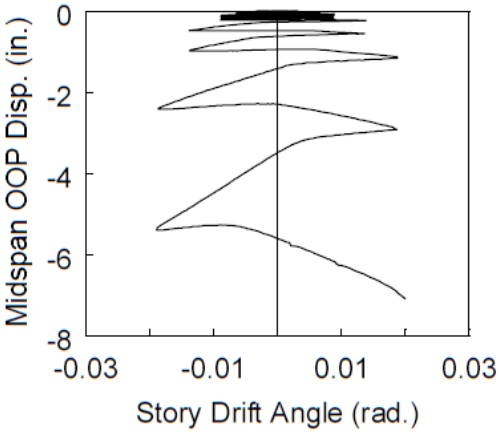

(f) Midspan OOP Disp. vs. *SDA*

Figure 4.15 Specimen 11H-BC: Global Responses

4.3 Group 13 Specimens: Section W30×173

4.3.1 General

Web and flange slenderness of Group 13 specimens was similar to that of Group 2 specimens with W24×131 section, which experienced the ALB failure mode. Test results from these groups were compared to study the effect of section depths on column inelastic cyclic responses involving in-plane plastic hinging. To investigate boundary condition effect, Specimens 13M and 13M-BC were subjected to fixed-fixed and fixed-rotating boundary conditions, respectively. Loading sequence of the latter boundary condition test was discussed in Chapter 2. Both specimens sustained constant axial load with $C_a = 0.4$.

4.3.2 Specimen 13M

Specimen 13M exhibited the ALB failure mode; Figure 4.16 and Figure 4.17 depict yielding and buckling progression. Web and flange local buckling was first observed at both ends at 1% drift; apexes of the outward flange local buckles located closer to the end plates than those of the inward ones. The buckled elements underwent larger deformation at 1.5% drift, forming plastic hinges at the column ends. No out-of-plane, LTB-type motion was observed. Yield length was much shorter than that observed in testing of Group 11 specimens, which experienced the CB mode. Due to excessive web local buckling, the test was terminated after completing the positive excursion of the second 1.5% drift cycle.

Figure 4.18 shows the global responses. Flexural strength degradation began during the 1% drift cycles corresponding to the onset of web and flange local buckling. The specimen lost its flexural capacity rapidly, decreasing to 75% of its maximum moment capacity after four cycles of 1% drift. The onset of web and flange local buckling also

triggered significant axial shortening, which continued to grow in proportion to the amplitudes of the local buckling.

(a) *SDA* = 0.005 rad

(b) *SDA* = 0.0075 rad

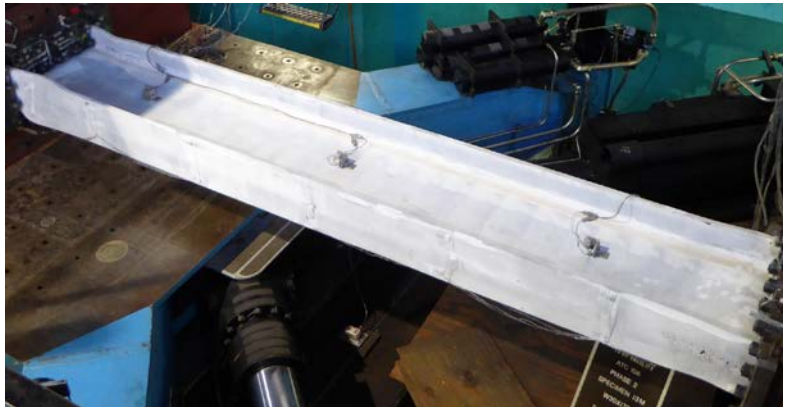

(c) *SDA* = 0.01 rad

(d) *SDA* = 0.015 rad

Figure 4.16 Specimen 13M: Overall Yielding and Buckling Progression

(a) East End

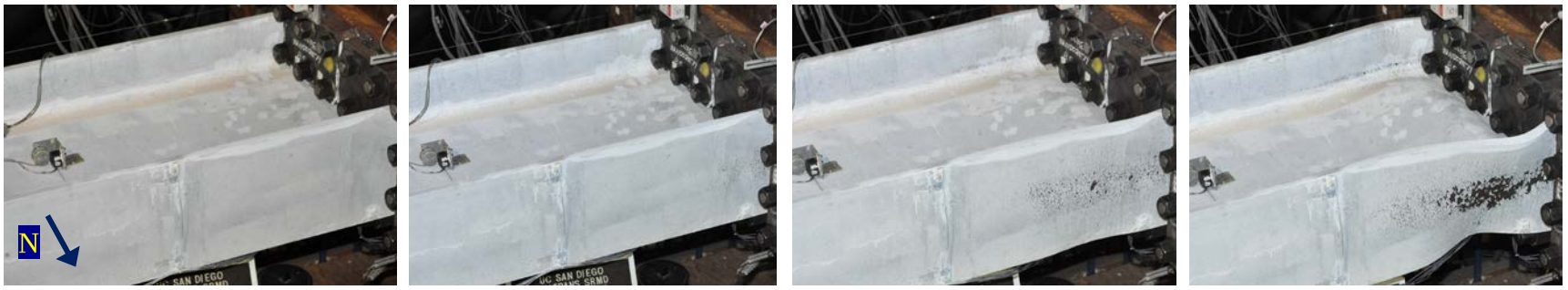

(b) West End

Figure 4.17 Specimen 13M: Yielding and Buckling Progression at Member Ends

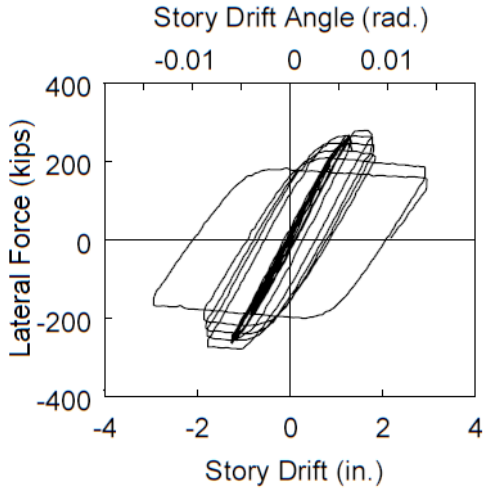

(a) Lateral Force vs. *SDA*

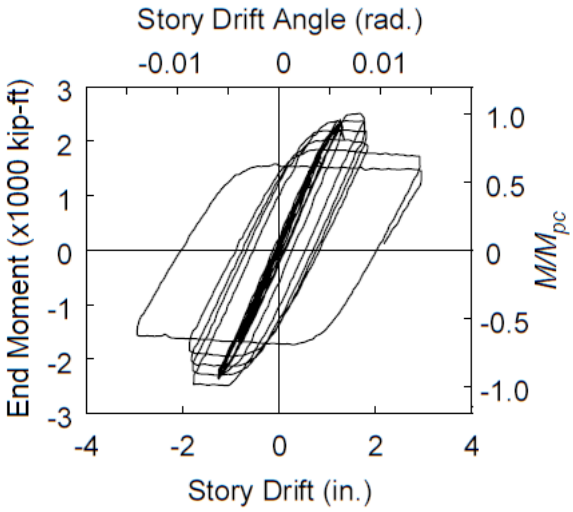

(b) End Moment vs. *SDA*

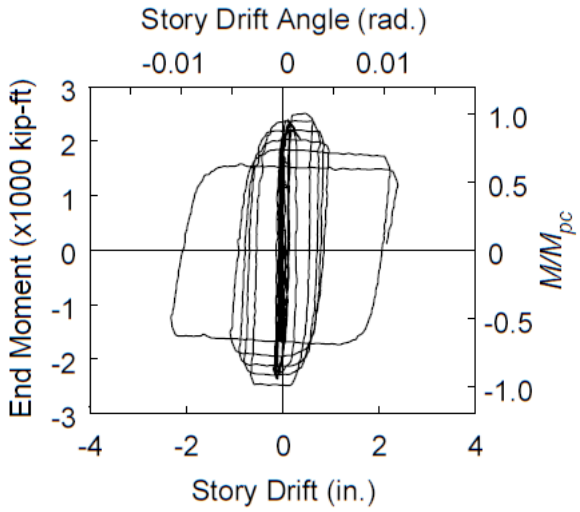

(c) End Moment vs. Plastic *SDA*

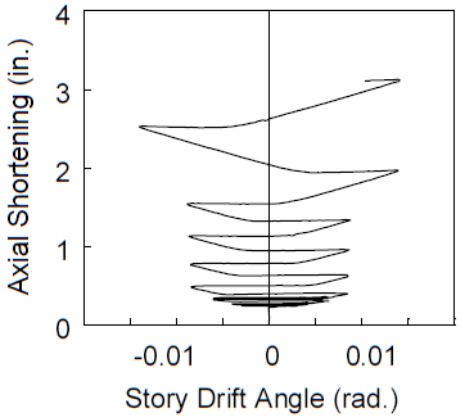

(d) Axial Shortening vs. *SDA*

Figure 4.18 Specimen 13M: Global Responses

4.3.3 Specimen 13M-BC

Like Specimen 13M, Specimen 13M-BC experienced the ALB failure mode. As expected in a boundary condition test, neither plastic deformation nor local buckling occurred at the east (or rotating) end. In contrast, web and flange local buckling initiated at the west (or fixed) end at 1.5% drift as demonstrated in Figure 4.19 and Figure 4.20; the ALB configuration was observed. LTB behavior was not observed in this specimen.

Figure 4.21 illustrates the global responses. Entering 1.5% drift, flexural strength of the specimen began to degrade corresponding to the onset of local buckling at the west end; it reduced to 62% of the maximum flexural strength after completing two cycles at 1.5% drift. In addition, the formation of local buckles triggered a rapid increase in axial shortening during the 1.5% drift cycles and beyond.

In comparison, Specimens 13M and 13M-BC experienced ALB at 1% and 1.5% drift, respectively. This demonstrated the effect of the fixed-rotating boundary conditions; the applied end rotation helped relieving some of the flexural moment demand that would have been produced with fixed-fixed boundary conditions at the same drift level. As a result, the specimen with fixed-rotating boundary conditions could withstand larger story drifts before it failed. Despite this difference, the global responses of Specimen 13M-BC had a similar characteristic to those of Specimen 13M.

4.3.4 Concluding Remarks

As predicted, ALB was the failure mode although the depth of this W30 section was larger than that of Group 2 specimens (W24) tested in Phase 1. Allowing one end of the column to rotate produced plastic hinging at one end (i.e., fixed end) only, but it did not alter the governing buckling mode.

(a) *SDA* = 0.0075 rad

(b) *SDA* = 0.01 rad

(c) *SDA* = 0.015 rad

(d) *SDA* = 0.02 rad

Figure 4.19 Specimen 13M-BC: Overall Yielding and Buckling Progression

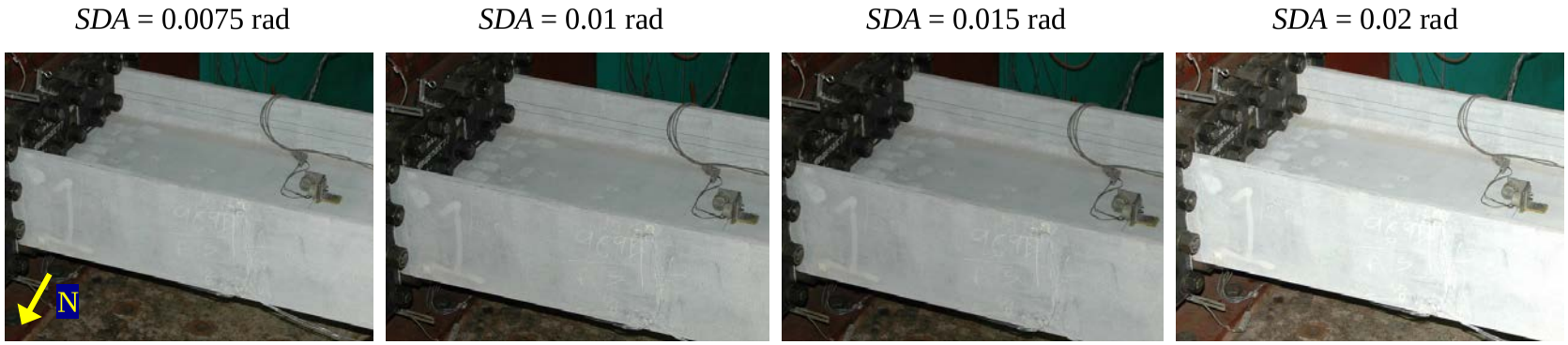

(a) East End

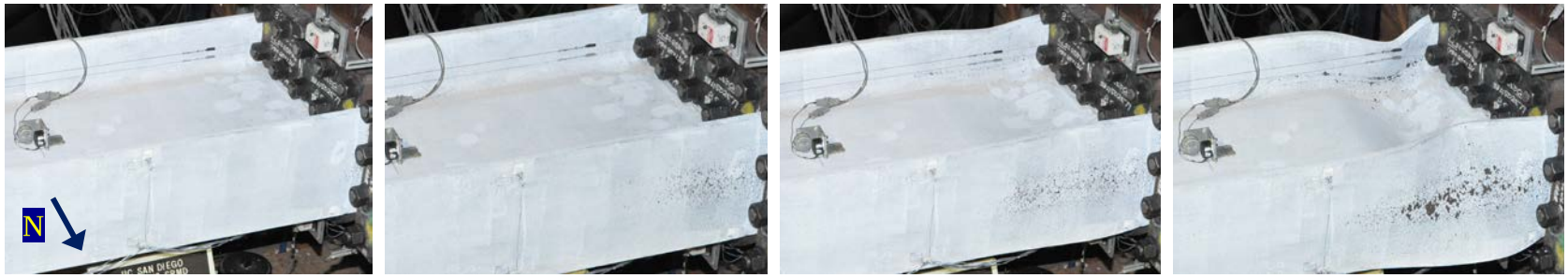

(b) West End

Figure 4.20 Specimen 13M-BC: Yielding and Buckling Progression at Member Ends

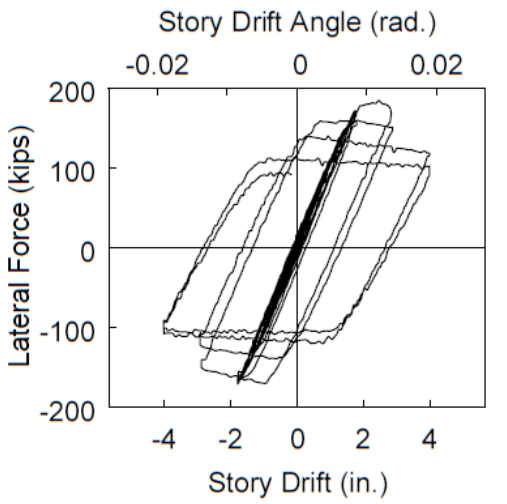

(a) Lateral Force vs. *SDA*

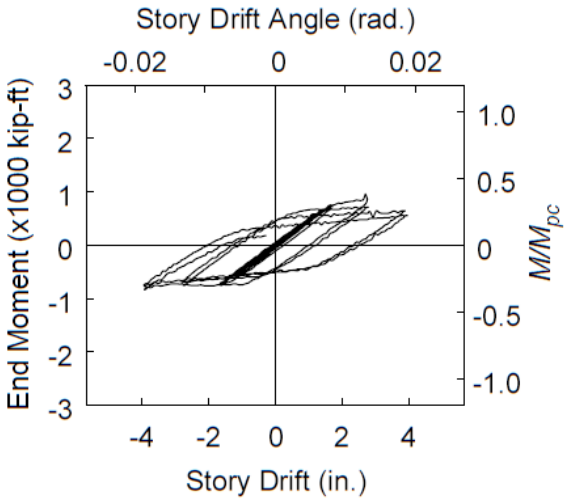

(b) East End Moment vs. *SDA*

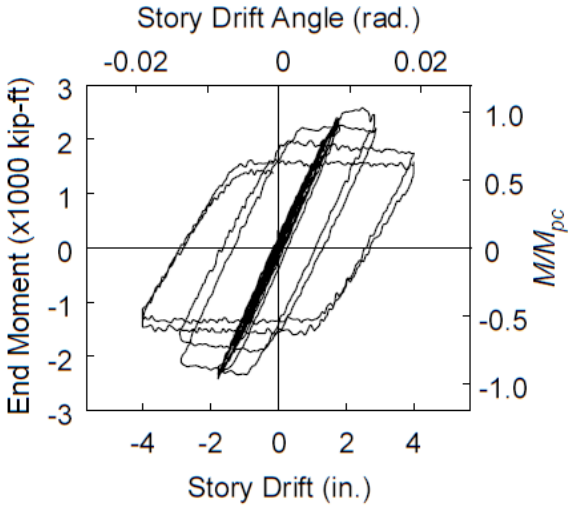

(c) West End Moment vs. *SDA*

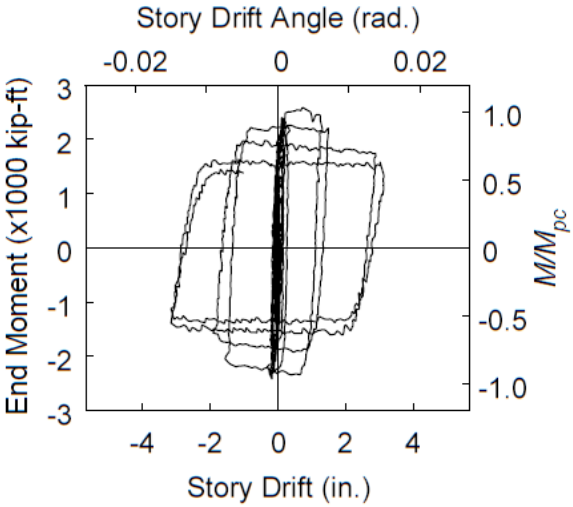

(d) West End Moment vs. Plastic *SDA*

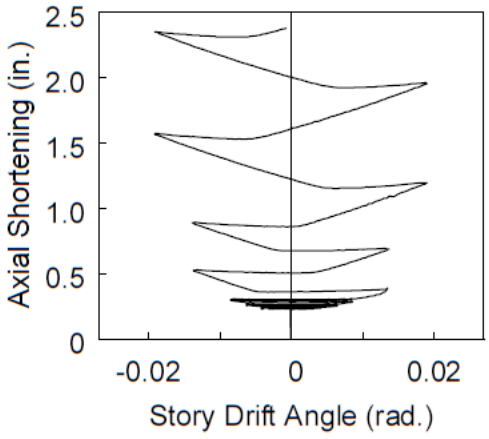

(e) Axial Shortening vs. *SDA*

Figure 4.21 Specimen 13M-BC: Global Responses

4.4 Group 16 Specimens: Section W18×130

4.4.1 General

Two W18×130 specimens were tested in this group to study the boundary condition and section depth effects; the section had similar slenderness properties to those of Group 1 (and Group 11) specimens. Both specimens were subjected to the AISC loading protocol and constant axial compression with $C_a = 0.4$. For Specimen 16M-BC, the end rotation sequence discussed in Section 2.6.3 was also applied at the east (or moving) end to simulate rotation at the top end of a first-story column in an SMF.

4.4.2 Specimen 16M

The governing failure mode of Specimen 16M is CB with the single-curvature global configuration; yielding and buckling progression is shown in Figure 4.22 and Figure 2.16. The sloped flaking pattern was apparent at 1% drift. At 2% drift, LTB movements initiated; at 3% drift, they exacerbated with compression flanges buckling out of plane more during each cycle. This led to a significant downward out-of-plane displacement at the column midspan. Corresponding to this out-of-plane curvature, an LTB-induced flange local buckle formed at each bottom half-width flange at each end (see the arrowed locations in Figure 4.23). The test was terminated due to the excessive downward displacement and significant flexural strength degradation in the specimen.

Figure 4.24 shows the global responses. Flexural strength was stable throughout the 2% drift cycles even though LTB had initiated in some degree. After completing the first 3% drift cycle, flexural strength reduced to 86% of the maximum value despite considerable out-of-plane buckling in the specimen. Very significant flexural strength degradation was observed during the positive excursion of the second 3% drift cycle, at

which point the out-of-plane displacement increased rapidly. As shown in Figure 4.24(d) and Figure 4.24(e) respectively, the column axial shortening history and the out-of-plane displacement history were similar in shape, indicating that the two quantities had a direct correlation due to geometry of the deformed specimen.

(a) *SDA* = 0.01 rad

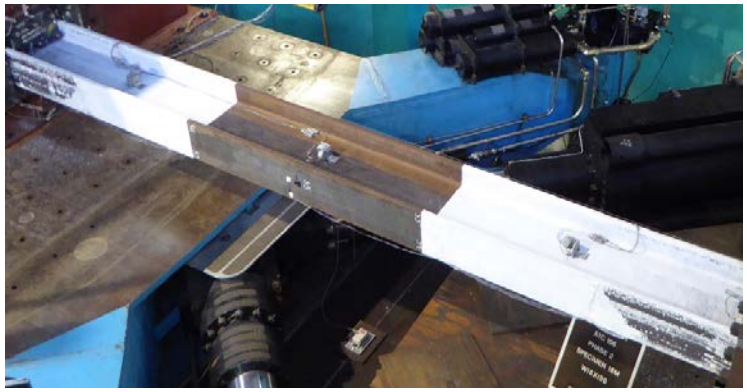

(b) *SDA* = 0.015 rad

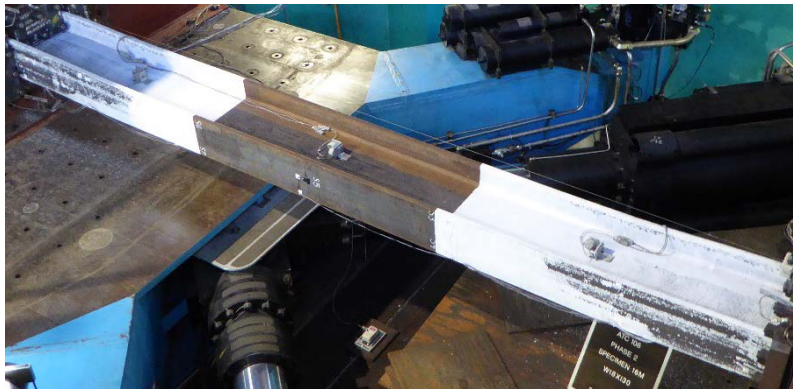

(c) *SDA* = 0.02 rad

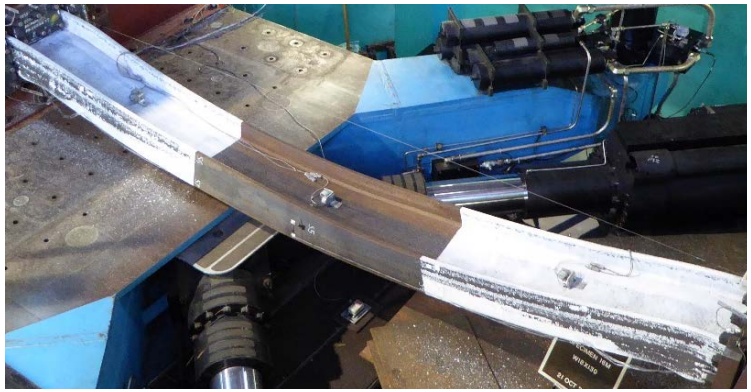

(d) *SDA* = 0.03 rad

Figure 4.22 Specimen 16M: Overall Yielding and Buckling Progression

SDA = 0.01 rad | *SDA* = 0.015 rad | *SDA* = 0.02 rad | *SDA* = 0.03 rad

(a) East End

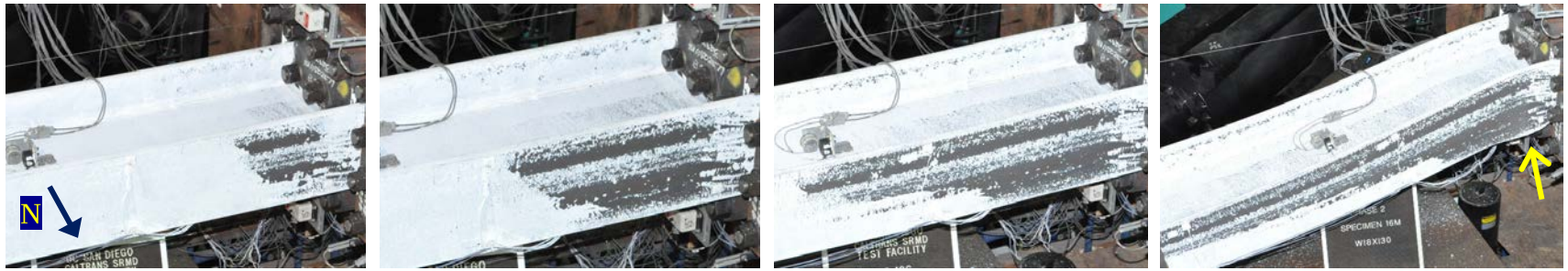

(b) West End

Figure 4.23 Specimen 16M: Yielding and Buckling Progression at Member Ends

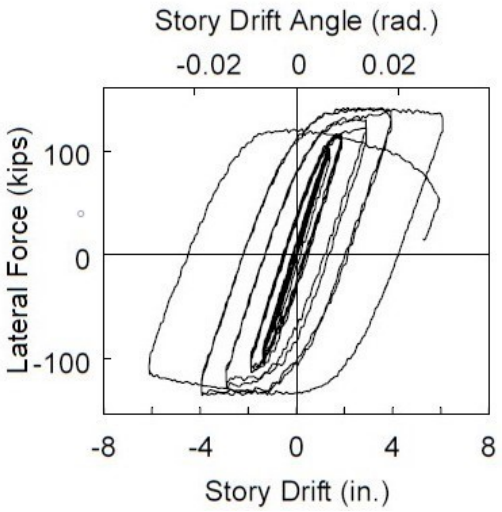

(a) Lateral Force vs. *SDA*

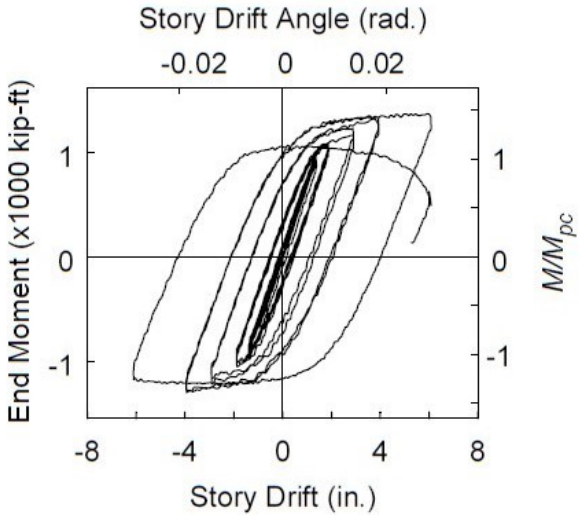

(b) End Moment vs. *SDA*

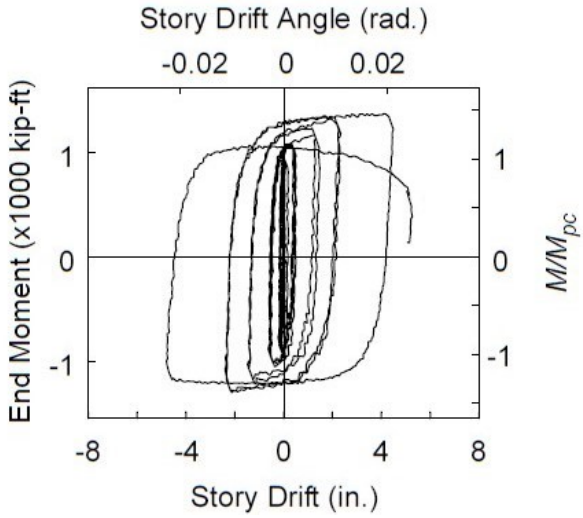

(c) End Moment vs. Plastic *SDA*

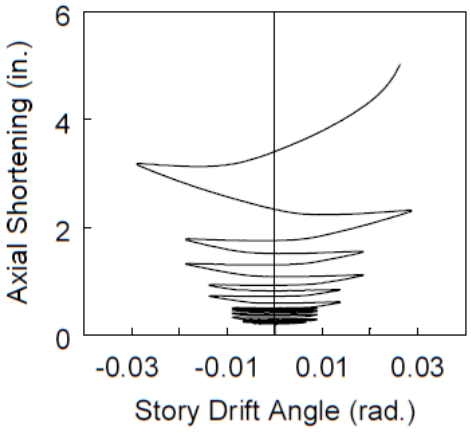

(d) Axial Shortening vs. *SDA*

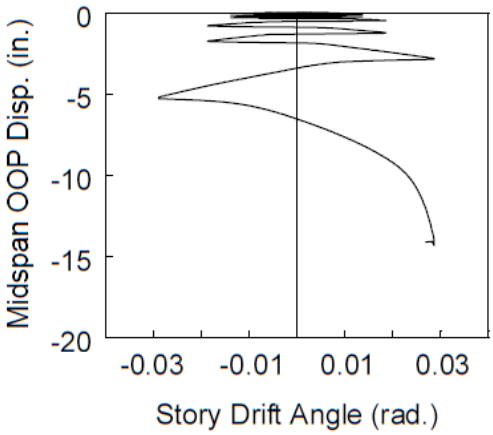

(e) Midspan OOP Disp. vs. *SDA*

Figure 4.24 Specimen 16M: Global Responses

4.4.3 Specimen 16M-BC

Like Specimen 16M, Specimen 16M-BC experienced the CB failure mode with the single-curvature global configuration; yielding and buckling progression is illustrated in Figure 4.25 and Figure 4.26. As expected in a boundary condition test, no significant deformation was observed at the east end; it remained mostly elastic and underwent some yielding toward the end of the test. At the west end, the sloped flaking pattern initiated at 2% drift. Successively at 3% drift, LTB of the specimen initiated and exacerbated at 4% drift: the west flange under compression in positive drift and that in negative drift buckled upward out of plane more during the positive and negative excursions of each cycle, respectively. The exacerbated LTB movements caused a rapid increase in the column out-of-plane displacement, which concentrated near the west end. Corresponding to this out-of-plane curvature, an LTB-induced flange local buckle formed at each top half-width flange at the west end as shown in Figure 4.27. Significant flexural strength degradation in the specimen during the 4% drift cycles prompted the termination of the test.

Figure 4.28 shows the global responses. Flexural strength remained stable during the 3% drift cycles despite the considerable development of the out-of-plane buckling near the west end. Strength degradation prevailed at 4% drift, corresponding to when the drastic out-of-plane movements occurred. Due to geometry of the deformed specimen, axial shortening aggravated proportionally to the amplitudes of the out-of-plane buckling. In comparison, Specimens 16M and 16M-BC reached their peak flexural strengths at 2% and 3% drift, respectively, and experienced strength degradation at 3% and 4% drift, respectively. This demonstrated the effect of the fixed-rotating boundary conditions; the applied end rotation helped relieving some of the flexural moment demand that would have

been produced with fixed-fixed boundary conditions at the same drift level. As a result, the specimen with fixed-rotating boundary conditions could withstand larger story drifts before it failed. Despite this difference, the global responses of Specimen 16M-BC had a similar characteristic to those of Specimen 16M.

4.4.4 Concluding Remarks

As predicted, CB was the failure mode although the depth of this W18 section was shallower than that of Groups 1 and 11 specimens (W24). Allowing one end of the column to rotate did not alter the governing buckling mode.

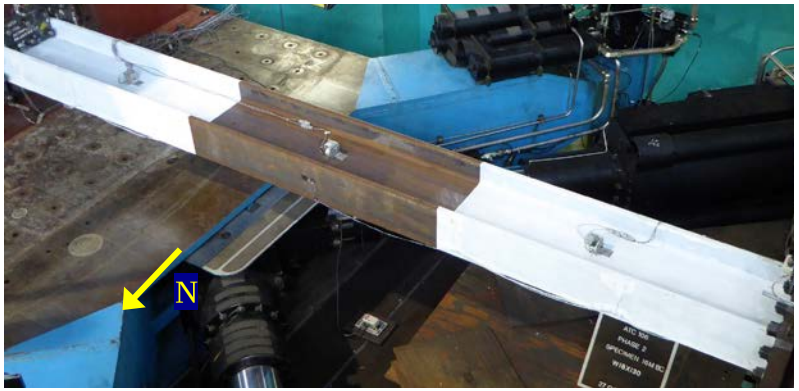

(a) *SDA* = 0.01 rad

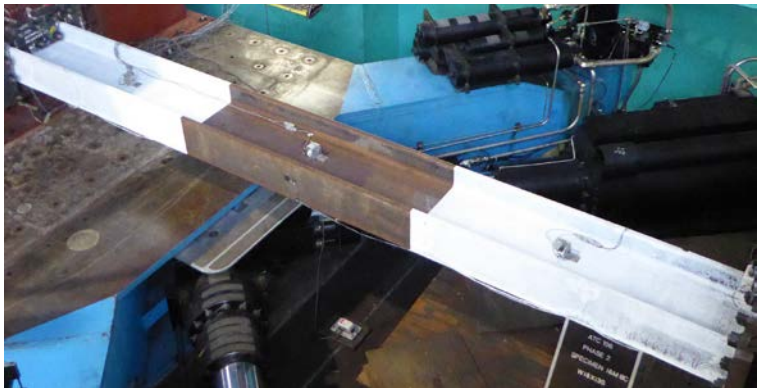

(b) *SDA* = 0.02 rad

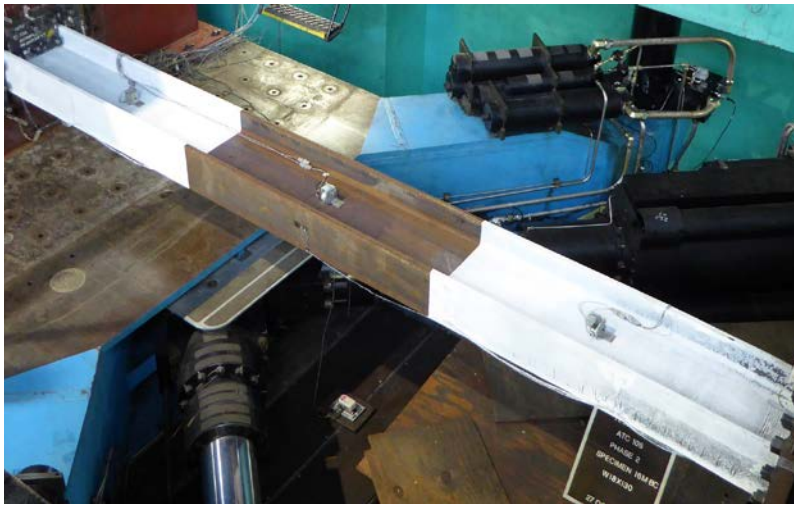

(c) *SDA* = 0.03 rad

(d) *SDA* = 0.04 rad

Figure 4.25 Specimen 16M-BC: Overall Yielding and Buckling Progression

(a) East End

(b) West End

Figure 4.26 Specimen 16M-BC: Yielding and Buckling Progression at Member Ends

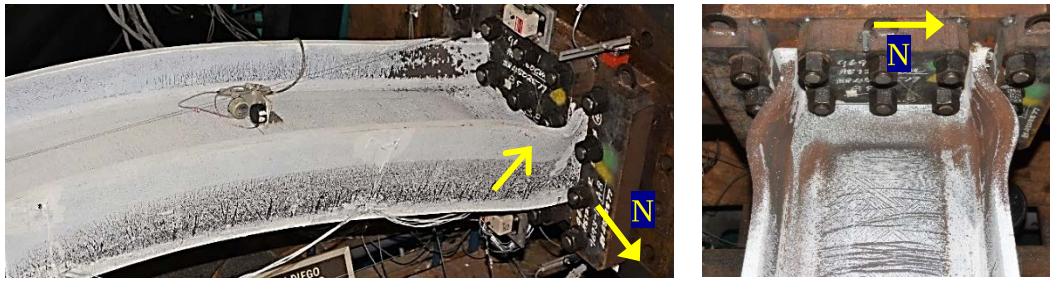

Figure 4.27 Specimen 16M-BC: LTB-induced Flange Local Buckling at West End

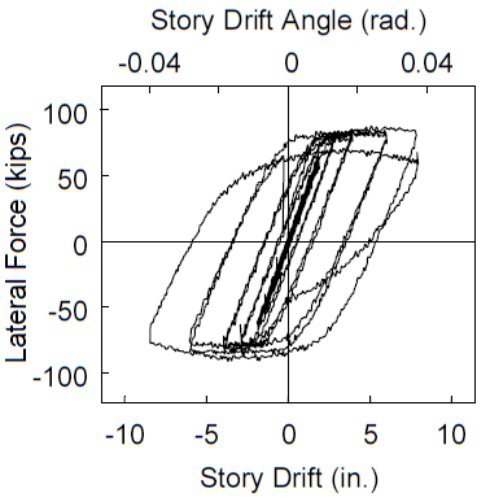

(a) Lateral Force vs. *SDA*

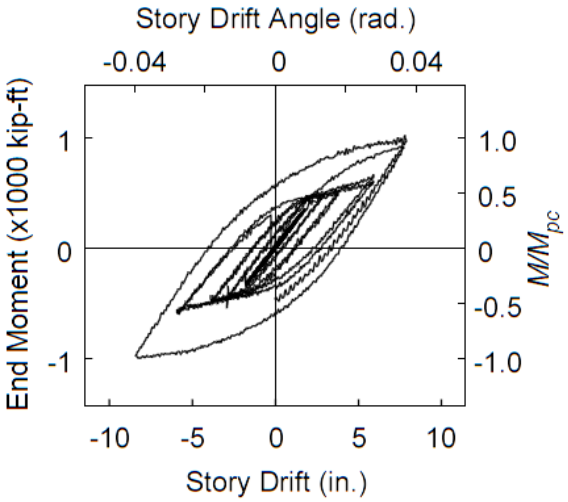

(b) East End Moment vs. *SDA*

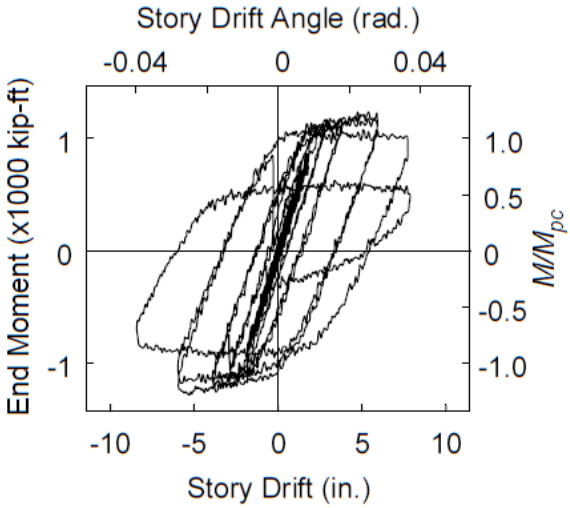

(c) West End Moment vs. *SDA*

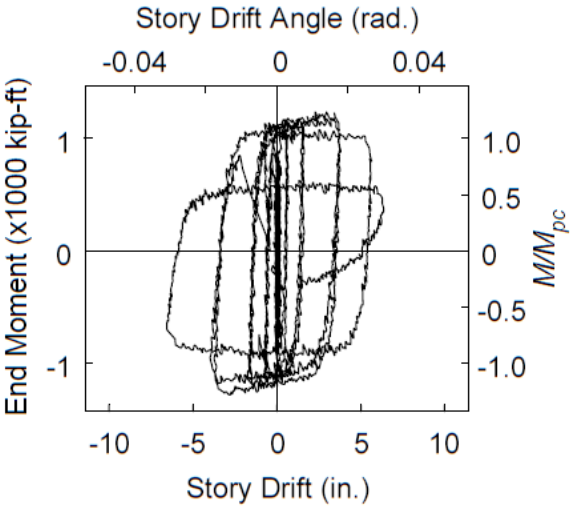

(d) West End Moment vs. Plastic *SDA*

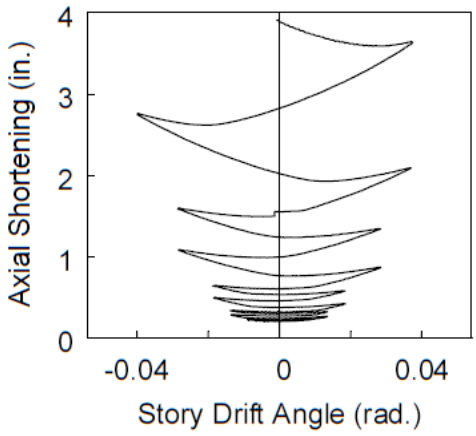

(e) Axial Shortening vs. *SDA*

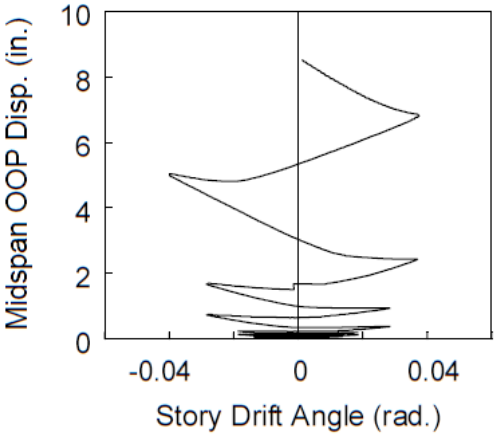

(f) Midspan OOP Disp. vs. *SDA*

Figure 4.28 Specimen 16M-BC: Global Responses

4.5 Group 21 Specimens: Section W18×130

4.5.1 General

In Group 16, two W18×130 specimens—Specimens 16M and 16M-BC—were tested with constant axial compression ($C_a = 0.4$); Specimen 16M -BC was also subjected to the end rotation sequence in conjunction with the typical AISC loading protocol. In this group, four specimens with the same section and geometry as Group 16 specimens were tested with four different loading scenarios. Specimen 21M-VAM was subjected to varying compressive axial load with C_a ranging from 0.1 to 0.7, while Specimen 21M-VAU was subjected to varying tensile and compressive axial load with C_a ranging from -0.2 (tension) to 0.4 (compression). Note that the former axial load sequence had its *mean* C_a value equal to 0.4; in contrast, the C_a value of 0.4 represented the *upper bound* value in the latter axial load sequence. In both cases, the axial load range (ΔC_a) remained the same (= 0.6). Specimen 21M-NF was tested with the near-fault loading protocol. Lastly, Specimen 21M-VAU-BC was subjected to both varying axial load and the end rotation sequence. Characteristics of all loading scenarios were discussed in Section 2.6.

4.5.2 Specimen 21M-VAM

The governing failure mode of Specimen 21M-VAM is CB with the single-curvature global configuration; yielding and buckling progression is shown in Figure 4.29 and Figure 4.30. Local buckling was not observed before the sloped flaking pattern and LTB movements initiated at 1.5% and 2% drift, respectively. LTB movements were triggered in the first negative excursion at 2% drift when axial compression increased to its highest amplitude ($C_a = 0.7$). They exacerbated at 3% drift: during each cycle,

compression flanges in the negative drift buckled out of plane more than those in positive drift since the former experienced higher combined axial and in-plane flexural compression than the later. In addition, out-of-plane amplitudes of the former decreased (or recovered) somewhat in the positive excursions due to the progressive decrease in axial compression. Since axial shortening grew proportionally to the out-of-plane amplitudes, it also recovered somewhat in the positive excursions as shown in Figure 4.33(d).

Significant LTB movements induced flange local buckling at both column ends as shown in Figure 4.31. At the west end, the two half-wave buckles formed at the top half-width flanges; at the east end, they formed at the top and bottom half-width flanges of the northeast and southeast flanges, respectively. The former appeared to be triggered primarily by out-of-plane stresses while the later appeared to be induced primarily by warping stresses due to significant twisting at the east end as shown in Figure 4.32.

Influenced by web-flange interactions, the web at each end also buckled in the direction that conformed to the flange local buckling configurations. In summary, global buckling occurred first in this specimen, followed by local buckling. It will be shown later that the order was reversed for Specimen 27L; local buckling initiated before global buckling was triggered.

Figure 4.33 shows the global responses. The specimen exhibited higher plastic moment capacity in the positive excursions compared to that in the negative excursions since lower axial compression was applied in the former. A drastic flexural strength degradation occurred during the second negative excursion at 3% drift as the applied axial load progressively returned to its highest amplitude. Axial shortening began to grow at an increasing rate at 2% drift, corresponding to the onset of LTB movements.

(a) *SDA* = 0.01 rad

(b) *SDA* = 0.015 rad

(c) *SDA* = 0.02 rad

(d) *SDA* = 0.03 rad

Figure 4.29 Specimen 21M-VAM: Overall Yielding and Buckling Progression

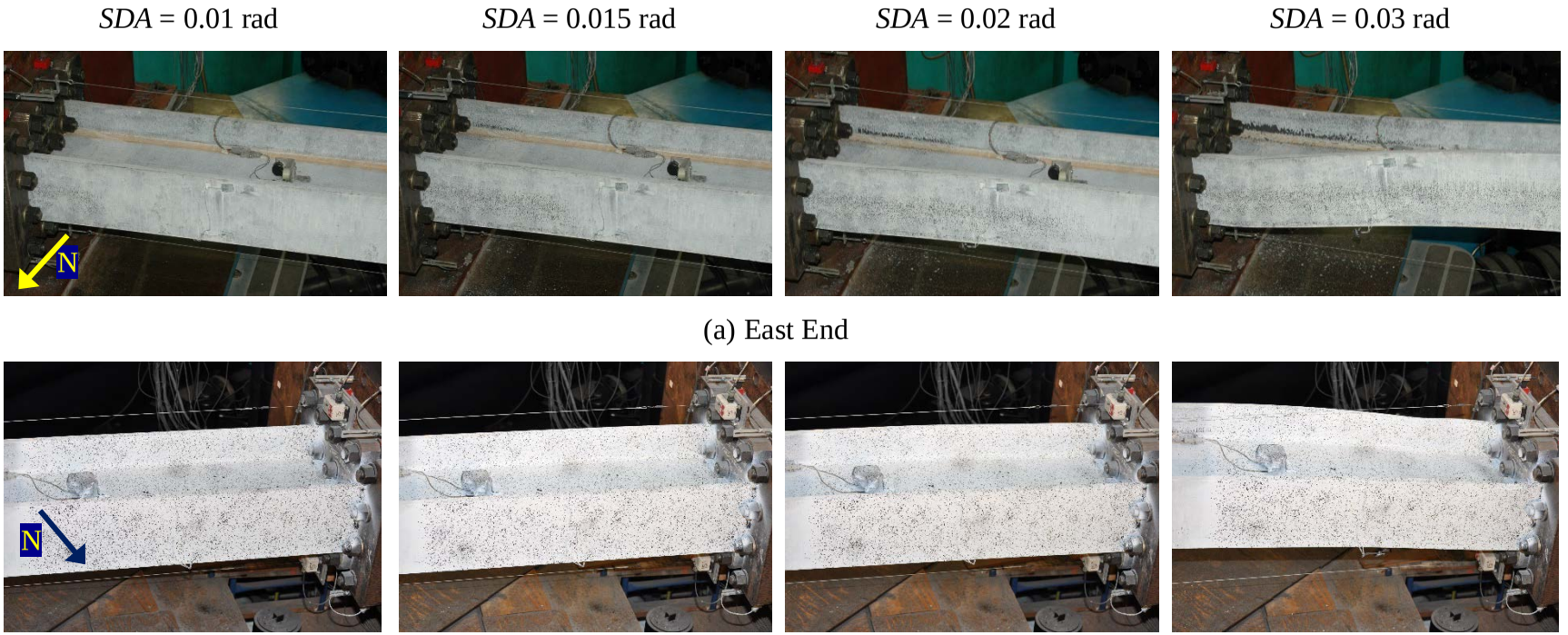

(a) East End

(b) West End

Figure 4.30 Specimen 21M-VAM: Yielding and Buckling Progression at Member Ends

(a) Southwest Flange

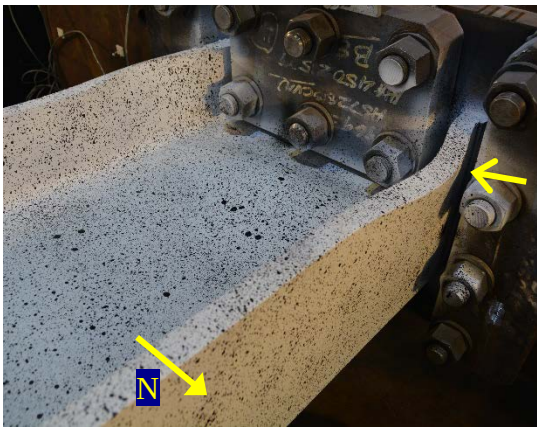

(b) Northwest Flange

(c) Web Local Buckling at West End

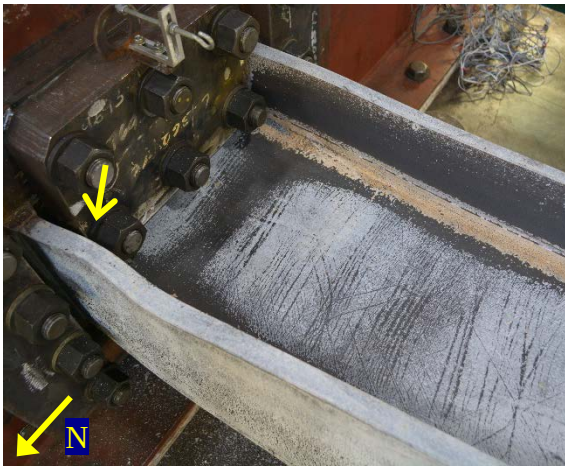

(d) Northeast Flange

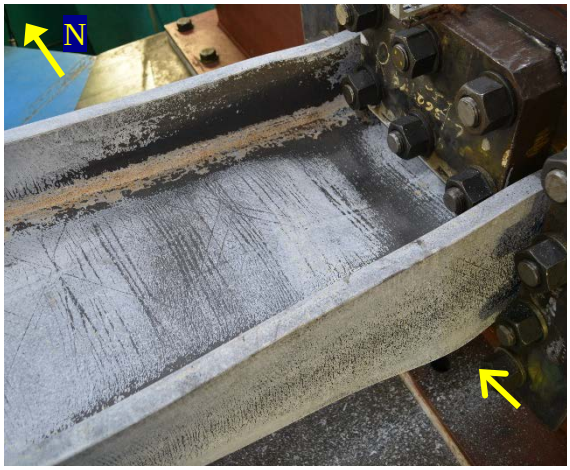

(e) Southeast Flange

Figure 4.31 Specimen 21M-VAM: LTB-induced Local Buckling at End of Test

(a) Overall

(b) East End

Figure 4.32 Specimen 21M-VAM: Significant Twisting at East End

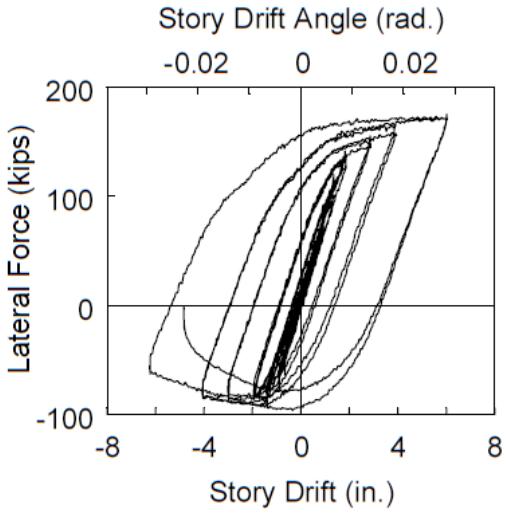

(a) Lateral Force vs. *SDA*

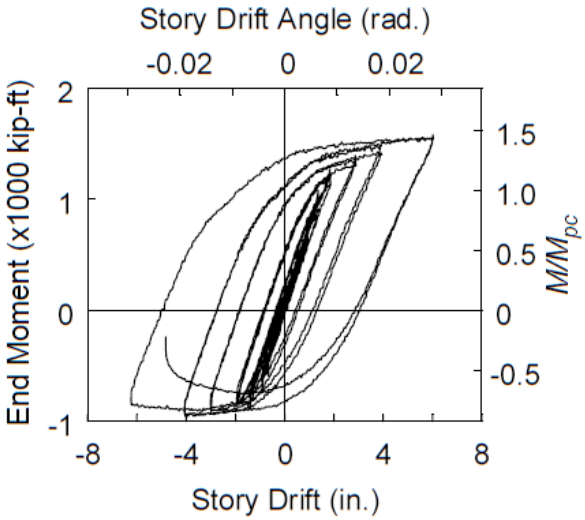

(b) End Moment vs. *SDA*

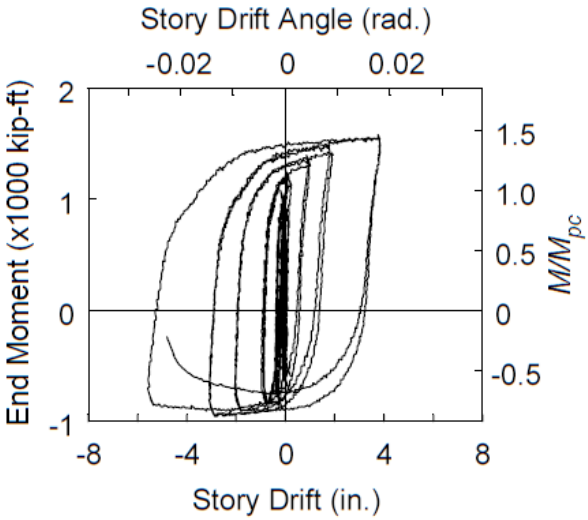

(c) End Moment vs. Plastic *SDA*

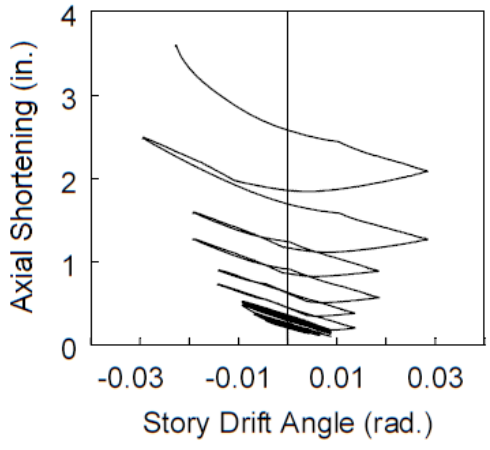

(d) Axial Shortening vs. *SDA*

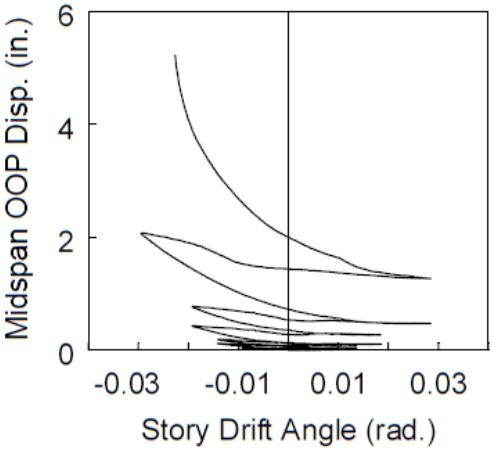

(e) Midspan OOP Disp. vs. *SDA*

Figure 4.33 Specimen 21M-VAM: Global Repsonses

4.5.3 Specimen 21M-VAU

Testing of Specimen 21M-VAM, which had an axial force coefficient C_a varied from 0.1 to 0.7, was stopped after completing two cycles at 3% drift due to excessive global buckling and strength degradation. By varying C_a from -0.2 to 0.4, Specimen 21M-VAU was able to experience one cycle at 5% drift. The governing failure mode of Specimen 21M-VAU is CB with the reverse-curvature global configuration; yielding and buckling progression is shown in Figure 4.34 and Figure 4.35.

LTB of the specimen was triggered during the 4% and 5% drift cycles only in the negative excursions with downward and upward amplitudes at the northeast and southwest flanges, respectively. In the positive excursions, the column sustained axial tension, which stretched it and mitigated the out-of-plane buckling amplitudes as shown in Figure 4.36; the column axial shortening also recovered corresponding to this phenomenon as shown in Figure 4.39(d).

Severe LTB movements were observed during the first negative excursion at 5% drift, at which point the member flexural strength began to degrade considerably as shown in Figure 4.39(b). Out-of-plane and warping stresses associated with the LTB deformation contributed significant tension at the free edges of the column flange CJP welds. In an attempt to displace the specimen to +5% drift with increasing tensile axial load for the second time, a rupture occurred at the northeast flange near the end plate as shown in Figure 4.37; the test was terminated. A partial fracture of a CJP weld was also observed at the top edge of the southwest flange (see Figure 4.38). Indeed, the combined effects of in-plane bending, LTB-type movements, and axial tension were detrimental to CJP welded joints (it will be shown in the next section that a similar flange rupture was also observed in

Specimen 21M-VAU-BC, which also experienced axial tension). Unlike Specimen 21M-VAM that experienced considerable LTB-induced local buckling at the member ends, Specimen 21M-VAU did not experience local buckling although this latter specimen underwent higher drift levels. Partly, this was due to the axial compression applied to the latter (maximum C_a = 0.4) was lower than that applied to the former (maximum C_a = 0.7).

(a) *SDA* = 0.02 rad

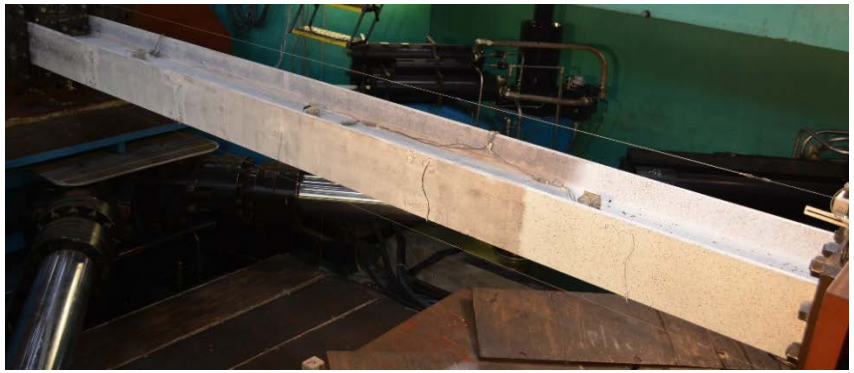

(b) *SDA* = 0.03 rad

(c) *SDA* = 0.04 rad

(d) *SDA* = 0.05 rad

Figure 4.34 Specimen 21M-VAU: Overall Yielding and Buckling Progression

(a) East End

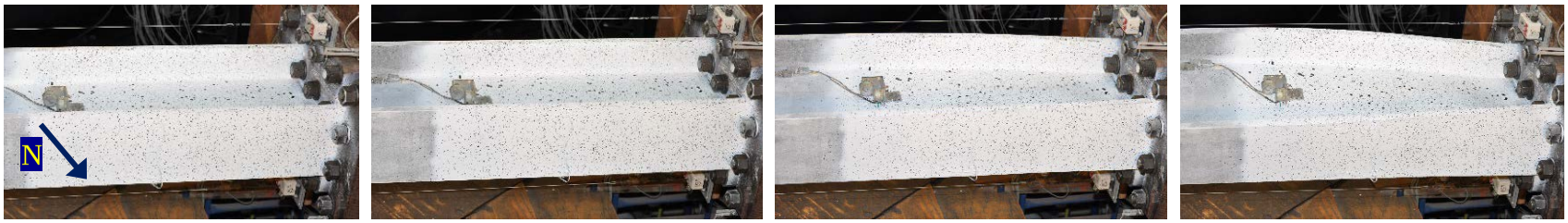

(b) West End

Figure 4.35 Specimen 21M-VAU: Yielding and Buckling Progression at Member Ends

SDA = -0.04 rad (1st Cycle) *SDA* = +0.04 *SDA* (2nd Cycle)

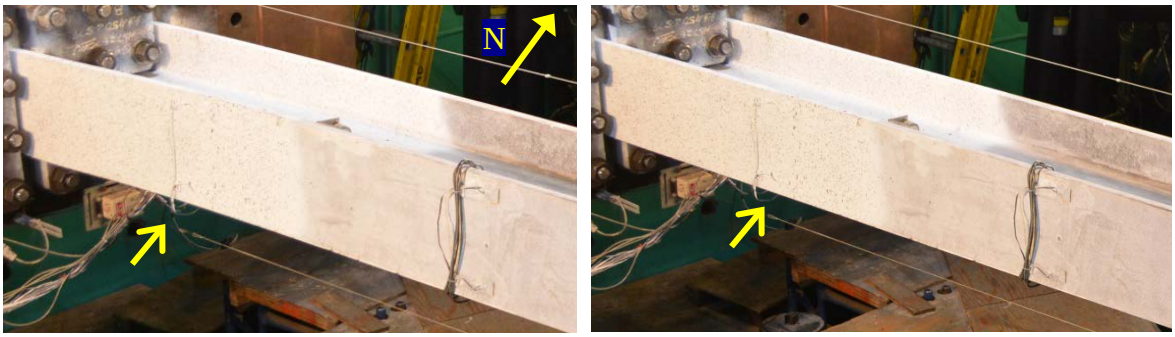

(a) Southwest Flange

(b) Northeast Flange

Figure 4.36 Specimen 21M-VAU: Tensile Axial Load Effect on Out-of-Plane Buckling

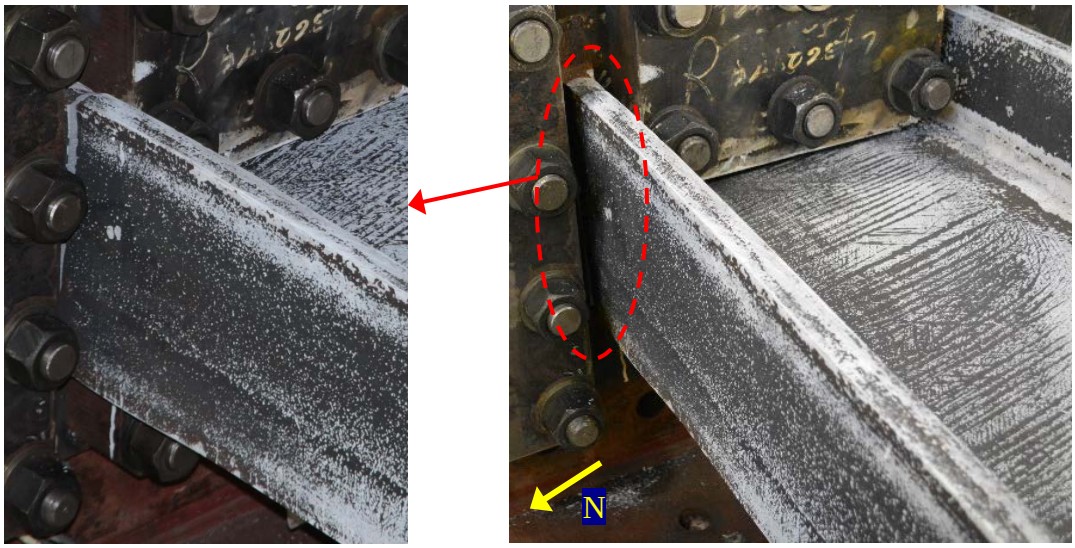

Figure 4.37 Specimen 21M-VAU: Rupture at Northeast Flange

(a) Northeast Flange

(b) Southwest Flange

Figure 4.38 Specimen 21M-VAU: Column Flange CJP Weld Fracture

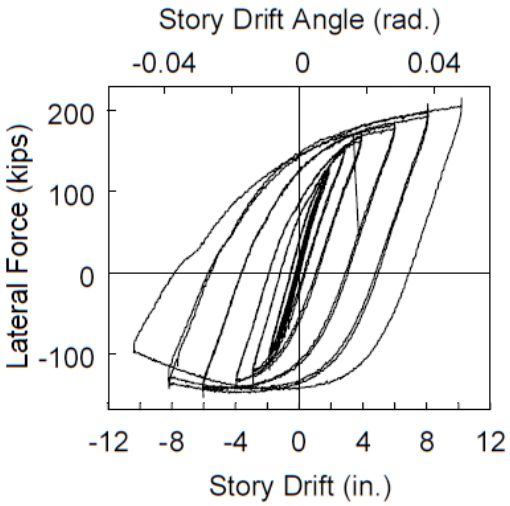

(a) Lateral Force vs. *SDA*

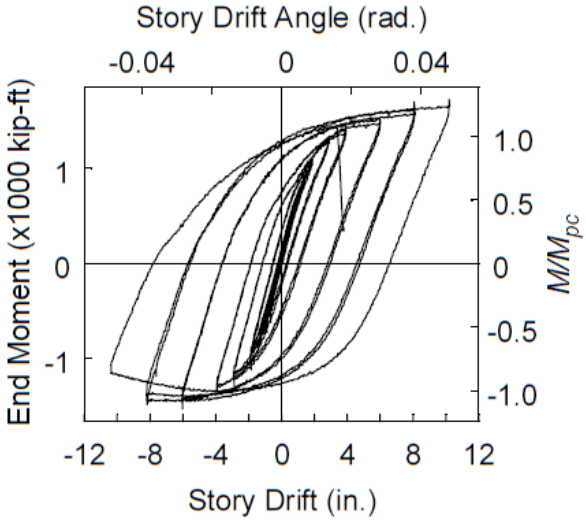

(b) End Moment vs. *SDA*

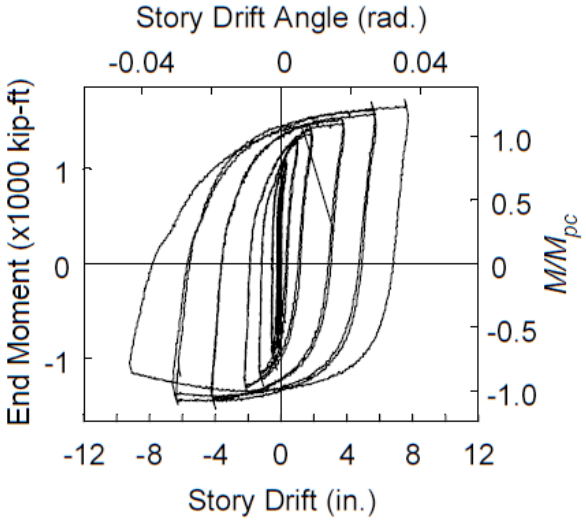

(c) End Moment vs. Plastic *SDA*

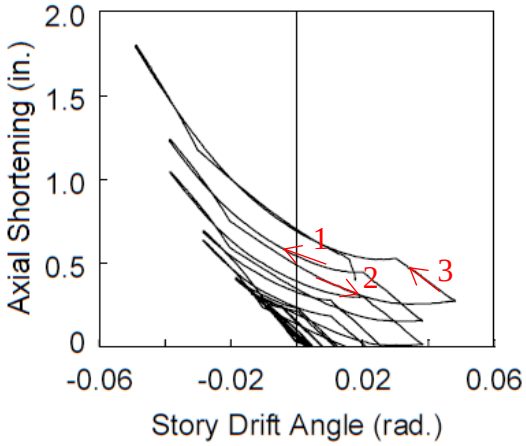

(d) Axial Shortening vs. *SDA*

Figure 4.39 Specimen 21M-VAU: Global Repsonses

4.5.4 Specimen 21M-VAU-BC

Section 2.5 discussed the end rotation sequence utilized in fixed-rotating boundary condition tests; it intended to apply a strong-axis end rotation at the east (or moving) end of the specimen with the same magnitude as the applied story drift angle (i.e., the AISC loading protocol). However, the SRMD platen could only apply approximately 0.035 rad rotation in both the clockwise and counterclockwise directions. Therefore, for 4% and greater drift cycles, the rotation-to-drift ratio ξ defined in Section 2.7 became less than 1 for some portions of the test where the applied story drift angle exceeded 0.035 rad; ξ equaled to 1 anywhere else. Figure 4.40(a) compares the story drift angle and end rotation histories of Specimen 21M-VAU-BC; two horizontal dashed lines indicates the maximum rotation the platen could accommodate during testing. It shows the load steps at which the applied story drift angle exceeded the applied end rotation. The corresponding global response portions are shown in dashed line in Figure 4.40(b); the solid line indicates the portions at which ξ is maintained at 1. The plot shows that lateral stiffness of the former is greater than that of the later when considering each loading and unloading branch of the 4% and greater drift cycles separately; this demonstrated the effect of varying ξ.

With the imposed rotation at the east end, the specimen was able to displace further compared to Specimen 21M-VAU; it completed two cycles at 5% drift and one cycle at 5.5% drift (the platen setup at that time did not allow 6% drift displacement) before the test was terminated. Specimen 21M-VAU only completed one cycle at 5% drift before its northeast flange and CJP weld ruptured.

The governing failure mode of Specimen 21M-VAU-BC is CB with the single-curvature global configuration; yielding and buckling progression is shown in Figure 4.41

and Figure 4.42. LTB behavior of this specimen was similar to that of Specimen 21M-VAU except that (1) the east end remained essentially in the elastic range up to 3% drift (see Figure 4.42) and did not exhibit obvious LTB movements until 5% drift, and (2) CJP weld ruptured at the southwest flange as shown in Figure 4.43. A minor LTB-induced flange local buckling was observed at the top half-width southwest flange, which was accompanied by a minor web local buckling due to the influence of web-flange interactions as shown in Figure 4.44.

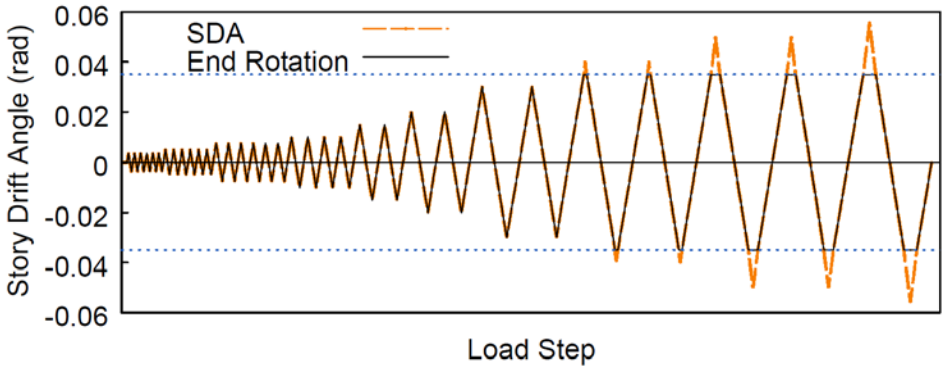

(a) Story Drift Angle and End Rotation (at Moving End) History Comparison

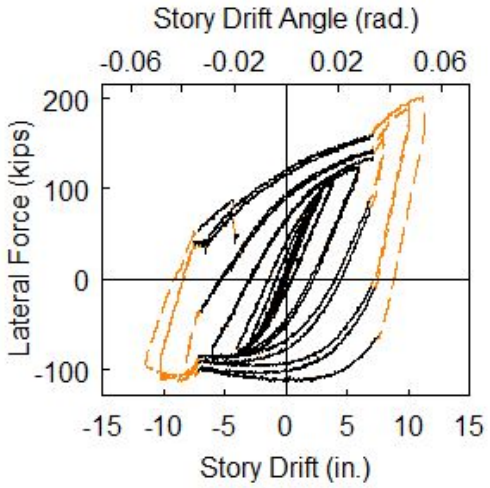

(b) Lateral Force vs. *SDA*

Figure 4.40 Specimen 21M-VAU-BC: End Rotation History and the Corresponding Global Response

(a) *SDA* = 0.03 rad

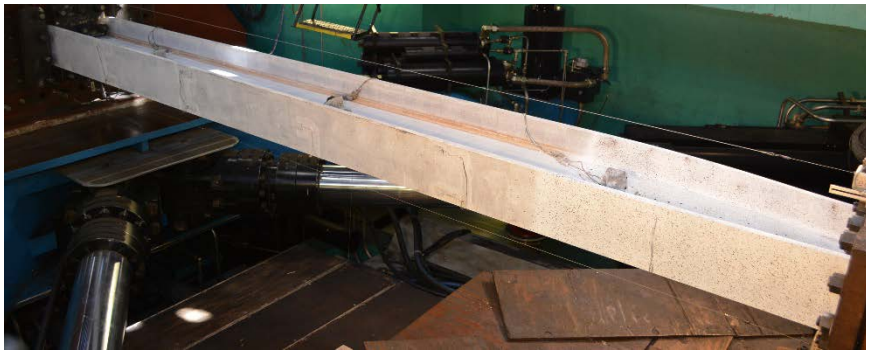

(b) *SDA* = 0.04 rad

(c) *SDA* = 0.05 rad

(d) *SDA* = 0.055 rad

Figure 4.41 Specimen 21M-VAU-BC: Overall Yielding and Buckling Progression

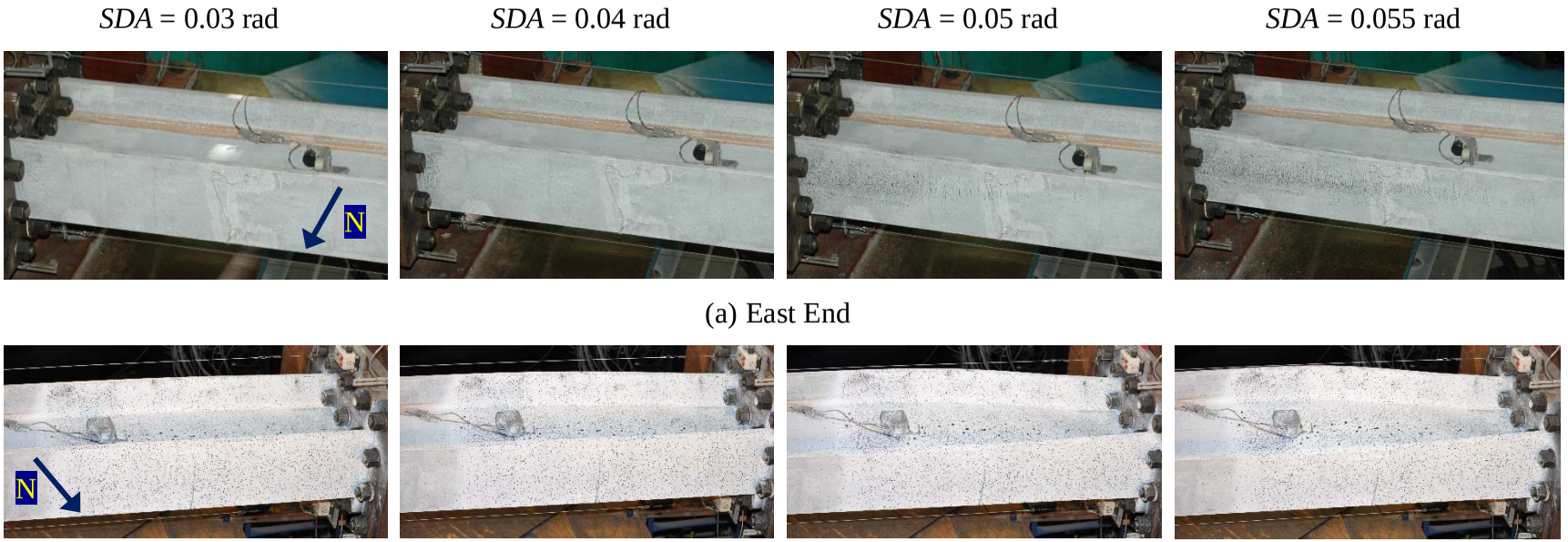

(a) East End

(b) West End

Figure 4.42 Specimen 21M-VAU-BC: Yielding and Buckling Progression at Member Ends

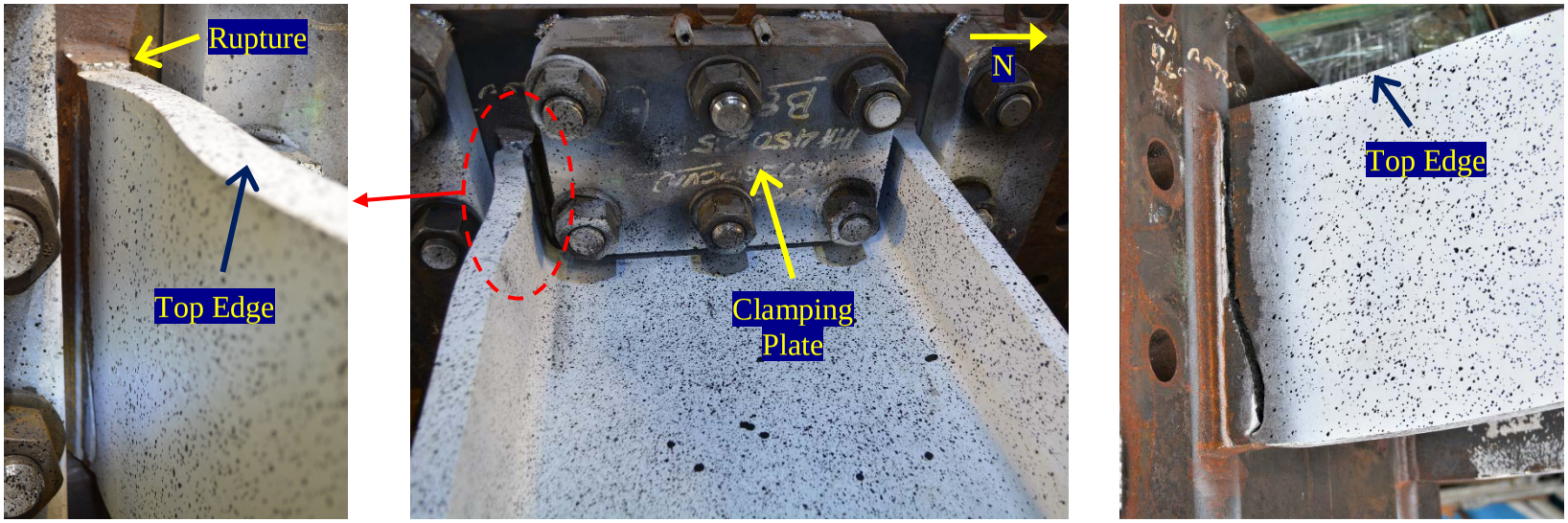

(a) *SDA* = 0.055 rad (b) after Test Inspection

Figure 4.43 Specimen 21M-VAU-BC: Rupture at Southwest Flange

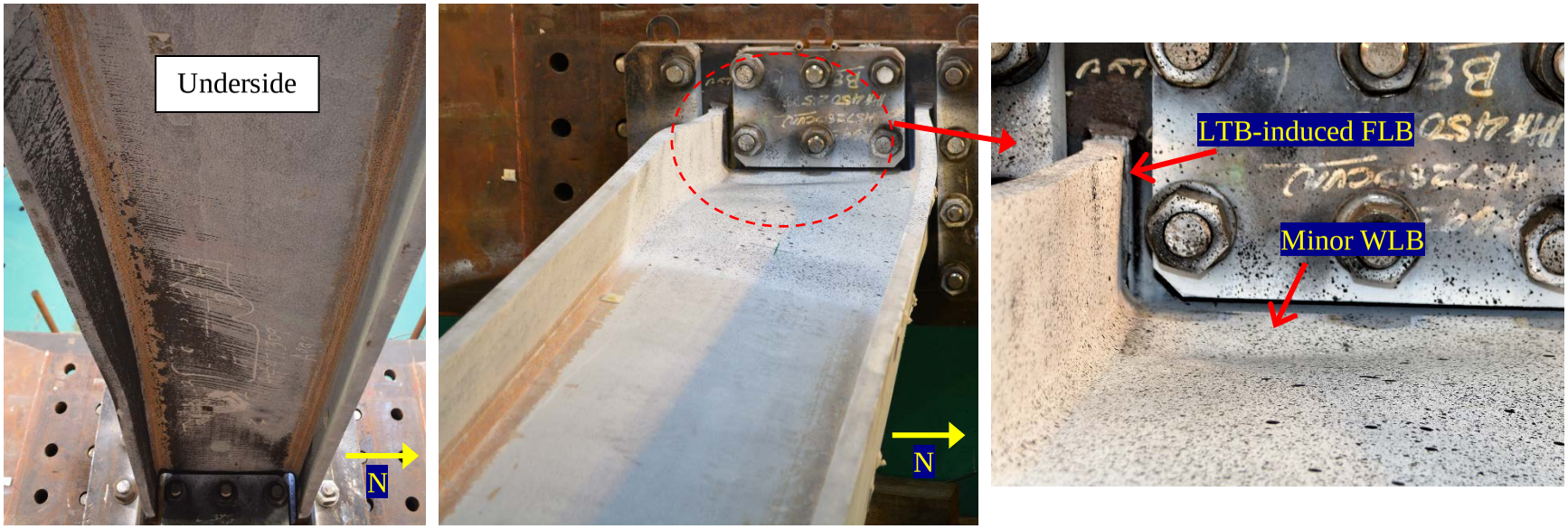

Figure 4.44 Specimen 21M-VAU-BC: Web Deformation at End of Test (West End)

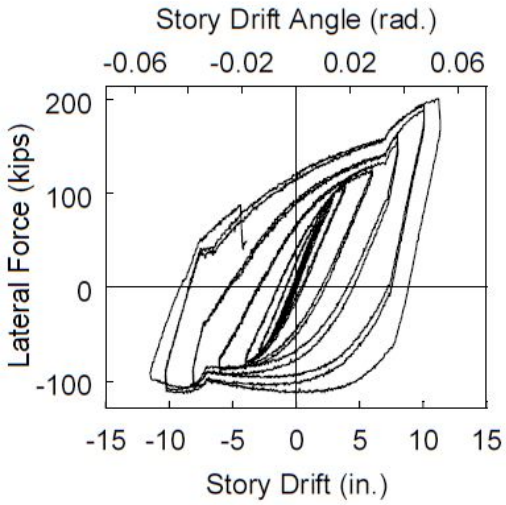

(a) Lateral Force vs. *SDA*

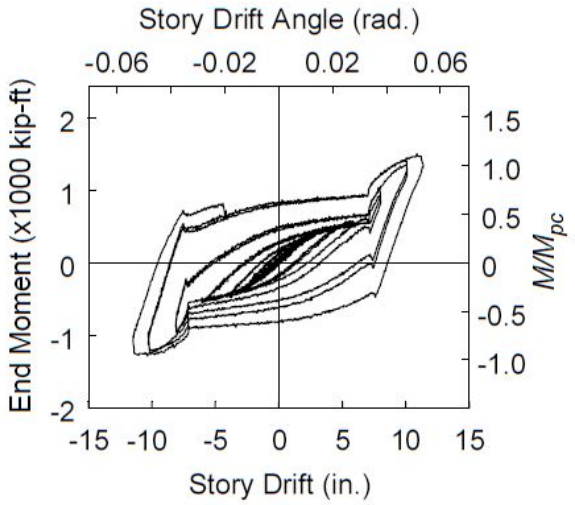

(b) East End Moment vs. *SDA*

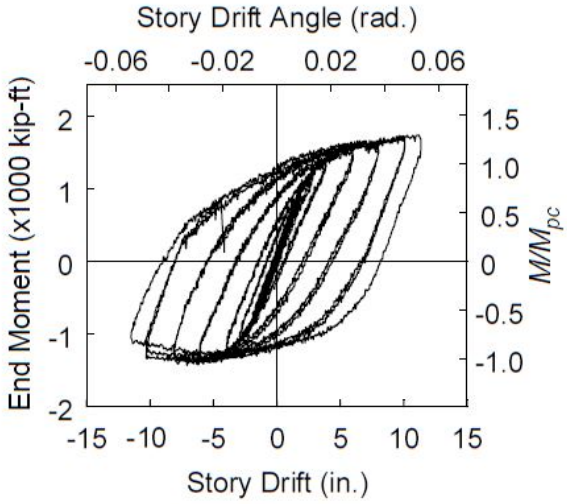

(c) West End Moment vs. *SDA*

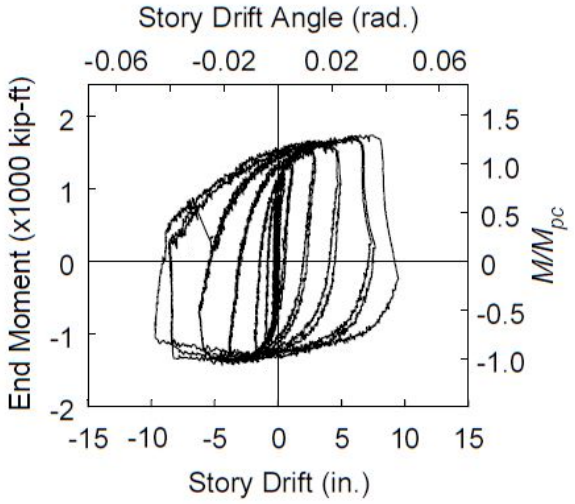

(d) West End Moment vs. Plastic *SDA*

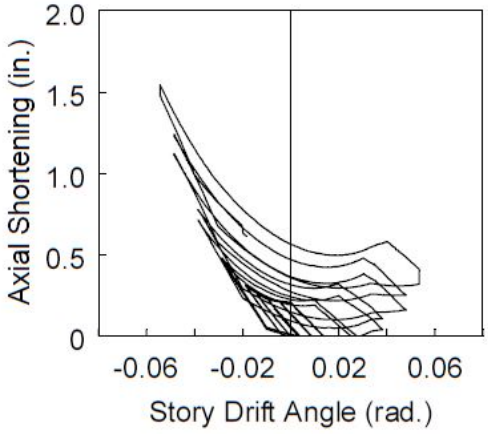

(e) Axial Shortening vs. *SDA*

Figure 4.45 Specimen 21M-VAU-BC: Global Repsonses

4.5.5 Specimen 21M-NF

Figure 4.46(a) shows the near-fault loading protocol, which is characterized by its large initial pulse and the following, smaller drift cycles that oscillate about a level of residual drift. The specimen underwent all these cycles but did not exhibit significant damage. Thus, after this "first run," the same loading protocol was applied from the 4% residual drift as shown in Figure 4.46(b); the "second run" refers to this portion of the test. Although the specimen was subjected to a constant level of axial load, it underwent asymmetric lateral drift loading: except for the first negative drift peak in the combined near-fault loading protocol, all cycles were in a positive drift range.

Figure 4.47 illustrates the overall yielding and buckling progression. At the first -2% drift, the specimen already experienced plastic deformation. In the following positive excursion to +6% drift, LTB of the specimen initiated with upward and downward amplitudes at the northwest and southeast flanges (i.e., compression flanges in positive drift), respectively. Since plastic deformation had already established, the southwest and northeast flanges (i.e., compression flanges in negative drift) experienced in-plane flexural compression in the following negative excursion to +1% drift, even though the specimen was not displaced into the negative drift range; Figure 4.48(a) shows the corresponding expansion of flaking. LTB of the specimen aggravated slightly but less aggressive than that observed during the former positive excursion. For the remaining first run cycles, LTB exacerbated more in the positive excursions than in the negative excursions, demonstrating the effect of the asymmetrical lateral drift loading. Figure 4.52(b) shows a slight flexural strength degradation in the positive excursions but not in the negative excursions of the first run.

In the positive excursion to +10% drift during the second run, LTB of the specimen aggravated drastically with significant out-of-plane amplitudes at the compression flanges in the positive drift as shown in Figure 4.47(b) and Figure 4.49. This led to a drastic flexural strength degradation as shown in Figure 4.52(b). Like the first run, LTB exacerbated in the positive excursions; unlike the first run, it appeared that LTB amplitudes recovered somewhat during the negative excursions. Since axial shortening grew proportionally to the out-of-plane amplitudes, it also recovered somewhat in the negative excursions as shown in Figure 4.52(d). Again, only the flexural strength in the positive excursions degraded while that in the negative excursions remained relatively stable because of the asymmetrical lateral drift loading. The test was terminated due to excessive reduction in lateral force resistance.

LTB-induced flange local buckling configurations of this specimen were like those of Specimen 21M-VAM as shown in Figure 4.50; those at the west end appeared to be triggered primarily by out-of-plane stresses while those at the east end later appeared to be induced primarily by warping stresses due to significant twisting at the east end as shown in Figure 4.51. Influenced by web-flange interactions, the web at each end also buckled locally in the direction that conformed to the flange local buckling configurations.

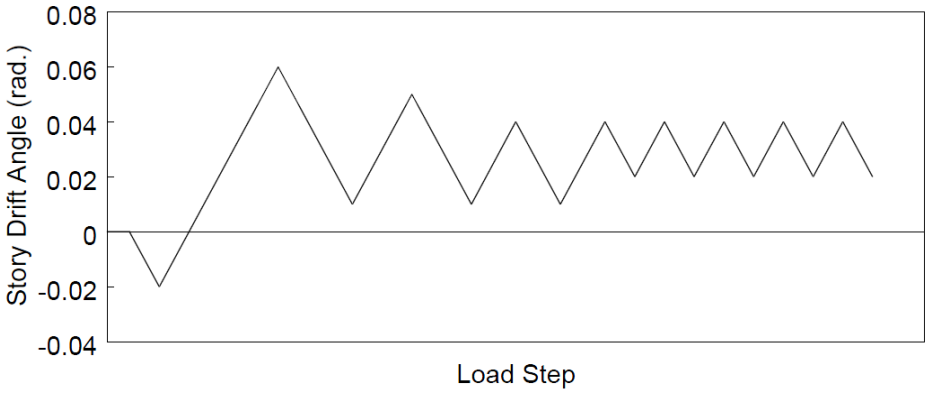

(a) Near-fault Loading Protocol

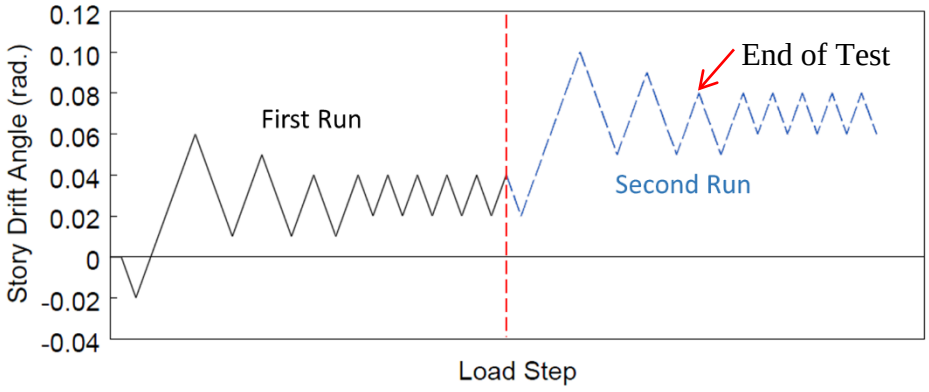

(b) Combined Near-fault Loading Protocol

Figure 4.46 Specimen 21M-NF: Near-fault Loading Protocols

SDA = -0.02 rad

SDA = +0.06 rad

SDA = +0.01 rad

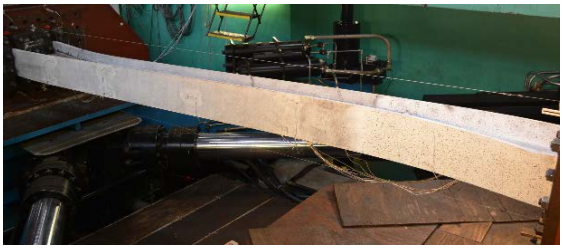

SDA = +0.05 rad

(a) First Run

SDA = +0.02 rad

SDA = +0.10 rad

SDA = +0.05 rad

End of Test

(b) Second Run

Figure 4.47 Specimen 21M-NF: Overall Yielding and Buckling Progression

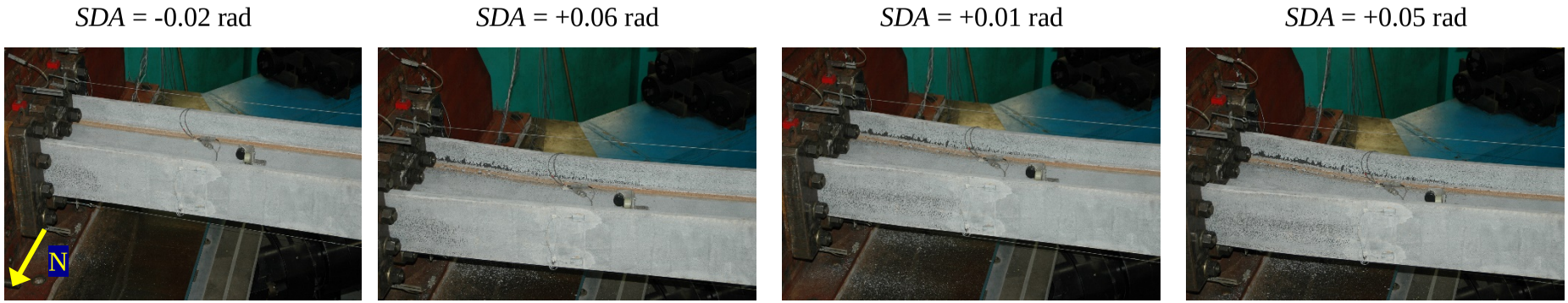

(a) East End

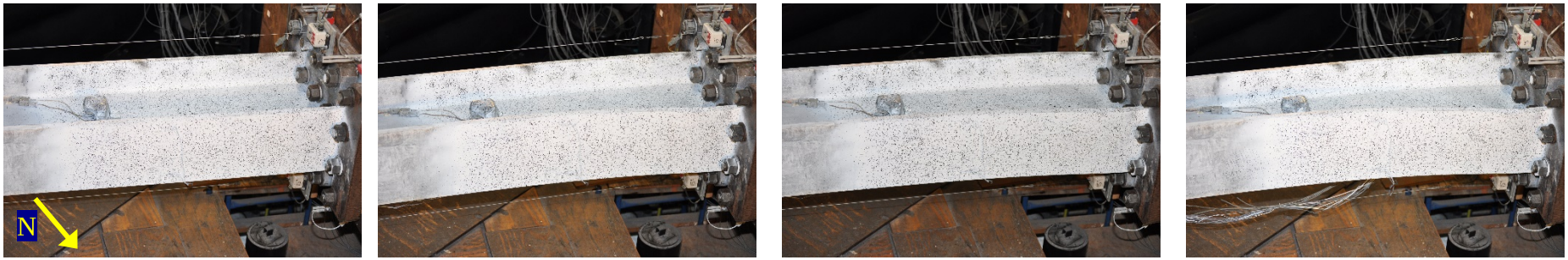

(b) West End

Figure 4.48 Specimen 21M-NF: Yielding and Buckling Progression at Member Ends (Fisrt Run)

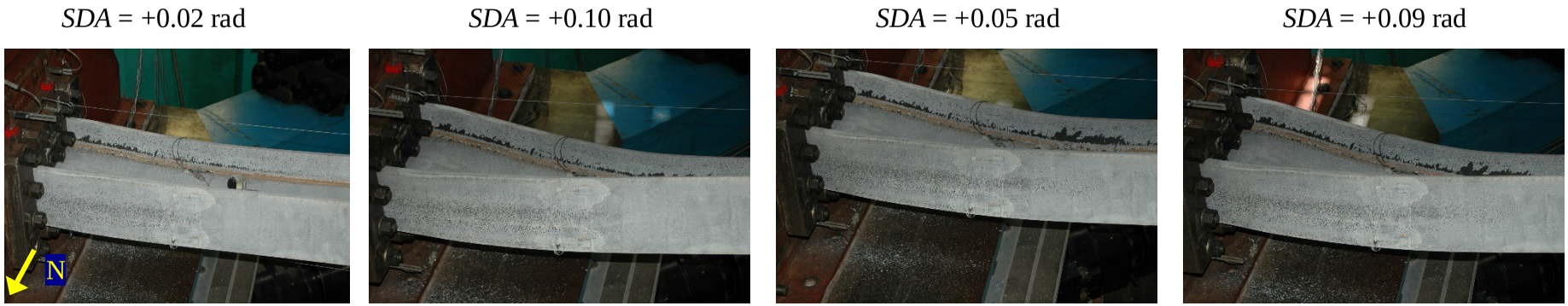

(a) East End

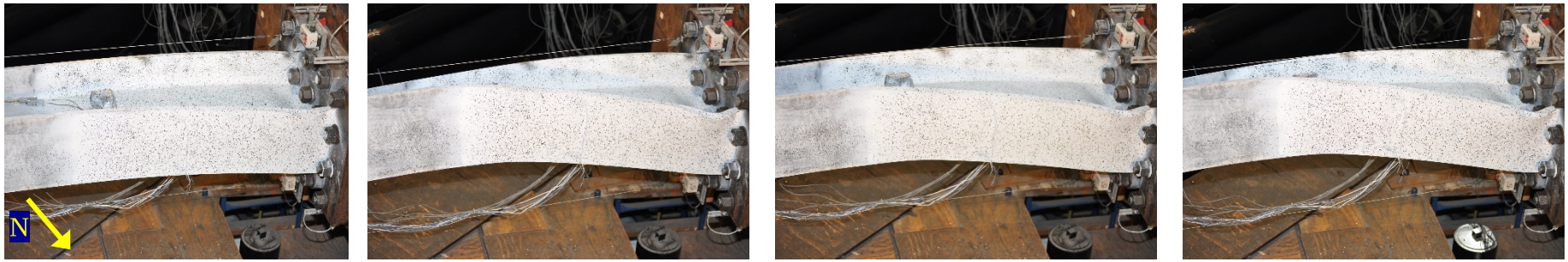

(b) West End

Figure 4.49 Specimen 21M-NF: Yielding and Buckling Progression at Member Ends (Second Run)

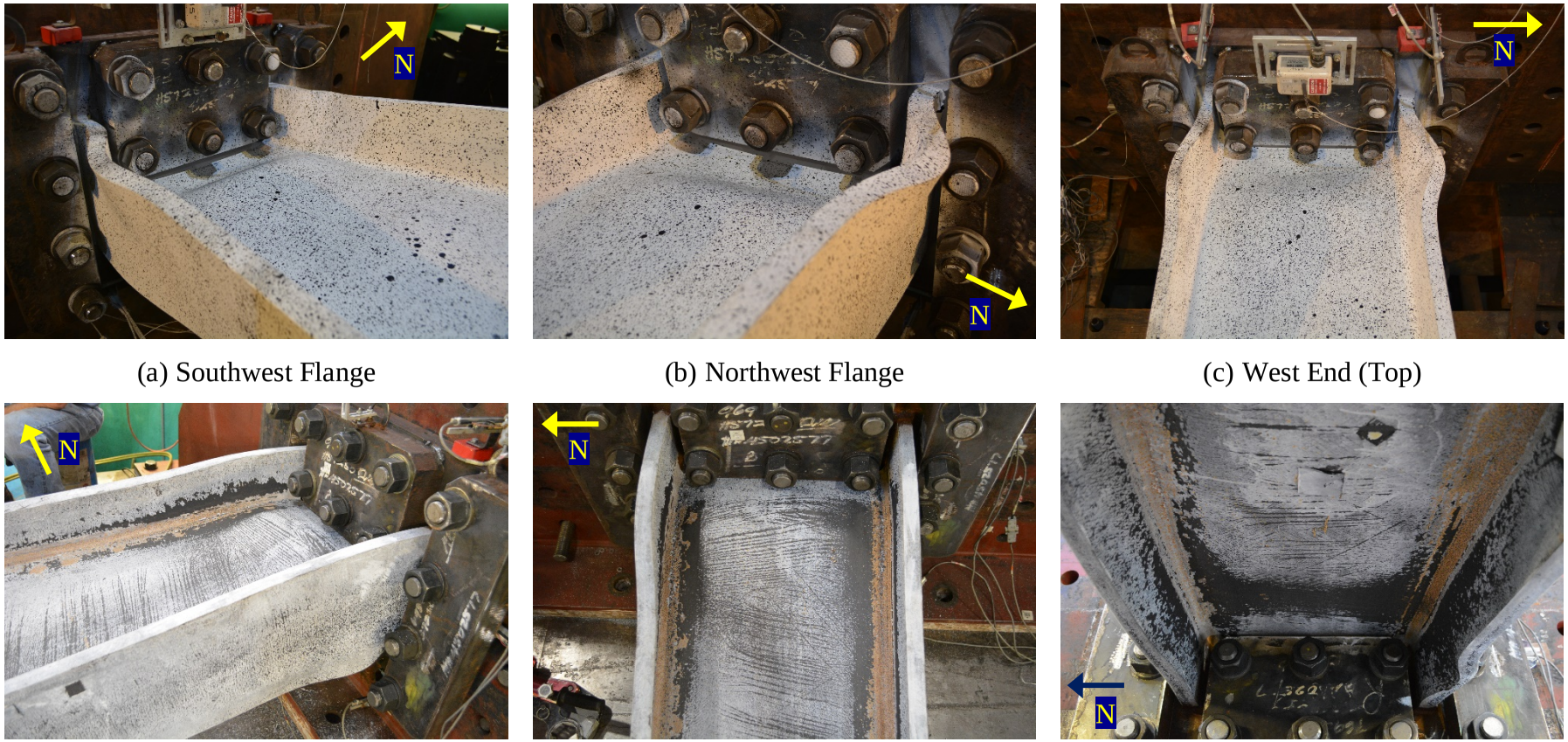

(a) Southwest Flange (b) Northwest Flange (c) West End (Top)

(d) Southeast Flange (e) East End (Top) (f) East End (Bottom)

Figure 4.50 Specimen 21M-NF: LTB-induced Local Buckling at End of Test

Figure 4.51 Specimen 21M-NF: Significant Twisting at East End

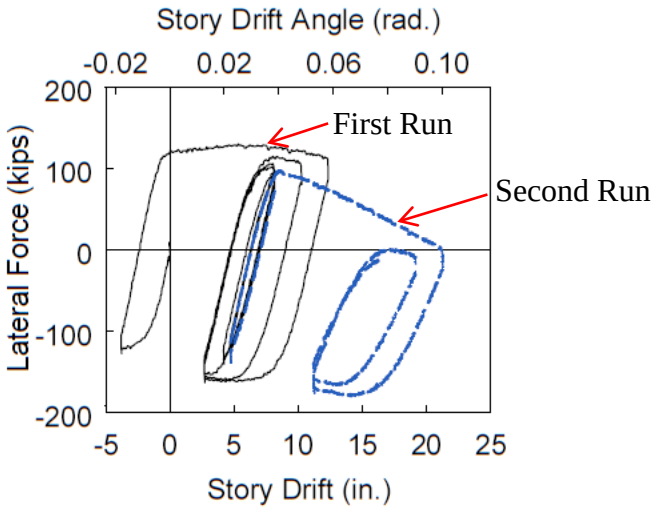

(a) Lateral Force vs. *SDA*

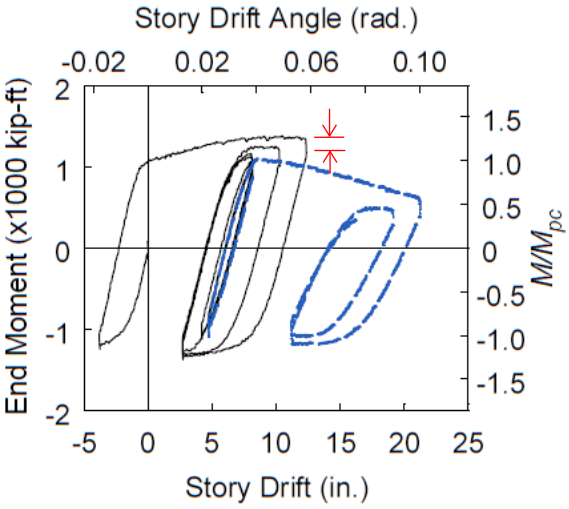

(b) End Moment vs. *SDA*

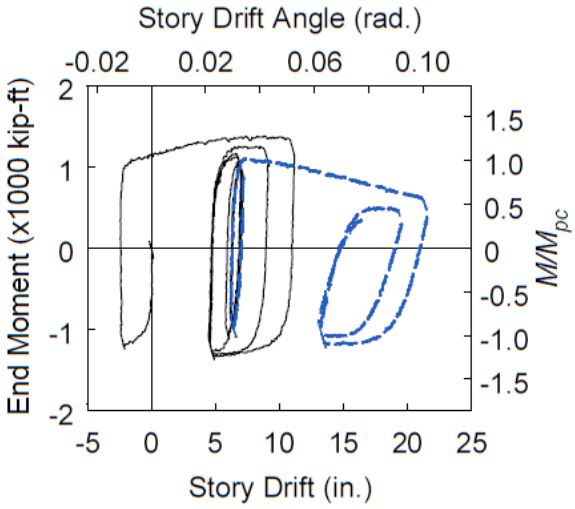

(c) End Moment vs. Plastic *SDA*

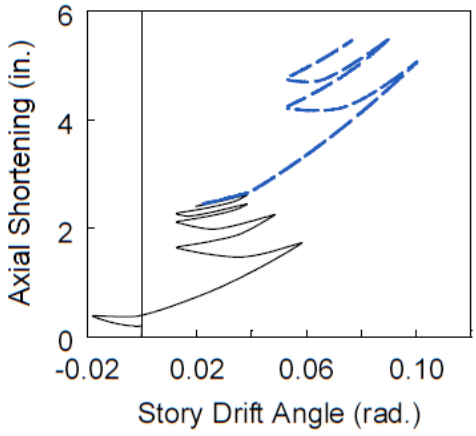

(d) Axial Shortening vs. *SDA*

Figure 4.52 Specimen 21M-NF: Global Repsonses

4.5.6 Concluding Remarks

Column end moment and axial shortening responses of all W18×130 specimens tested in Phase 2 are shown in Figure 4.53 and Figure 4.54, respectively, with consistent range in the horizontal and vertical axes. Comparisons can be made as follows:

(1) Flexural strengths of Specimens 16M and 16M-BC are similar in magnitude since the two specimens sustain the same level of axial compression ($C_a = 0.4$). Specimen 21M-VAM experiences varying axial compression with C_a ranging from 0.1 in the positive excursions to 0.7 in the negative excursions. This causes its end moment response to be asymmetrical with higher and lower flexural strength relative to those of the former specimens in the positive and negative excursions respectively.

(2) Specimens 21M-VAU and 21M-VAU-BC exhibit increased flexural and ductility capacities as their axial load range is offset from $C_a = 0.1$ to 0.7 to C_a = -0.2 to 0.4. Their end moment responses are also less asymmetrical compared to that of Specimen 21M-VAM because they sustain axial tension and compression that are relatively close in magnitude (0.2 and 0.4). For Specimen 21M-VAM, the magnitudes of the lowest and highest compression (0.1 and 0.7) are much more different.

(3) While flexural strength degradation is observed in both the positive and negative excursions for constant axial load tests, it is only observed in the negative excursions for varying axial load tests.

(4) Specimens 16M-BC and 21M-VAU-BC with fixed-rotating boundary conditions exhibit lower elastic flexural stiffness than that of their counterparts with fixed-fixed boundary conditions, i.e., Specimens 16M and 21M-VAU respectively. The former

also sustains a higher drift level than the latter before significant strength degradation or a column flange CJP weld rupture occurs.

(5) Specimen 21M-NF with the near-fault loading protocol exhibits a relatively stable end moment response compared to others despite being pushed to 6% drift during the first run test (see Section 4.5.5).

(6) Specimens 16M, 16M-BC, and 21M-VAM experience LTB movements at 2%, 3%, and 2% drifts, respectively. Their axial shortening is relatively limited before the onset of LTB. Such grows at an increasing rate proportional to the out-of-plane amplitude once LTB initiates. All three specimens exhibit similar out-of-plane amplitudes when their flexural strengths degrade significantly, prompting termination of the tests. As a result, they exhibit relatively similar level of axial shorting (roughly 4 to 5 in.) at the end of the tests.

(7) With a varying axial load that oscillates below the medium level (i.e., $C_a \leq 0.4$), Specimens 21M-VAU and 21M-VAU-BC exhibit significantly less axial shortening compared to others. This is because their LTB movements are not triggered until 4% drift and do not exacerbate much before the specimens experience column flange CJP weld ruptures.

(8) In constant axial compression tests, axial shortening remains constant and exacerbates during each in-plane flexural unloading and reloading branch, respectively. In contrast, that of varying axial load tests recovers (i.e., reduces in magnitude) in the positive excursions due to the simultaneous reduction of axial and in-plane flexural compression; it then aggravated in the negative excursions, corresponding to when axial load progressively returns to its highest compressive level.

Chapter 2, 3, 4, and 5 in part are currently being prepared for submission for publication of the material. Chansuk, P., Ozkula, G., and Uang, C.-M. (2018). “ATC-106 Phase 2: Seismic behavior and design of deep, slender wide-flange structural steel beam-columns.” *Report No. SSRP-18/02*, University of California, San Diego, La Jolla, CA. The thesis author was the primary investigator and author of this material.

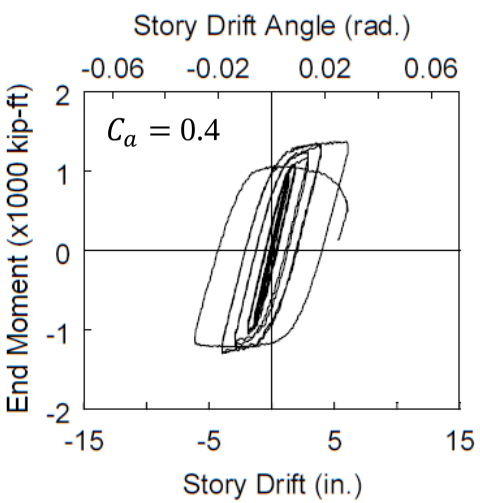

(a) Specimen 16M

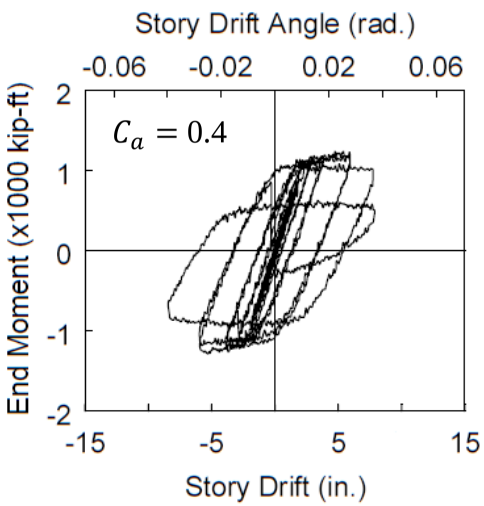

(b) Specimen 16M-BC

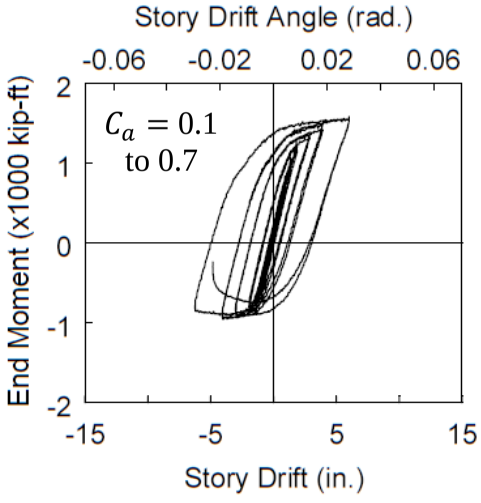

(c) Specimen 21M-VAM

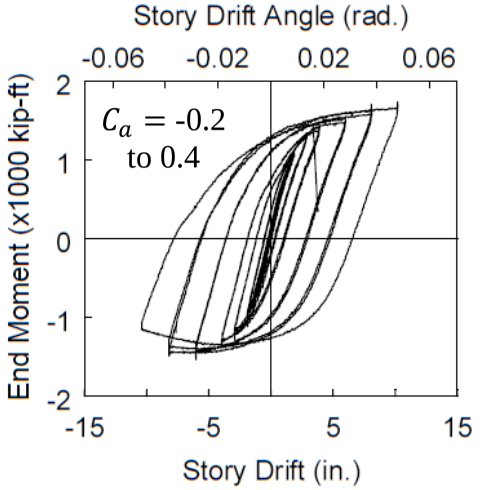

(d) Specimen 21M-VAU

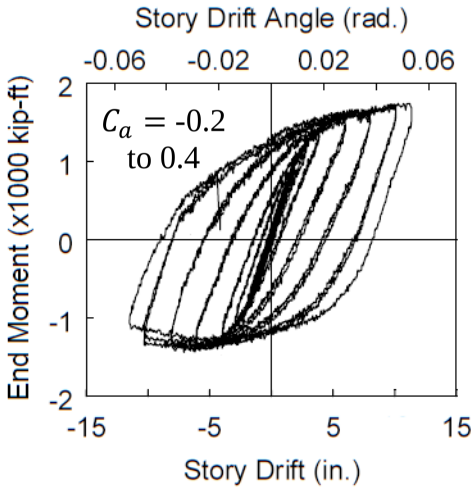

(e) Specimen 21M-VAU-BC

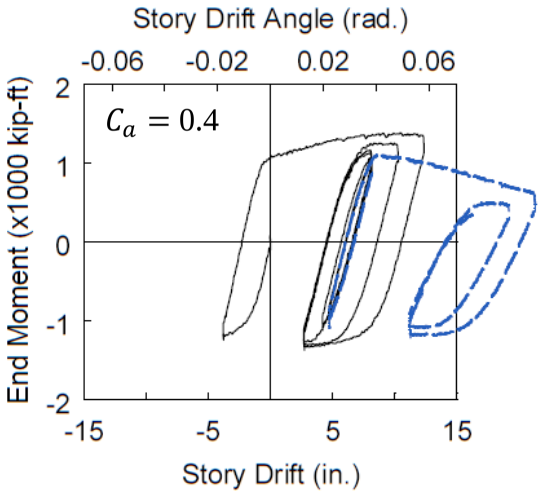

(f) Specimen 21M-NF

Figure 4.53 W18×130 Specimens: West End Moment Repsonse

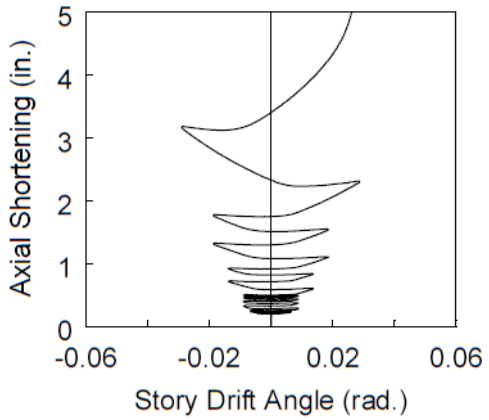

(a) Specimen 16M

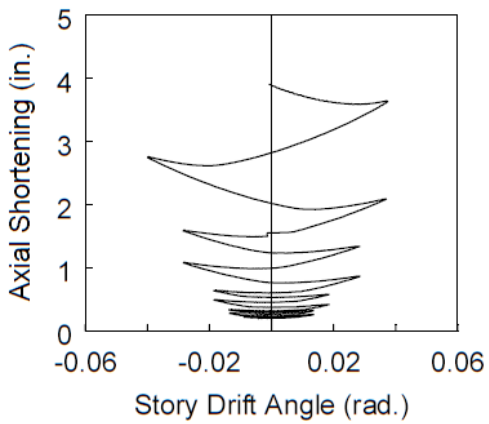

(b) Specimen 16M-BC

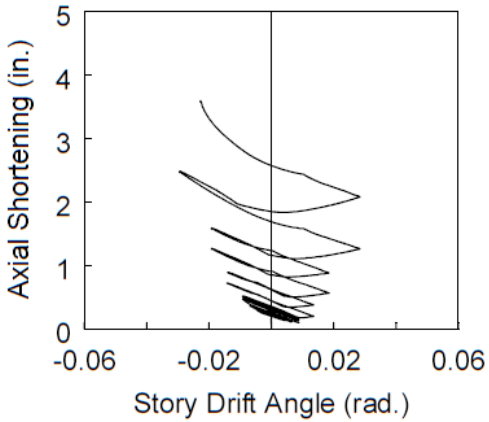

(c) Specimen 21M-VAM

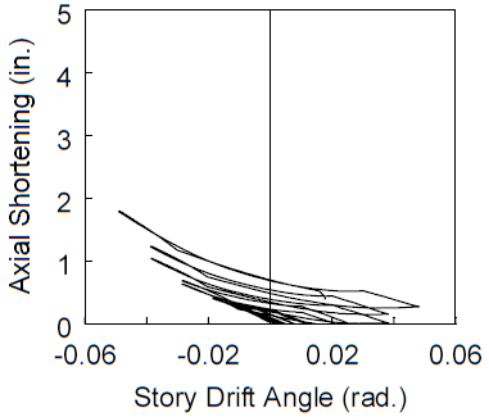

(d) Specimen 21M-VAU

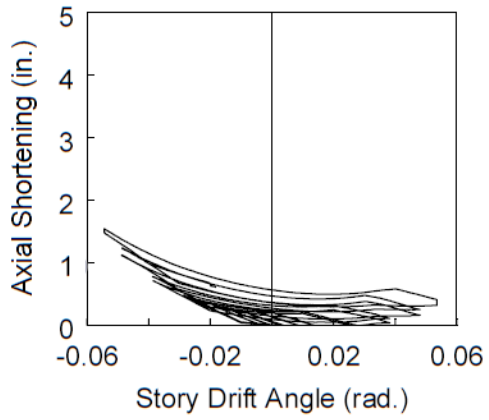

(e) Specimen 21M-VAU-BC

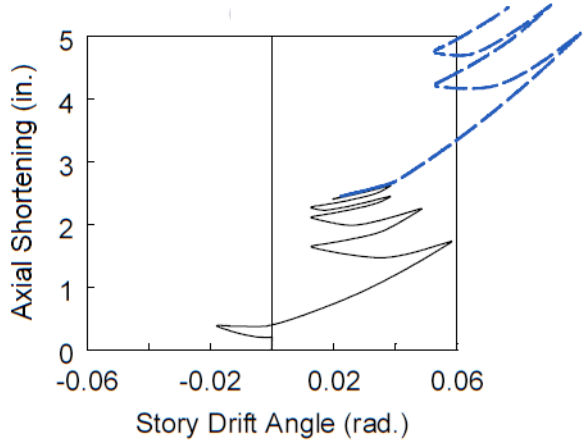

(f) Specimen 21M-NF

Figure 4.54 W18×130 Specimens: Axial Shortening Repsonse

5. BOUNDARY CONDITION EFFECT

5.1 Introduction

In real application, the top end of first-story columns in a moment frame experiences rotation due to the flexibility of the connected beams, i.e., the columns sustain fixed-rotating boundary conditions. Accordingly, in NIST Phase 2 testing, four specimens (Specimens 11H-BC, 13M-BC, 16M-BC, and 21M-VAU-BC) were cyclically tested with the fixed-rotating boundary conditions (see Section 2.6.3 for loading protocols): a cyclic end rotation in-phase with and proportional to the applied cyclic lateral drift was prescribed to the east or moving end, which can be expressed as follows:

$$\theta = \xi \left(\frac{\Delta_m}{L} \right) \tag{5.1}$$

where ξ is the rotation-to-drift ratio and is set equal to 1 for Specimens 13M-BC, 16M-BC, and 21M-VAU-BC, and 1.1 for Specimen 11H-BC.

Based on the test results and finite element simulations, the effect of boundary conditions on column responses was studied. In addition, a procedure to adjust fixed-fixed column responses to account for this top-end rotation effect is proposed in this chapter.

5.2 Fixed-fixed vs. Fixed-rotating Column Responses

This section investigates the boundary condition effect by comparing the test responses of nominally identical specimens with fixed-fixed and fixed-rotating boundary conditions, respectively; the pairs of Specimens 11H and 11H-BC, Specimens 13M and 13M-BC, and Specimens 16M and 16M-BC with constant axial loads were considered. Finite element models of these specimens were also analyzed to support the experimental findings.

For fixed-fixed columns, the inflection point was assumed to remain at the column midspan throughout the tests; thus, the end moment hysteresis was identical at both ends that underwent significant plastic deformation. For fixed-rotating columns, the rotating end stayed mostly in the elastic range; significant plastic hinging only occurred at the fixed end. Therefore, the *fixed-end moment* responses of the two respective cases were considered to study the boundary condition effects on the column maximum flexural strengths, plastic rotation capacities, strength degradation behaviors, etc. Furthermore, to facilitate the test response comparisons, backbone curves were constructed for the lateral force and fixed-end moment responses of each column as shown in Figure 5.1; it was accomplished by connecting each data point at the peak drift (both positive and negative) of the first cycle of each drift level (ASCE 2013).

The backbone curve comparison of each specimen pair is shown in Figure 5.2. In general, each backbone curve can be characterized into three zones: (1) the elastic zone, (2) the inelastic zone up to the peak flexural strength, and (3) the strength degradation zone. Figure 5.3 color-codes each corresponding zone for both the fixed-fixed and fixed-rotating backbone curves associated with the ALB and CB failure modes. With respect to the fixed-fixed backbone curve, the gray, green, and unshaded regions represent the elastic, inelastic, and degradation zones, respectively; theses were represented by the red, yellow, and unshaded regions for the fixed-rotating backbone curves. Mechanism of the boundary condition effect is discussed below with respect to each zone.

In the elastic zone, the fixed-fixed columns experienced more flexural bending demand than the fixed-rotating columns at the same drift level because the bending curvatures in the latter was relieved somewhat by the rotation at its rotating end.

Essentially, elastic flexural stiffnesses decreased as the result of the end rotation: the latter exhibited lower elastic stiffness than the former. This trend was more prominent in the lateral force responses (see Figure 5.2). Due to the reduction in flexural demand, the latter was also able to undergo a higher drift level before it experienced substantial yielding and entered the inelastic zone. Nonetheless, both the former and the latter exhibited similar flexural yield strengths since they had the same sectional properties, and strain hardening was minimal during the elastic cycles.

In the inelastic zone, fixed-rotating boundary conditions had different effects on specimens with the ALB and CB failure modes. For ALB specimens, flange and web local buckling initiated shortly after small portions of the column ends became fully plastic and softened in material (i.e., the Young's modulus decreased). Accordingly, not many inelastic drift cycles beyond the elastic zone were required to set this condition prone to local instability. This was true for both the fixed-fixed and fixed-rotating columns, even though the latter experienced somewhat less moment demand per additional lateral drifts than the former as the result of the end rotation. Indeed, as shown in Figure 5.3(a), the inelastic zones of the former (green region) and the latter (yellow region) were both limited, i.e., both columns sustained similar limited amount of inelastic cycles beyond their respective elastic cycles before experiencing local buckling. Consequently, they also developed similar extent of strain hardening, which was limited, and thus exhibited similar peak flexural strengths that could be approximated by the reduced plastic moment capacity, M_{pc}, of the section.

Specimens with the CB failure mode, however, usually sustained more inelastic drift cycles than the ALB specimens before they experienced global and local buckling. As

a result, their inelastic zones were much larger than those of the latter as shown in Figure 5.3, i.e., the green and yellow regions in Figure 5.3(b) are much larger than those in Figure 5.3(a). Since they underwent significant lateral drifts beyond the elastic zone, the effect of the rotating end became apparent as shown in Figure 5.3(b): the yellow region was much wider than the green region. That is, the fixed-rotating column could undergo a larger lateral drift beyond the elastic zone than the fixed-fixed column before global and local buckling initiated and trigger flexural strength degradation. Essentially, inelastic flexural stiffnesses also decreased as the result of the end rotation, i.e., it reduced the end moment demand per an additional drift in the fixed-rotating column, which allowed the column to sustain a larger drift level before buckling.

Despite this difference in the lateral drift range, both the fixed-fixed and fixed-rotating CB columns exhibited similar peak flexural strengths. This implies that they experienced similar extent of strain hardening before global instability exacerbated. To verify this observation, finite element analysis of Specimen 16M and 16M-BC was conducted. As an indirect measure of the extent of strain hardening, the cumulative energy dissipation as the result of plastic straining is plotted against the story drift angle for each specimen as shown in Figure 5.4. The horizontal lines indicate the energy levels at which each respective specimen reached its peak flexural strength before global buckling initiated; both are very close. Accordingly, this signifies that the two columns, indeed, underwent similar extent of strain hardening before they buckled out-of-plane and, hence, exhibited similar peak flexural strengths. This trend was also confirmed with other fixed-fixed and fixed-rotating CB specimen pairs (results not shown).

Further investigation revealed that the fixed-rotating CB columns exhibited a slightly lower peak flexural strength than the fixed-fixed CB columns. Since lateral-torsional buckling (LTB) was the important limit state that influenced the peak flexural strengths of these CB columns under cyclic loading, the elastic LTB design principle could be used to understand the boundary condition effect on the peak strengths. AISC 360 (AISC 2016c) used C_b, the lateral-torsional buckling modification factor, in determining the nominal flexural strength of flexural members with nonuniform moment diagrams. For doubly symmetric members with no transverse loading between brace points, C_b equaled to 2.27, 1.67, and 1.0 for the case of equal end moments of the same sign (reverse curvature bending), zero moment at one end, and uniform moment, respectively. Essentially, as the moment diagram becomes more uniform, i.e., has a flatter slope, the corresponding LTB capacity decreases. This principle can be applied to the CB specimens that experience LTB. Figure 3.8 shows that fixed-fixed columns bend in reverse curvature with the inflection point at the midspan, while that of the fixed-rotating columns locates closer to the rotating end. As a result, at the same fixed-end moment magnitude, the latter would have a less steep moment diagram than the former and, thus, be assigned with C_b less than 2.27. Essentially, the "more uniform" moment diagram of the fixed-rotating column makes it more prone to LTB and, thus, reduces its peak flexural strength even under cyclic loading. This effect is amplified as the magnitude of the end rotation increases since this results in a more uniform moment diagram. For instant, Specimen 11H-BC was subjected to a larger end rotation (ξ = 1.1) than the other fixed-rotating specimens (ξ = 1.0); consequently, its peak flexural strength was much lower than that of Specimen 1H as shown in Figure 5.2(a).

Based on the inflection point location, C_b could be calculated for each fixed-fixed and fixed-rotating CB column as shown in Table 5.1. For each specimen pair, the ratio between the two quantities, i.e., C_b^{FR}/C_b^{FF}, was determined. Similarly, a ratio between the peak fixed-end moments with respect to the two boundary condition cases, i.e., $M_{max}^{FR}/M_{max}^{FF}$, was also calculated. The former and latter ratios appeared to correlate relatively well. Finite element results also supported this claim as shown in Table 5.2.

Lastly, in the flexural-strength degradation zone, it was observed that the degrading rate, i.e., the slope of the degrading branch of the backbone curve, was similar for the fixed-fixed and fixed-rotating specimens with the ALB failure mode. This was also true for the CB specimen pairs, but in some cases, the fixed-rotating column degraded slower; the flexural demand reduction as the result of the end rotation appeared to moderate the degrading rate in the fixed-rotating CB specimens.

5.3 Conversion between Fixed-fixed and Fixed-rotating Boundary Conditions

5.3.1 Plastic Story Drift Angle

As discussed in Section 5.2, elastic and inelastic flexural stiffnesses decreased as the result of the end rotation at one end of the column. In turn, these stiffnesses affected the lateral drift range of each zone in the backbone curve. In the elastic zone, cyclic behavior of a beam-column could be predicted based on the Timoshenko theory as discussed in Section 3.2.2.2; Eq. (5.2) expresses the elastic stiffness relationship between the fixed-end moment and the moving end's lateral displacement and rotation.

$$M = \left(K_{C,41} - \frac{\xi}{L}K_{C,42}\right)\Delta = K_e\Delta \tag{5.2}$$

where $K_{C,41}$ and $K_{C,42}$ are calculated as follows [refer to Eq. (3.45)]:

$$K_{C,41} = \frac{EI}{L^2\Psi_C}\Phi^2(1+\mu)(1-\cos\Phi)$$
$$K_{C,42} = \frac{EI}{L\Psi_C}\Phi[\Phi-(1+\mu)\sin\Phi] \tag{5.3}$$

To investigate the plastic component of the moment-displacement response, which was more difficult to predict in cyclic tests, the elastic component of the lateral drift was isolated per Eq. (5.4), resulting in the plastic drift response.

$$\Delta_p = \Delta - \frac{M}{K_e} \tag{5.4}$$

As shown in Figure 5.5, the fixed-fixed and fixed-rotating backbone curves were plotted against this plastic component of the lateral drift divided by the undeformed column length, i.e., the plastic story drift angle (*SDA*). The results showed that, for Group 13 and 16 specimen pairs, the two moment versus plastic *SDA* backbone curves resembled similar shapes, indicating that the plastic rotation capacity remained relatively the same for both boundary condition cases, and the effect of the end rotation mostly concentrated in the elastic component of the lateral drift response.

5.3.2 Equivalent Story Drift Angle and Response Conversion

Accordingly, to convert the backbone curves of the fixed-fixed case to the fixed-rotating case, and vice versa, the elastic lateral drift corresponding to the boundary condition of interest could be added to the plastic drift response:

(1) Fixed-fixed (FF) to fixed-rotating (FR)

$$\Delta_{eqv}^{FF\rightarrow FR} = \Delta_p^{FF} + \frac{M^{FF}}{K_e^{FR}} \tag{5.5}$$

(2) Fixed-rotating (FR) to fixed-fixed (FF)

$$\Delta_{eqv}^{FR\rightarrow FF} = \Delta_p^{FR} + \frac{M^{FR}}{K_e^{FF}} \tag{5.6}$$

With respect to the test results, Figure 5.6 and Figure 5.7 show the backbone curve conversion based on Eqs. (5.5) and (5.6), respectively; the converted backbone curves agree reasonably well with the intended ones.

5.3.3 Validation of Response Conversion Method with Finite Element Models

To further assess the proposed conversion procedure, it was applied to finite element simulation results, which provided clean data that covered wider drift ranges than what could be accomplished in testing. Software ABAQUS-CAE was utilized in this study. Three models with the W18, W24, and W30 sections, respectively, were considered for each failure mode, i.e., the ALB and CB modes. Geometry of the wide-flange cross sections was simplified in the models, ignoring the fillet portions; a shell extrusion technique was used in constructing the models. The models employed 4-node doubly curved "S4R" shell elements suitable in analyses that involved severe local buckling; such was expected to occur at the member ends in this study.

Figure 5.8 shows an example model with boundary condition details. To simulate a fixed column base, all six degrees of freedom of the nodes at the bottom end were fixed. At the top end, all edge nodes were coupled, and movements were prescribed at the edge node at the centroid of the cross section. Lateral displacement was prescribed to U2 degree of freedom. For fixed-rotating column simulation, rotation sequence was also prescribed to UR1 degree of freedom. U3 was a free degree of freedom allowing the column to shorten under the applied loads. The remaining degrees of freedom at the top column end were fixed.

Obtained from elastic buckling analysis (i.e., eigen analysis), the right figure in Figure 5.8 shows the first buckling mode of the column subjected to a unit axial and lateral force. This deformed configuration scaled to a hundredth in magnitude was applied to the model as its initial geometric imperfection.

The elastic material properties of steel were defined by a Young's Modulus of 29000 ksi and a Poisson's ratio of 0.3. Regarding inelastic material behavior, yield stresses were specified for the flange and web components of the model, respectively, according to stress-strain relationships obtained from tensile coupon tests. To capture cyclic material behavior of steel, both nonlinear isotropic and nonlinear kinematic hardening rules were included in the material model. Their related parameters were calibrated using the available cyclic and tensile coupon test results based on procedures provided in the ABAQUS manual (HKS, 2007).

Some simulation results of these models were first correlated with the test data (Specimens 13M, 13M-BC, 16M, and 16M-BC) as shown in Figure 5.9 to Figure 5.12 to ensure that the finite element models were reliable. The same comparison approach implemented on the test data was utilized: Figure 5.13 to Figure 5.16 compare the fixed-fixed and fixed-rotating backbone curves of each model pairs with respect to the *SDA*, plastic *SDA*, and equivalent *SDA*, respectively. In conclusion, finite element results support the previous observations regarding the backbone-curve characteristics and the effect of the end rotation; they also validate the proposed procedure in calculating the equivalent lateral drifts.

While ξ, the rotation-to-drift ratio, of Specimens 13M-BC and 16M-BC was equal to 1, Specimen 11H-BC sustained a slightly greater end-rotation magnitude, i.e., ξ = 1.1.

Since the latter failed in the CB mode, the greater end-rotation magnitude considerably affected its peak flexural strength (discussed in Section 5.2). Consequently, its plastic backbone curve did not resemble that of its fixed-fixed counterpart as well as the others. Further research is needed to investigate the effects of large end-rotation magnitudes on the responses of columns with CB failure mode.

Chapter 2, 3, 4, and 5 in part are currently being prepared for submission for publication of the material. Chansuk, P., Ozkula, G., and Uang, C.-M. (2018). “ATC-106 Phase 2: Seismic behavior and design of deep, slender wide-flange structural steel beam-columns.” *Report No. SSRP-18/02*, University of California, San Diego, La Jolla, CA. The thesis author was the primary investigator and author of this material.

Table 5.1 Test Results: LTB Modification Factors of CB Specimens

Specimen	Shape	Boundary Condition	C_b	$\frac{C_b^{FR}}{C_b^{FF}}$	Moment Range (×1000 kip-ft)	$\frac{M_{max}^{FR}}{M_{max}^{FF}}$
1H	W24×176	Fixed-fixed	2.27	0.89	(-1.96, 2.01)	(0.86, 0.87)
11H-BC	W24×176	Fixed-rotating	2.02		(-1.69, 1.75)	
16M	W18×130	Fixed-fixed	2.27	0.95	(-1.30,1.35)	(0.99,0.93)
16M-BC	W18×130	Fixed-rotating	2.16		(-1.28,1.26)	

Table 5.2 ABAQUS Results: LTB Modification Factors of CB Specimens

Model	Shape	Boundary Condition	C_b	$\frac{C_b^{FR}}{C_b^{FF}}$	Moment Range (×1000 kip-ft)	$\frac{M_{max}^{FR}}{M_{max}^{FF}}$
11M	W24×176	Fixed-fixed	2.27	0.95	(-2.51, 2.53)	(0.97, 0.96)
11M-BC	W24×176	Fixed-rotating	2.16		(-2.43, 2.43)	
16M	W18×130	Fixed-fixed	2.27	0.95	(-1.42, 1.42)	(0.95, 0.95)
16M-BC	W18×130	Fixed-rotating	2.16		(-1.35, 1.35)	
22L	W30×148	Fixed-fixed	2.27	0.95	(-3.04, 3.04)	(0.97, 0.97)
22L-BC	W30×148	Fixed-rotating	2.15		(-2.96, 2.97)	

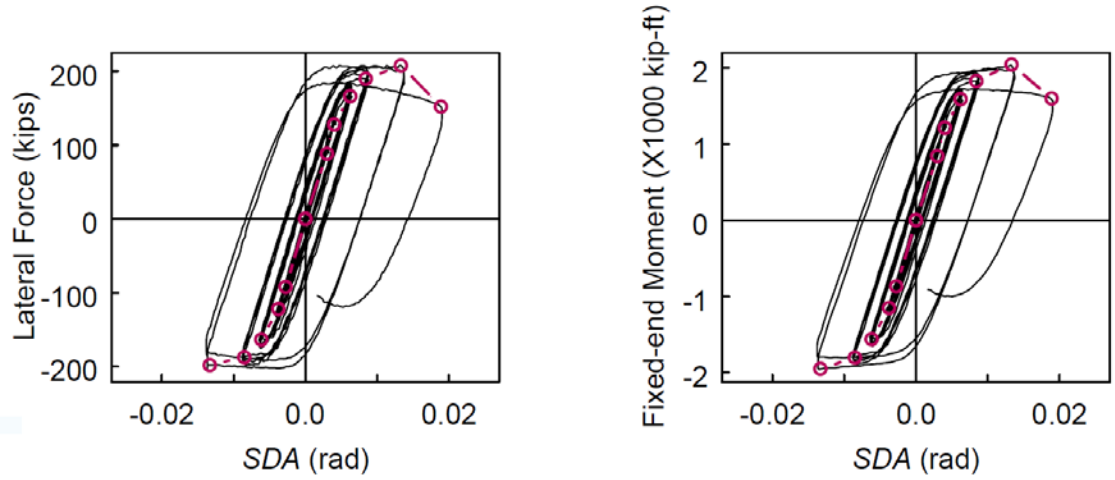

(a) Specimen 1H

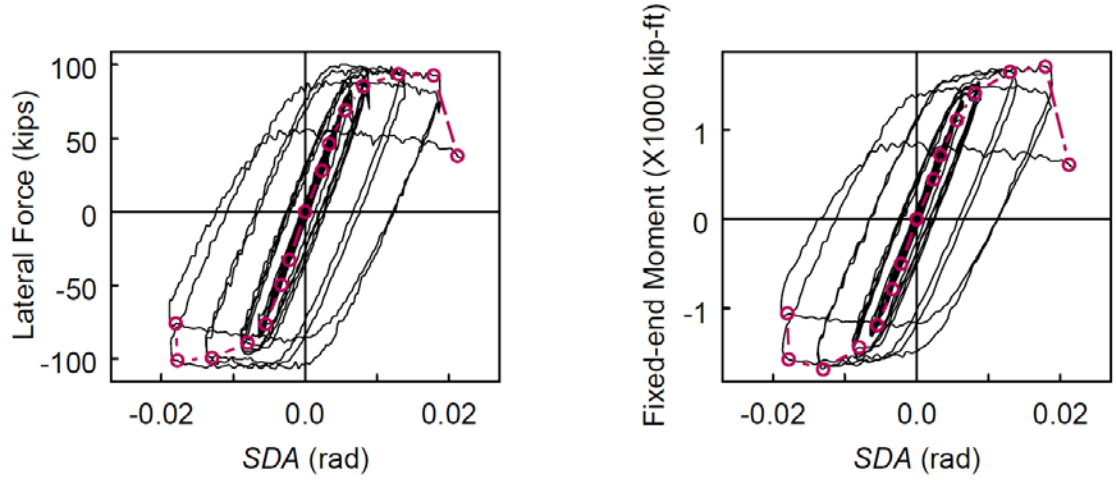

(b) Specimen 11H-BC

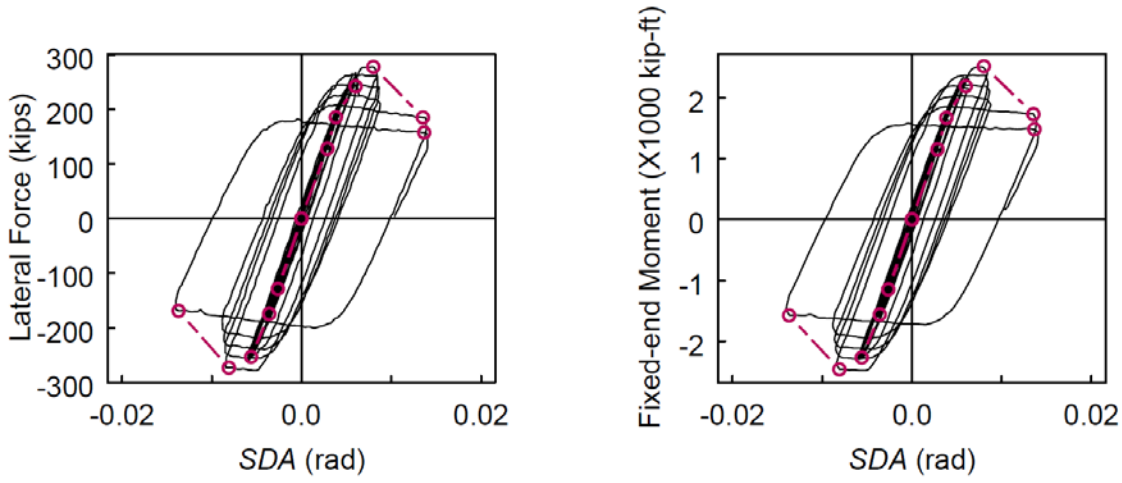

(c) Specimen 13M

Figure 5.1 Test Results: Construction of Backbone Curves

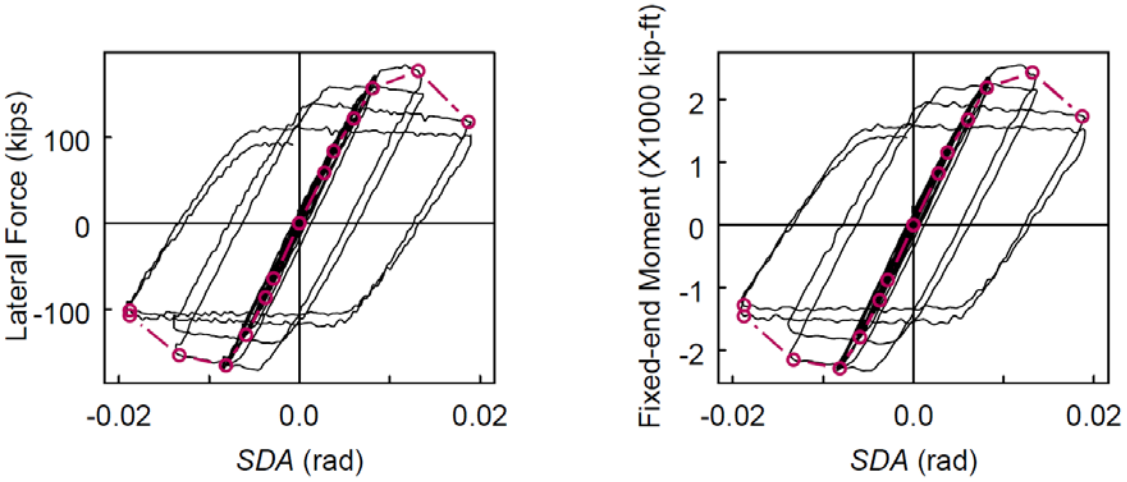

(d) Specimen 13M-BC

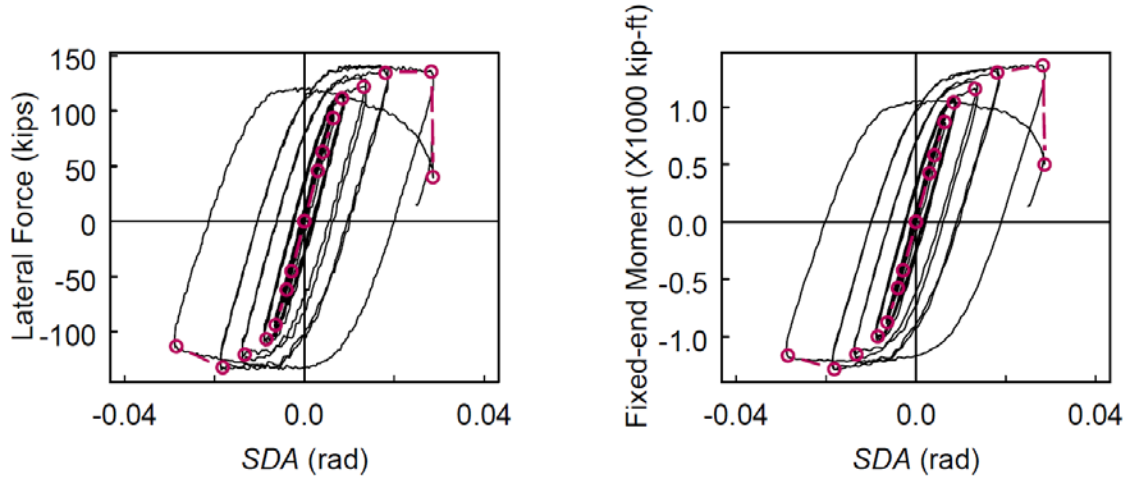

(e) Specimen 16M

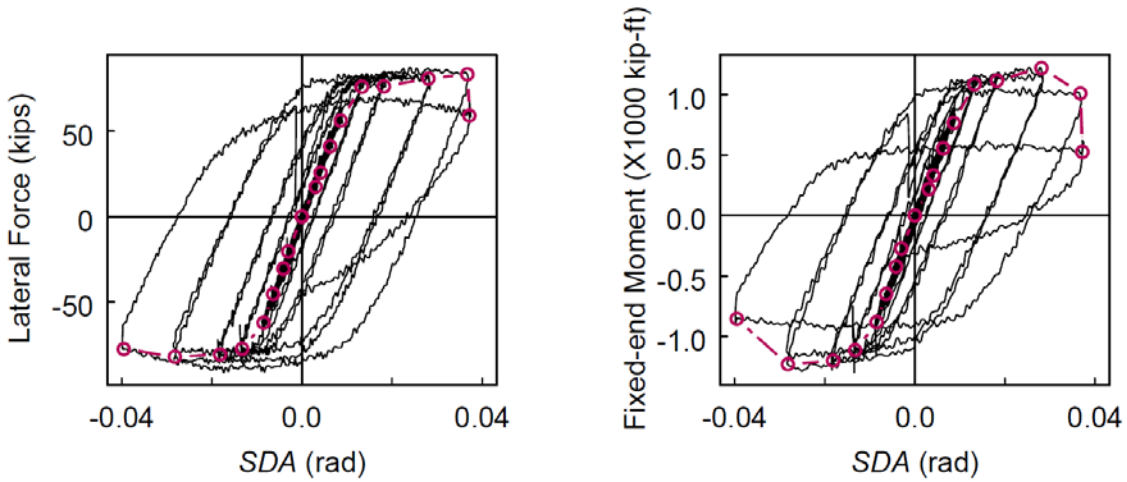

(f) Specimen 16M-BC

Figure 5.1 Test Results: Construction of Backbone Curves (continued)

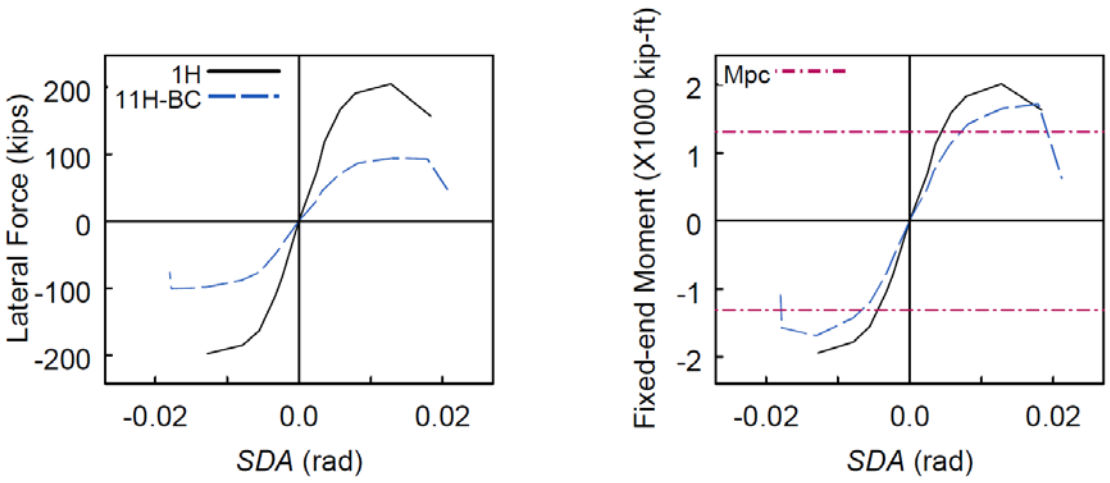

(a) Specimens 1H vs. 11H-BC (CB Mode)

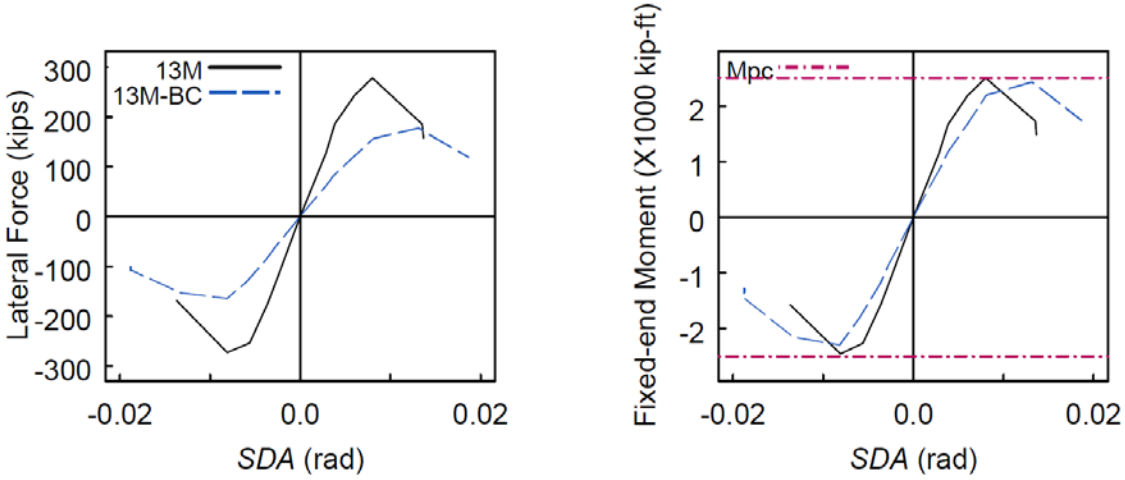

(b) Specimens 13M vs. 13M-BC (ALB Mode)

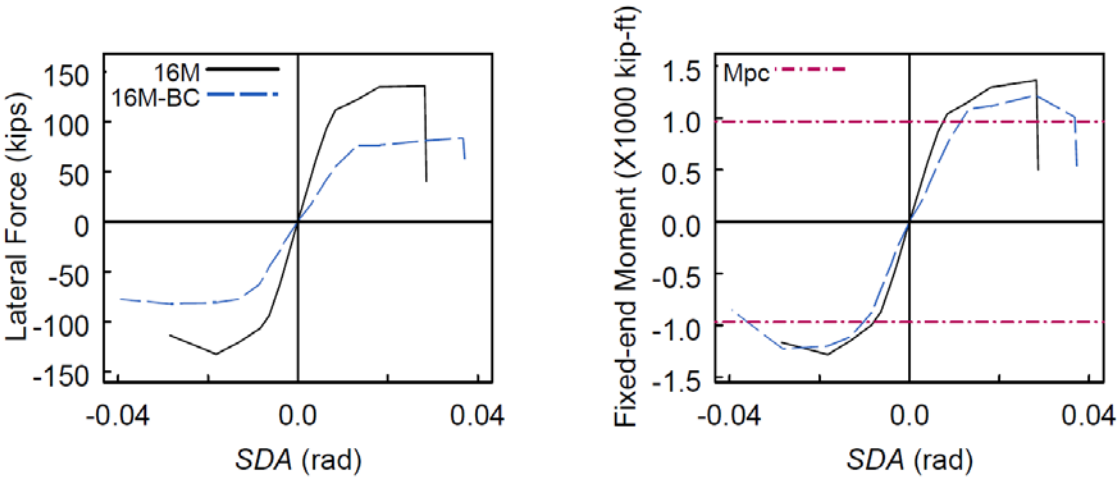

(c) Specimens 16M vs. 16M-BC (CB Mode)

Figure 5.2 Test Results: Comparison of Backbone Curves

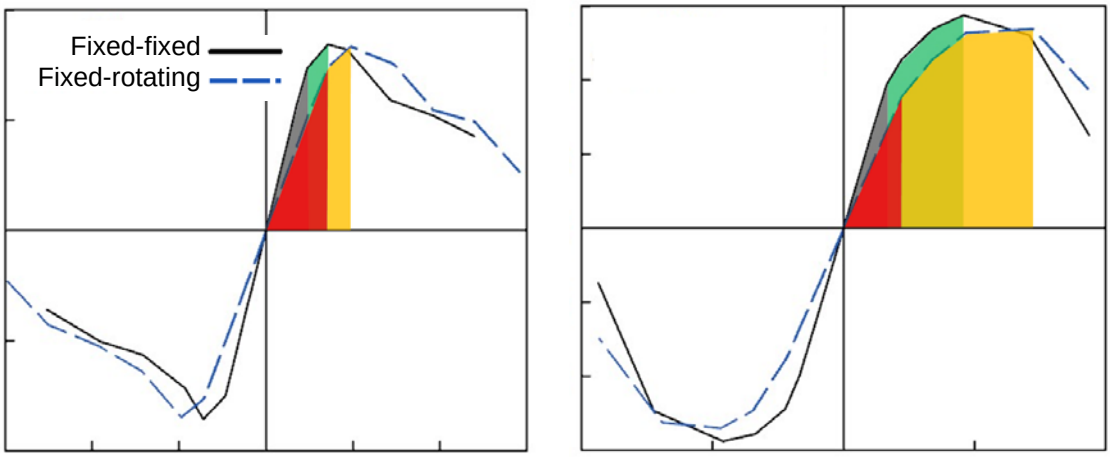

(a) ALB Specimens (b) CB Specimens

Figure 5.3 Elastic, Inelastic, Degradation Cyclic Zones

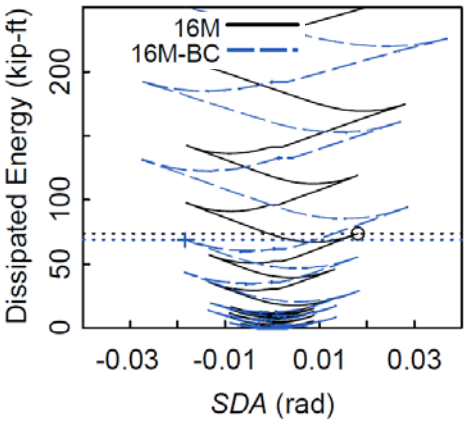

Figure 5.4 Plastic-straining Energy Dissipation

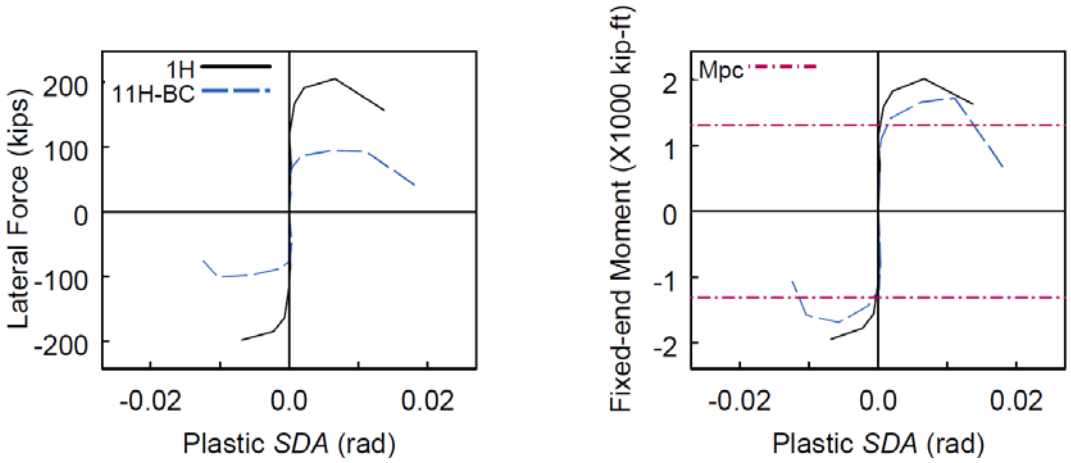

(a) Specimens 1H vs. 11H-BC

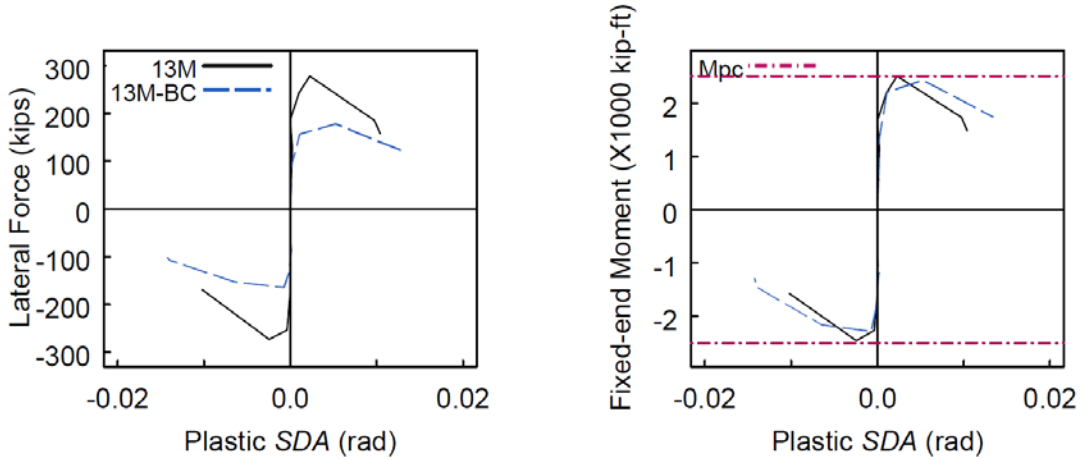

(b) Specimens 13M vs. 13M-BC

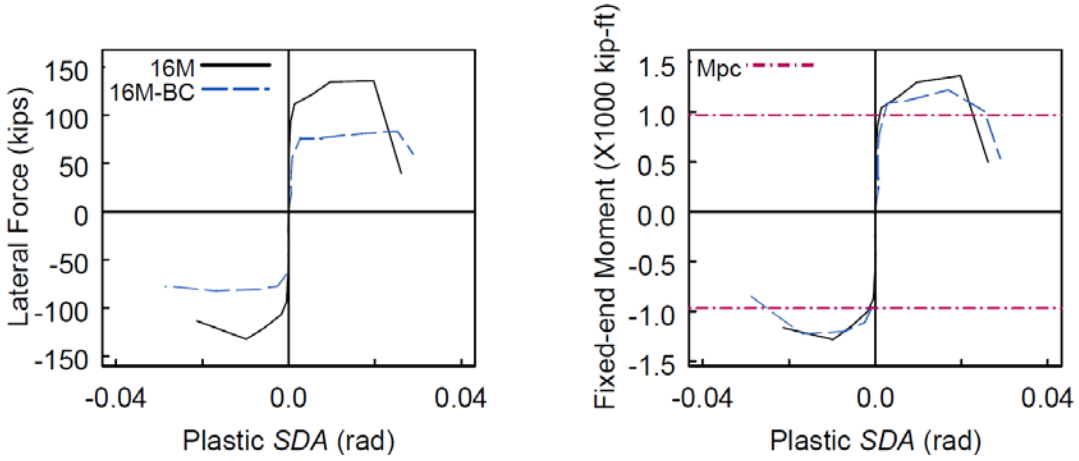

(c) Specimens 16M vs. 16M-BC

Figure 5.5 Test Results: Comparison of Plastic Component of Backbone Curves

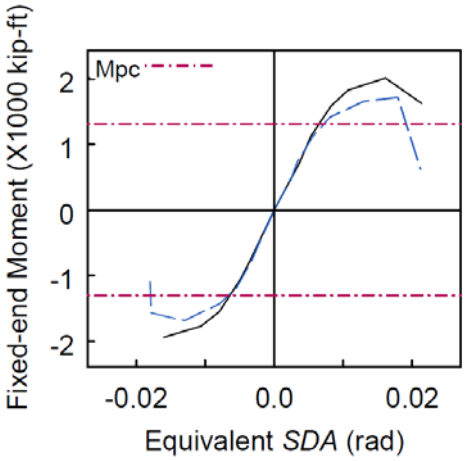

(a) Specimens 1H vs. 11H-BC

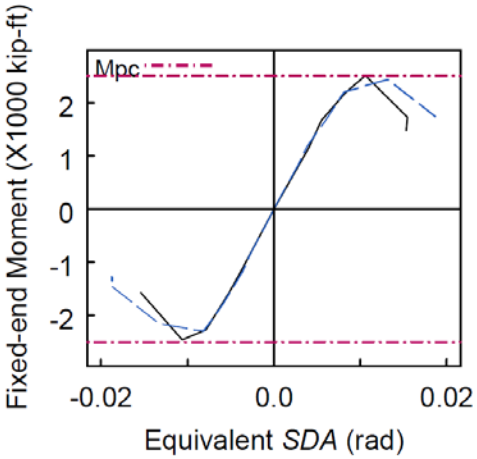

(b) Specimens 13M vs. 13M-BC

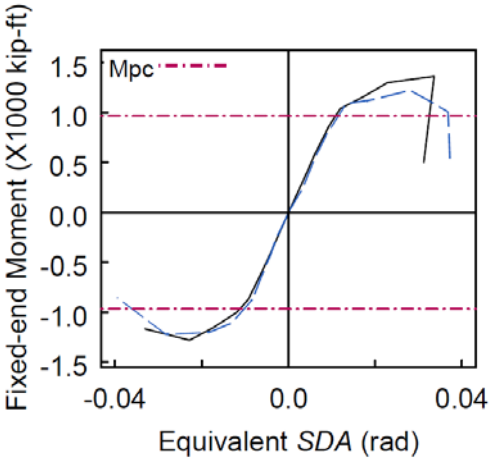

(c) Specimens 16M vs. 16M-BC

Figure 5.6 Response Conversion from Fixed-fixed to Fixed-rotating Boundary Conditions (Based on Test Results)

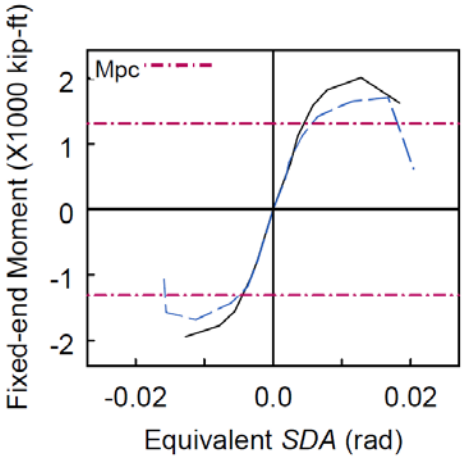

(a) Specimens 1H vs. 11H-BC

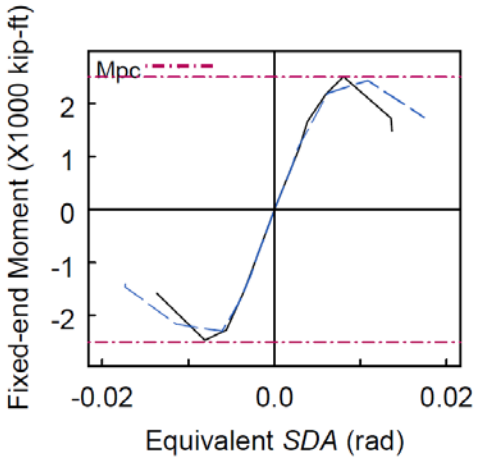

(b) Specimens 13M vs. 13M-BC

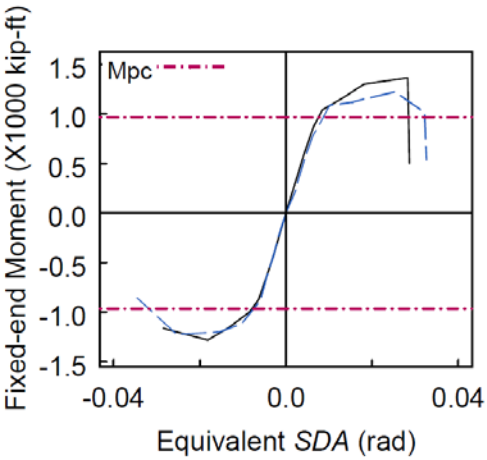

(c) Specimens 16M vs. 16M-BC

Figure 5.7 Response Conversion from Fixed-rotating to Fixed-fixed Boundary Conditions (Based on Test Results)

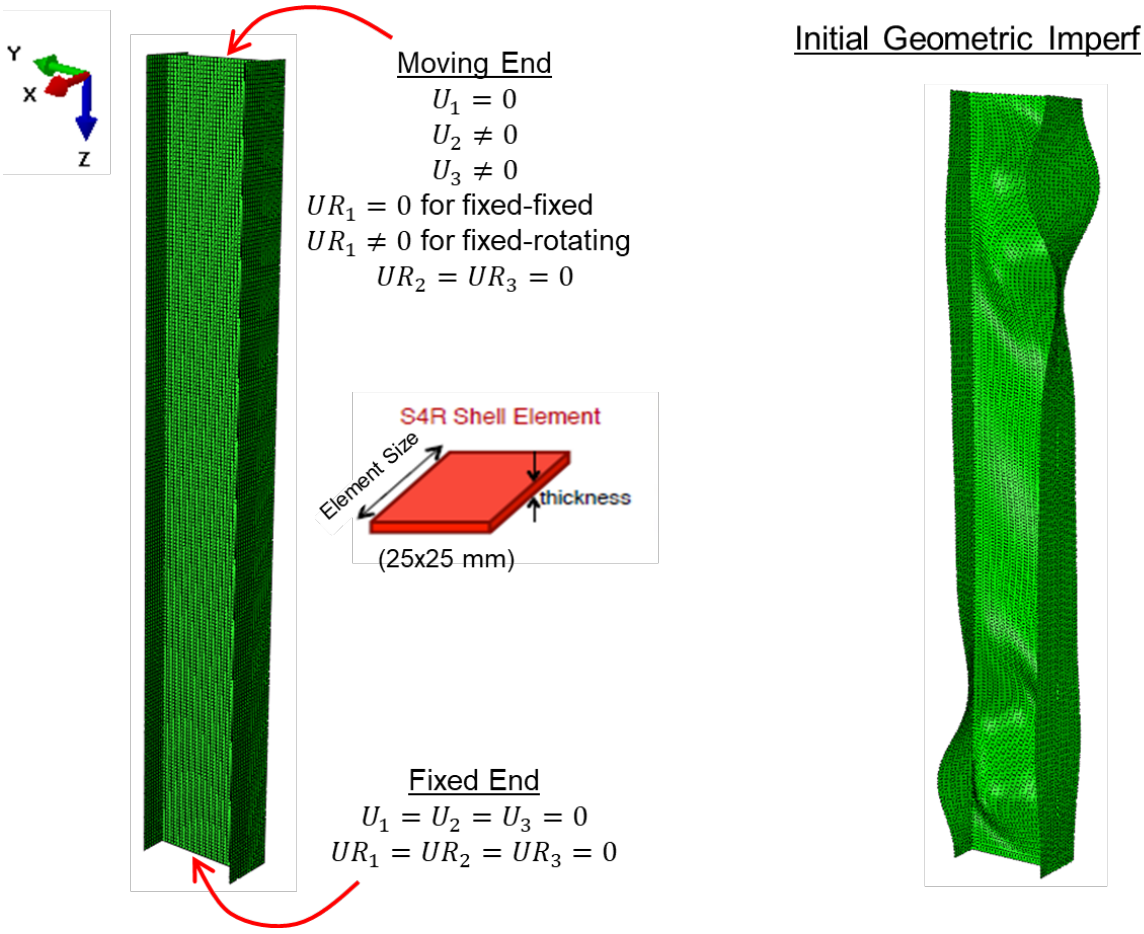

Figure 5.8 ABAQUS Modeling Details

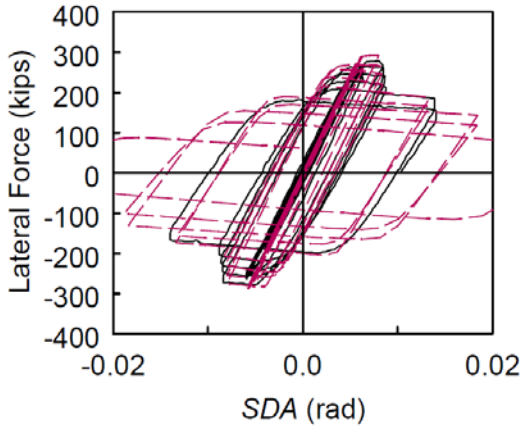

(a) Lateral Force vs. *SDA*

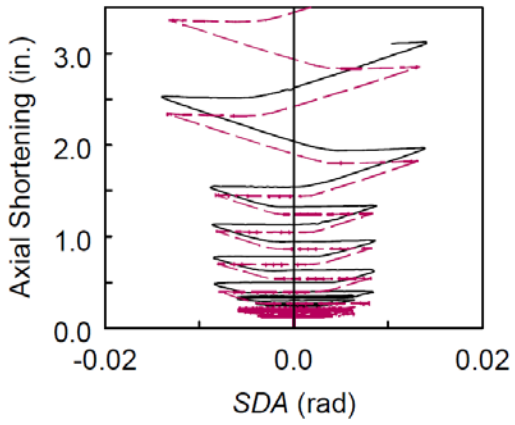

(b) Axial Shortening vs. *SDA*

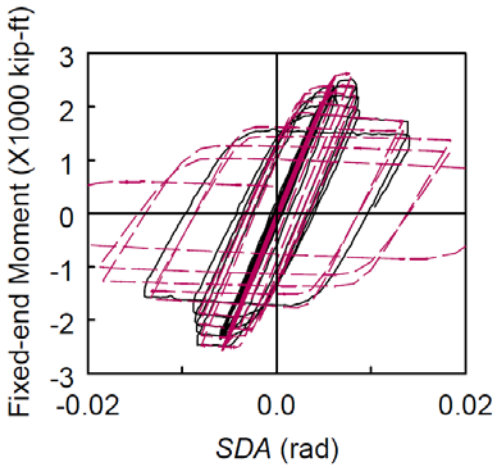

(c) Fixed-end Moment vs. *SDA*

Figure 5.9 Specimen 13M: Test (solid black) and ABAQUS (dashed red) Result Correlation

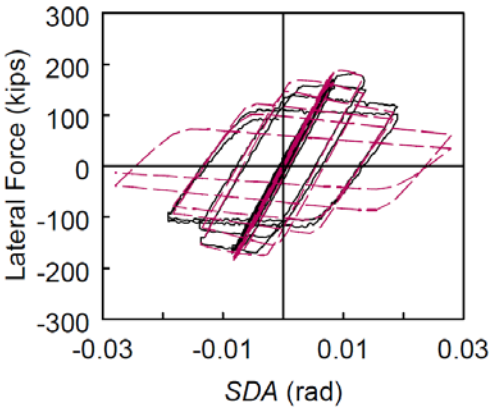

(a) Lateral Force vs. *SDA*

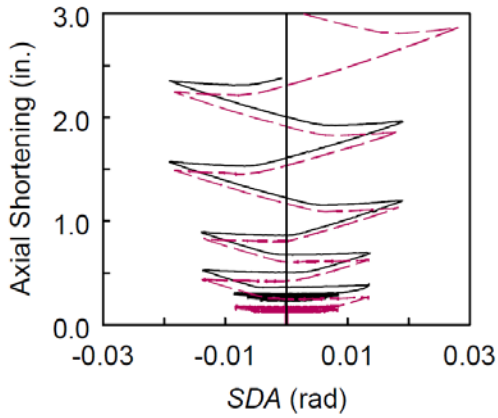

(b) Axial Shortening vs. *SDA*

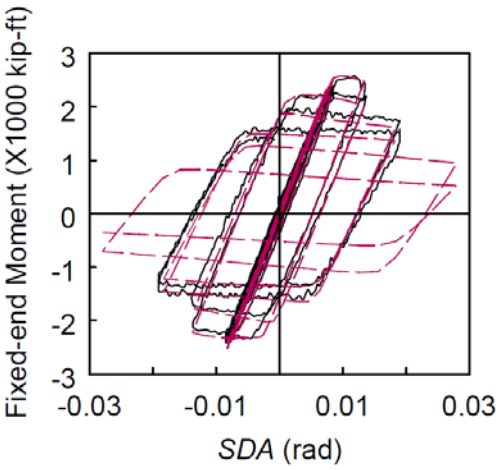

(c) Fixed-end Moment vs. *SDA*

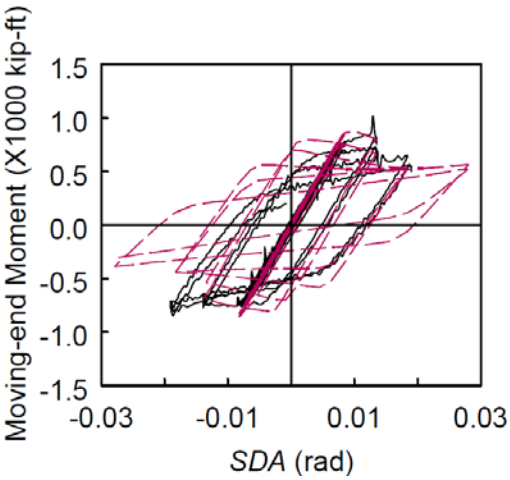

(d) Moving-end Moment vs. *SDA*

Figure 5.10 Specimen 13M-BC: Test (solid black) and ABAQUS (dashed red) Result Correlation

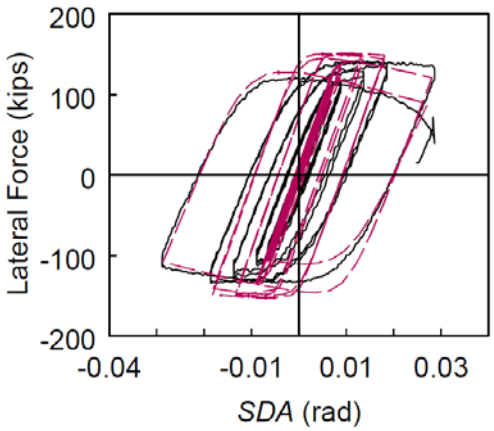

(a) Lateral Force vs. *SDA*

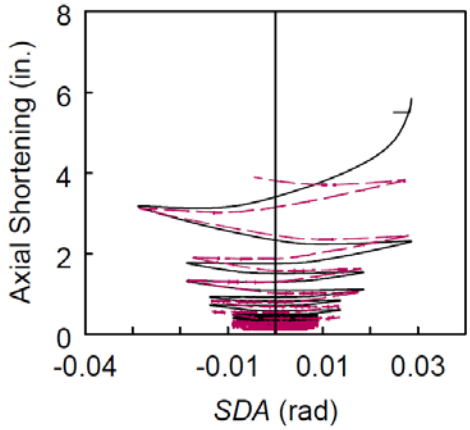

(b) Axial Shortening vs. *SDA*

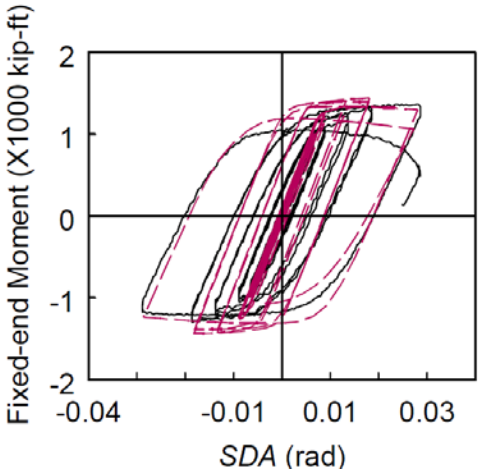

(c) Fixed-end Moment vs. *SDA*

Figure 5.11 Specimen 16M: Test (solid black) and ABAQUS (dashed red) Result Correlation

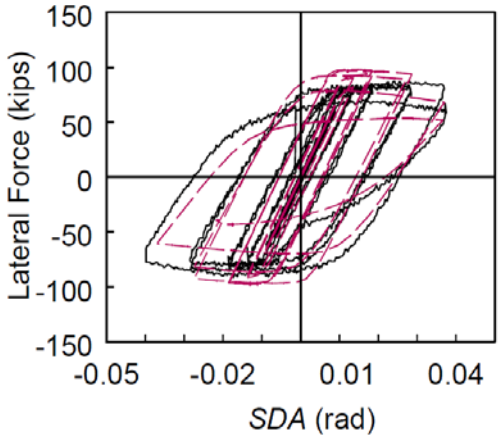

(a) Lateral Force vs. *SDA*

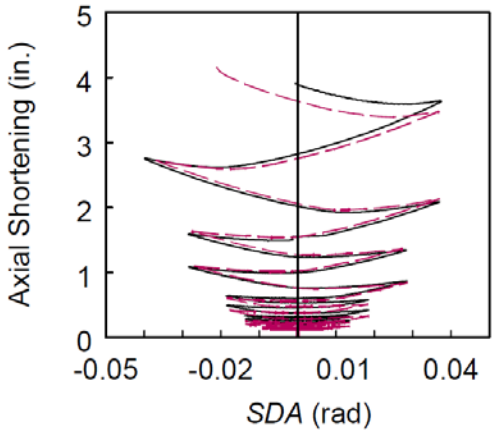

(b) Axial Shortening vs. *SDA*

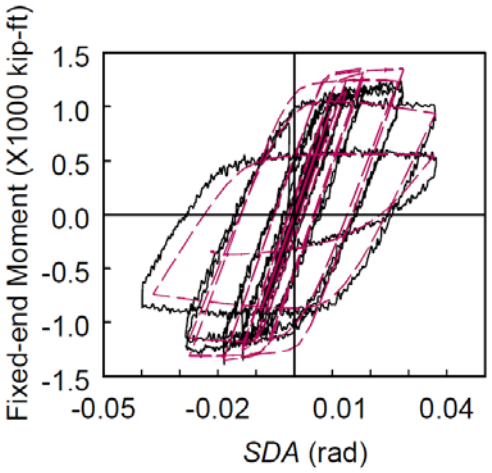

(c) Fixed-end Moment vs. *SDA*

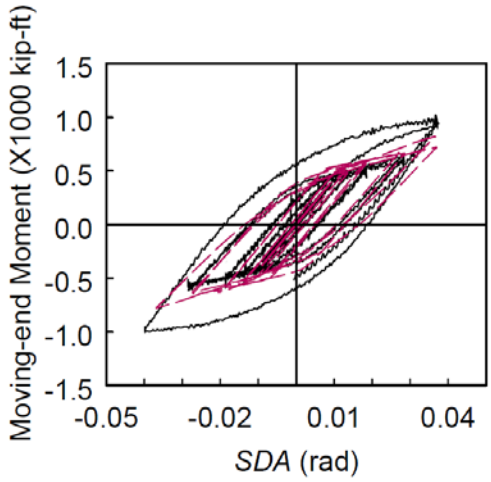

(d) Moving-end Moment vs. *SDA*

Figure 5.12 Specimen 16M-BC: Test (solid black) and ABAQUS (dashed red) Result Correlation

ALB Failure Mode

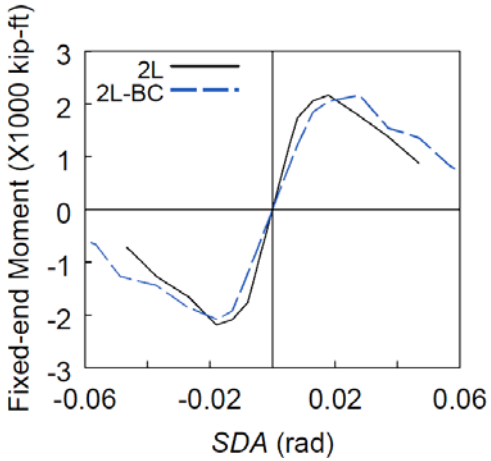

(a) Models 2L vs. 2L-BC (W24×131)

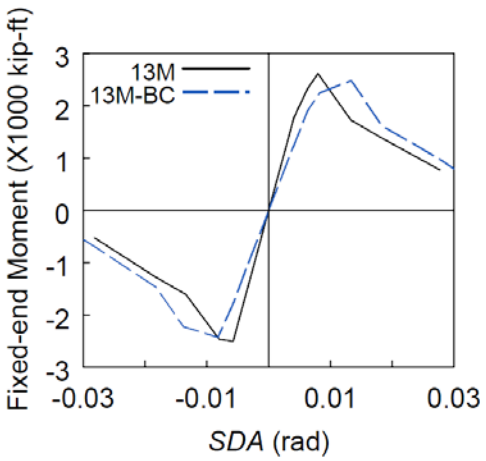

(b) Models 13M vs. 13M-BC (W30×173)

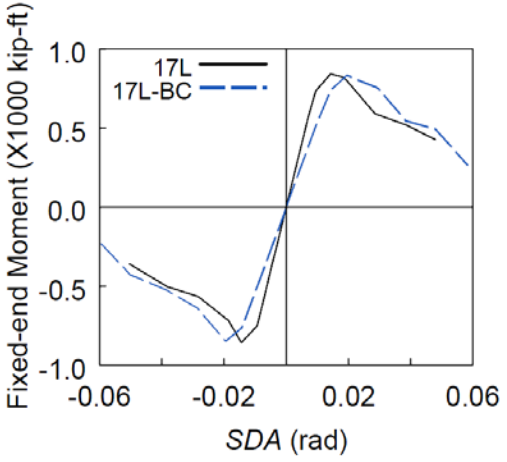

(c) Models 17L vs. 17L-BC (W18×76)

CB Failure Mode

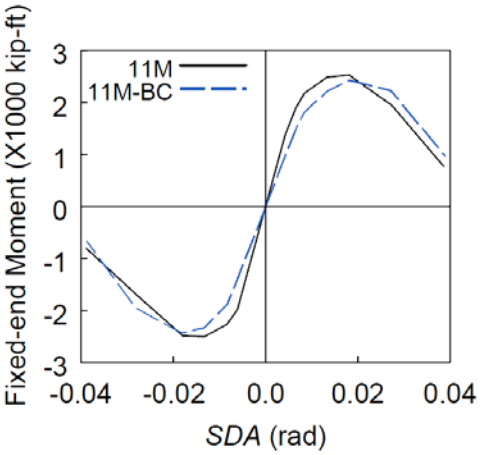

(d) Models 11M vs. 11M-BC (W24×176)

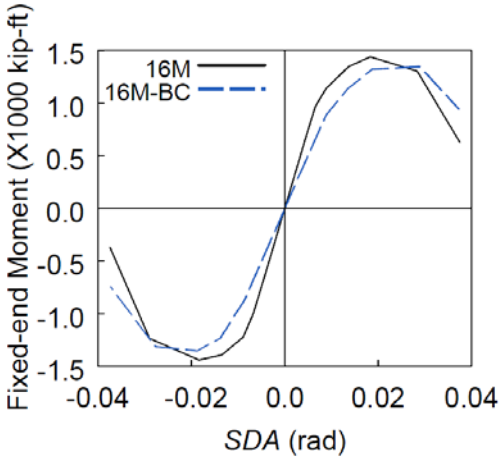

(e) Models 16M vs. 16M-BC (W18×130)

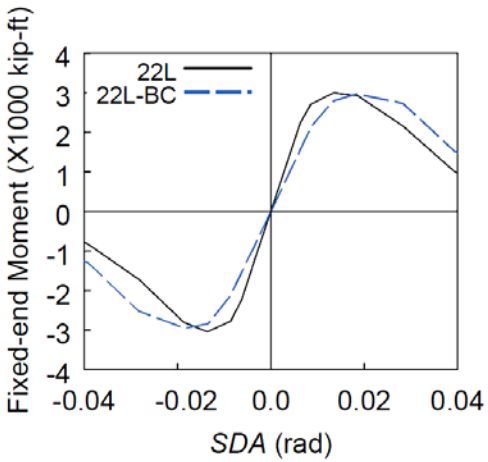

(f) Models 22L vs. 22L-BC (W30×148)

Figure 5.13 ABAQUS Results: Comparison of Backbone Curves

ALB Failure Mode

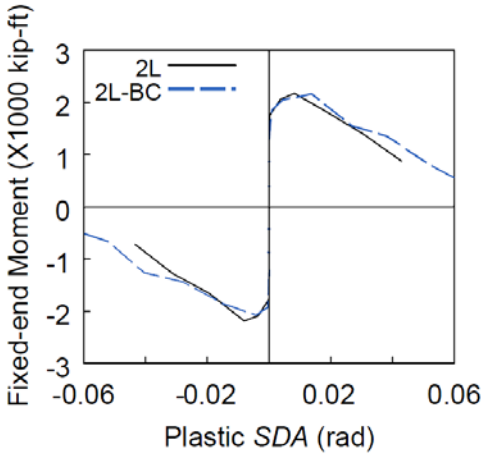

(a) Models 2L vs. 2L-BC (W24×131)

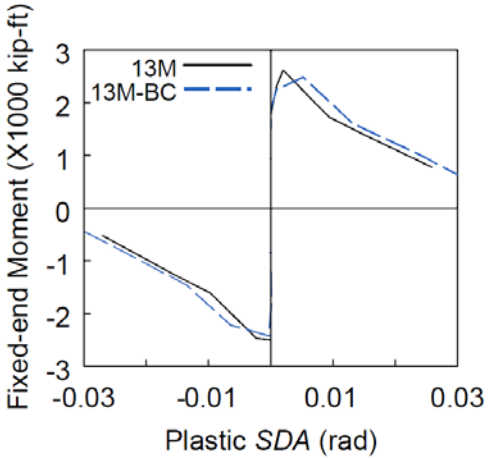

(b) Models 13M vs. 13M-BC (W30×173)

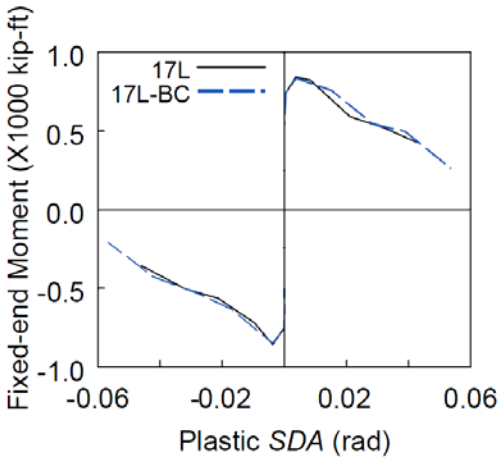

(c) Models 17L vs. 17L-BC (W18×76)

CB Failure Mode

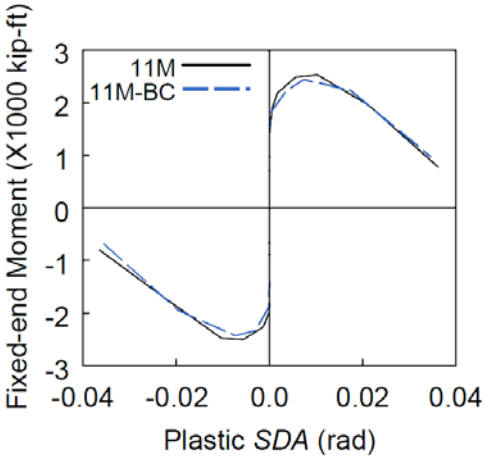

(d) Models 11M vs. 11M-BC (W24×176)

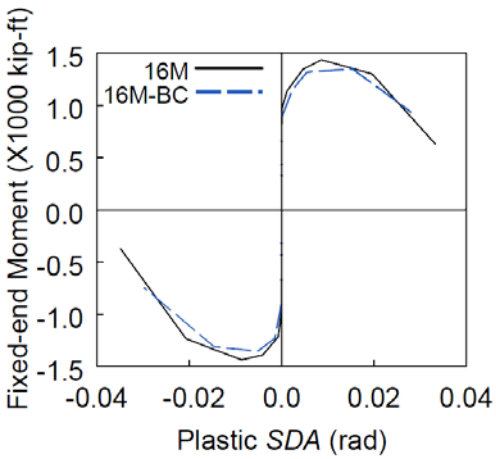

(e) Models 16M vs. 16M-BC (W18×130)

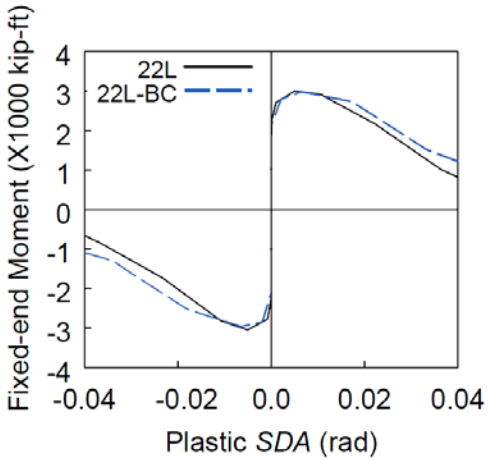

(f) Models 22L vs. 22L-BC (W30×148)

Figure 5.14 ABAQUS Results: Comparisons of Plastic Component of Backbone Curves

ALB Failure Mode

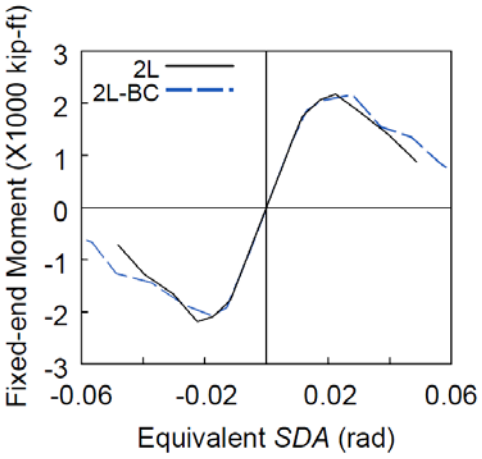

(a) Models 2L vs. 2L-BC (W24×131)

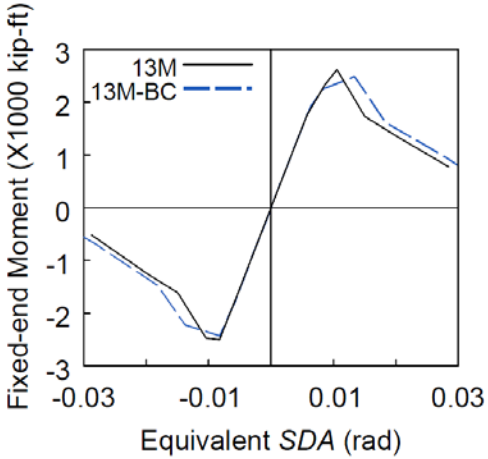

(b) Models 13M vs. 13M-BC (W30×173)

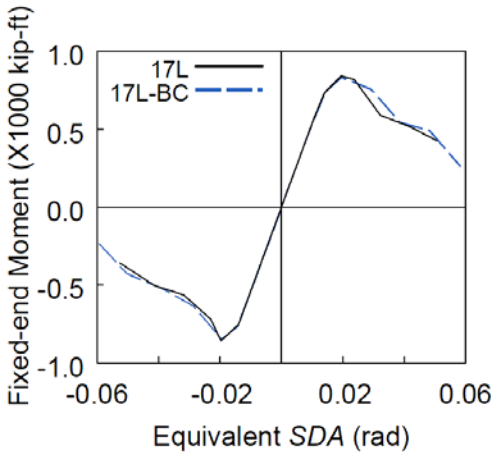

(c) Models 17L vs. 17L-BC (W18×76)

CB Failure Mode

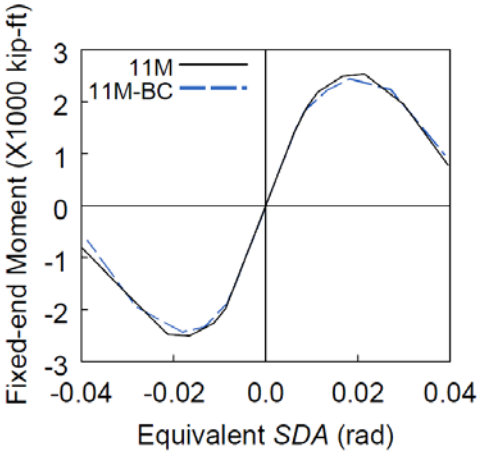

(d) Models 11M vs. 11M-BC (W24×176)

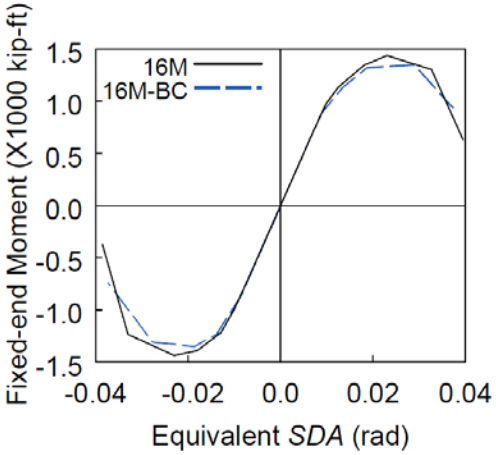

(e) Models 16M vs. 16M-BC (W18×130)

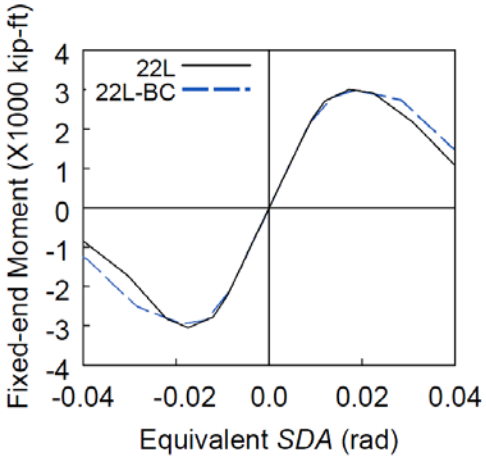

(f) Models 22L vs. 22L-BC (W30×148)

Figure 5.15 Response Conversion from Fixed-fixed to Fixed-rotating Boundary Conditions (Based on ABAQUS Results)

ALB Failure Mode

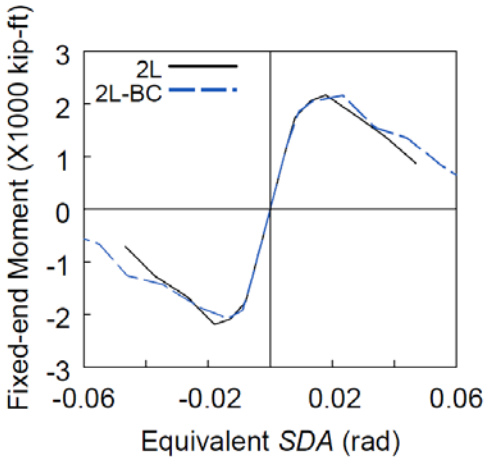

(a) Models 2L vs. 2L-BC (W24×131)

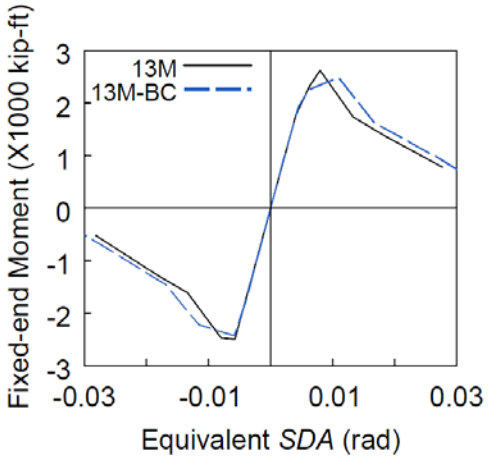

(b) Models 13M vs. 13M-BC (W30×173)

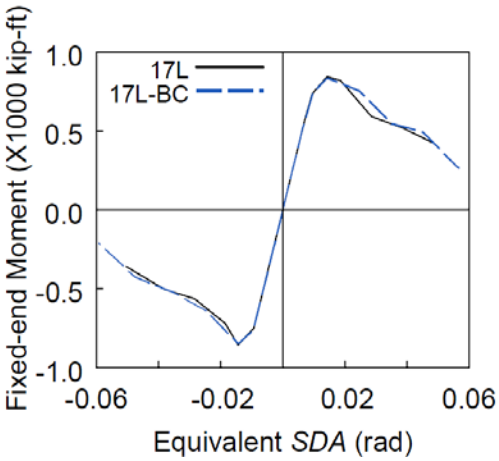

(c) Models 17L vs. 17L-BC (W18×76)

CB Failure Mode

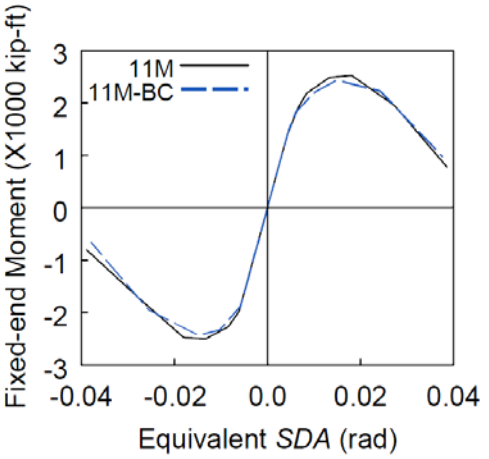

(d) Models 11M vs. 11M-BC (W24×176)

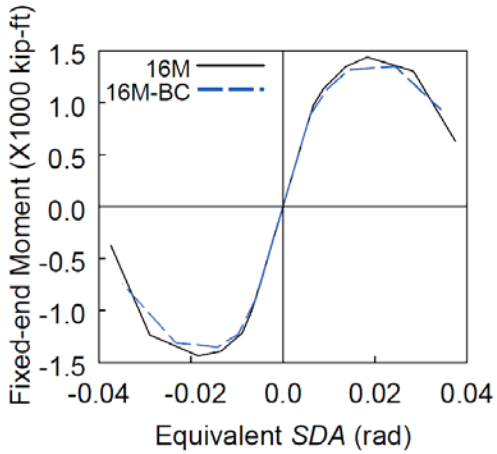

(e) Models 16M vs. 16M-BC (W18×130)

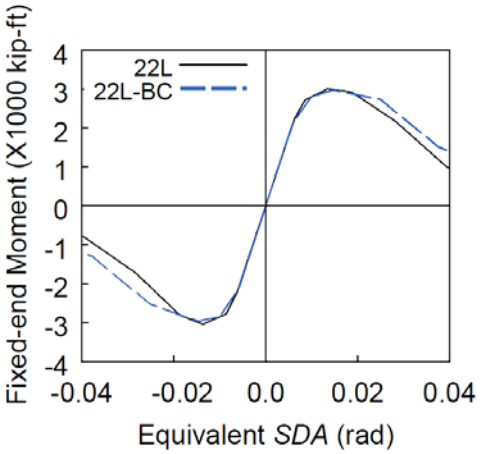

(f) Models 22L vs. 22L-BC (W30×148)

Figure 5.16 Response Conversion from Fixed-rotating to Fixed-fixed Boundary Conditions (Based on ABAQUS Results)

6. SUMMARY AND CONCLUSIONS

6.1 Summary

Twenty-five W24 columns were tested in Phase 1 program (Ozkula and Uang 2015) to evaluate the behavior and response of deep columns for seismic application in SMF design. Phase 1 testing intended to investigate the effects of slenderness parameters, constant axial load levels, lateral drift loading protocols, and biaxial loading on the column responses. In Phase 2 program, twenty-three additional "shallow" (W14) and "deep" (W18, W24, and W30) columns were tested to further investigate Phase 1 objectives and examine the effects of section depths, fixed-rotating boundary conditions, and varying axial loads. Phase 2 test data and numerical simulation results are presented in this thesis to investigate seismic behavior of deep, slender wide-flange structural steel beam-columns. Theoretical study was also conducted to predict the beam-column elastic responses. The following conclusions can be made from this study.

6.2 Conclusions

(1) Timoshenko compatibility and constitutive laws were used to derive elastic flexural stiffness relationships of a two-node member with and without nodal end rotational springs; the derived stiffness relationships account for both shear deformation and the second-order effect.

(2) A data reduction procedure utilizing Timoshenko beam-column theoretical expressions derived in this study was proposed to eliminate the effect of connection flexibility from the column global responses.

(3) Test results showed that boundary conditions, varying axial loads, and lateral-drift sequences had significant effects on the column response but did not influence the governing buckling mode of the specimens.

(4) Cyclic responses of interior columns and exterior columns are very different in terms of maximum flexural strength, post-buckling stiffness degradation, and axial shortening. The backbone curves associated with the interior and exterior columns need to be distinguished from one another for seismic design applications.

(5) Elastic flexural stiffness of specimens subjected to fixed-rotating boundary conditions is lower than that of their nominally identical specimens with fixed-fixed ends. A procedure to convert flexural-strength backbone curves of fixed-fixed columns to account for rotation at the top end was proposed.

REFERENCES

(1) AISC. (2016a). "Seismic provisions for structural steel buildings." *ANSI/AISC 341-16*, Chicago.

(2) AISC. (2016b). "Prequalified connections for special and intermediate steel moment frames for seismic applications." *AISC 358*, Chicago.

(3) AISC. (2016c). "Specification for structural steel buildings." *AISC 360*, Chicago.

(4) ASCE. (2013). "Seismic evaluation and retrofit of existing buildings." *ASCE/SEI 41-13*, Reston, VA.

(5) ASCE. (2016). "Minimum design loads and associated criteria for buildings and other Structures." *ASCE/SEI 7*, Reston, VA.

(6) ASCE-WRC (Welding Research Council). (1971). "Plastic design in steel: A guide and commentary." *Manual of Practice No. 41*, New York.

(7) Chen, W. F., and Lui, E. M. (1987). *Structural stability: Theory and implementation*, Elsevier Science, New York.

(8) Cowper, G. R. (1966). "The shear coefficient in Timoshenko's beam theory." *J. of Applied Mechanics*, 33(2), ASME, 335-340.

(9) Elkady, A., and Lignos, D. G. (2016). "Dynamic stability of deep and slender wide-flange steel columns: Full scale experiments." *Proc., Annual Stability Conf.*, Structural Stability Research Council, Orlando, FL.

(10) FEMA. (2000). "Recommended seismic design criteria for new steel moment-frame buildings." *FEMA-350*, Washington, DC.

(11) Graff, K. F. (1975). *Wave motion in elastic solids*, Dover, Oxford.

(12) HKS (Hibbit, Karlsson, and Sorenson, Inc.). (2007). *ABAQUS/Standard 6.7 User's Manual*, Pawtucket, RI.

(13) Harris, J. L., and Speicher, M. S. (2015). "Assessment of first generation performance-based seismic design nethods for new steel buildings volume 1: Special moment frames." *NIST TN 1863-1*, Gaithersburg, MD.

(14) Krawinkler, H., Gupta, A., Medina, R., and Luco, N. (2000). "Loading histories for seismic performance testing of SMRF components and assemblies." *Rep. No. SAC/BD-00/10*, SAC Joint Venture, Sacramento, CA.

(15) MacRae, G. A., Carr, A. J., and Walpole, W. R. (1990). "The seismic response of steel frames." *Research Rep. 90-6*, Univ. of Canterbury, Christchurch, New Zealand.

(16) McGuire, W., Gallagher, R. H., and Ziemian, R. D. (2014). *Matrix structural analysis*, 2nd Ed.

(17) Newell, J. D., and Uang, C.-M. (2008). "Cyclic behavior of steel wide-flange columns subjected to large drift." *J. Struct. Eng.*, 134(8), 1334-1342.

(18) NIST. (2011). "Research plan for the study of seismic behavior and design of deep, slender, wide-flange structural steel-beam-column members." *NIST-GCR-11-917-13*, Gaithersburg, MD.

(19) Ozkula, G., and Uang, C.-M. (2015). "Seismic behavior and design of deep, slender wide-flange structural steel beam-column members." *Rep. No. SSRP-15/06*, Department of Structural Engineering, University of California, San Diego, La Jolla, CA.

(20) Ozkula, G., Harris, J., and Uang, C.-M. (2017). "Classifying cyclic buckling modes of steel wide-flange columns under cyclic loading." *Proc., Structures Congress*, ASCE, Reston, VA.

(21) Przemieniecki, J. S. (1968). *Theory of matrix structural analysis*, Dover, Mineola, NY.

(22) Seaburg, P. A., and Carter, C. J. (1997). "Torsional analysis of structural steel members." *Steel Design Guide Series 9*, AISC.